IONOSPHERIC CORRECTION OF INTERFEROMETRIC SAR DATA WITH APPLICATION TO THE CRYOSPHERIC SCIENCES

By

Heming Liao

A Dissertation Submitted in Partial Fulfillment of the Requirements

for the Degree of

Doctor of Philosophy

in

Geophysics

University of Alaska Fairbanks

August 2018

APPROVED:

Dr. Franz J. Meyer, Committee Chair

Dr. Jeffrey T. Freymueller, Committee Member

Dr. Carl Tape, Committee Member

Dr. Brenton Watkins, Committee Member

Dr. Paul McCarthy, Chair

Department of Geosciences

Dr. Anupma Prakash, Interim Dean

College of Natural Science and Mathematics

Dr. Michael Castellini, Dean

Graduate School

Abstract

The ionosphere has been identified as an important error source for spaceborne Synthetic Aperture Radar (SAR) data and SAR Interferometry (InSAR), especially for low frequency SAR missions, operating, e.g., at L-band or P-band. Developing effective algorithms for the correction of ionospheric effects is still a developing and active topic of remote sensing research. The focus of this thesis is to develop robust and accurate techniques for ionospheric correction of SAR and InSAR data and evaluate the benefit of these techniques for cryospheric research fields such as glacier ice velocity tracking and permafrost deformation monitoring. As both topics are mostly concerned with high latitude areas where the ionosphere is often active and characterized by turbulence, ionospheric correction is particularly relevant for these applications.

After an introduction to the research topic in Chapter 1, Chapter 2 will discuss open issues in ionospheric correction including processing issues related to baseline-induced spectrum shifts. The effect of large baseline on split spectrum InSAR technique has been thoroughly evaluated and effective solutions for compensating this effect are proposed. In addition, a multiple sub-band approach is proposed for increasing the algorithm robustness and accuracy. Selected case studies are shown with the purpose of demonstrating the performance of the developed algorithm.

In Chapter 3, the developed ionospheric correction technology is applied to optimize InSAR-based ice velocity measurements over the big ice sheets in Greenland and the Antarctic. Selected case studies are presented to demonstrate and validate the effectiveness of the proposed correction algorithms for ice velocity applications. It is shown that the ionosphere signal can be larger than the actual glacier motion signal in the interior of Greenland and Antarctic, emphasizing the necessity for operational ionospheric correction. The case studies also show that the accuracy of ice velocity estimates was significantly improved once the developed ionospheric correction techniques were integrated into the data processing flow. We demonstrate that the proposed ionosphere correction outperforms the traditionally-used approaches such as the averaging of multi-temporal data and the removal of obviously affected data sets. For instance, it is shown that about one hundred multi-temporal ice velocity estimates would need to be averaged to achieve the estimation accuracy of a single ionosphere-corrected measurement.

In Chapter 4, we evaluate the necessity and benefit of ionospheric-correction for L-band InSAR-based permafrost research. In permafrost zones, InSAR-based surface deformation measurements are used together with geophysical models to estimate permafrost parameters such

as active layer thickness, soil ice content, and permafrost degradation. Accurate error correction is needed to avoid biases in the estimated parameters and their co-variance properties. Through statistical analyses of a large number of L-band InSAR data sets over Alaska, we show that ionospheric signal distortions, at different levels of magnitude, are present in almost every InSAR dataset acquired in permafrost-affected regions. We analyze the ionospheric correction performance that can be achieved in permafrost zones by statistically analyzing correction results for large number of InSAR data. We also investigate the impact of ionospheric correction on the performance of the two main InSAR approaches that are used in permafrost zones: (1) we show the importance of ionospheric correction for permafrost deformation estimation from discrete InSAR observations; (2) we demonstrate that ionospheric correction leads to significant improvements in the accuracy of time-series InSAR-based permafrost products.

Chapter 5 summarizes the work conducted in this dissertation and proposes next steps in this field of research.

Table of Contents

List of Figures

Page

List of Tables

Page

Acknowledgments

This thesis would not have been possible without the support from many people.

I would like to express my heartfelt appreciation to my advisor Dr Franz Meyer, for his inspiration, guidance and support for the past six years. He is such a knowledgeable person on SAR, his insight, vision is fundamental for shaping this thesis. The fruitful discussion and constructive feedback and suggestion from him has helped me a lot to grow to a professional scholar. I am always thankful for his hard working for securing sufficient funding allowing me to attend conferences and seminar that interested me. He took the pressure but never mentioned it, and he is always so supportive for every opportunity that could benefit me.

My gratitude goes to my committee members Dr Jeffrey Freymueller, Dr Carl Tape and Dr Brenton Watkins. I am very thankful for their time and guidance, and helpful advice for career development.

During my Ph.D, I am fortunate to have the opportunity to collaborate with many excellent scholars, including Dr Eric Rignot, Dr Ian Joughin, Dr Bernd Scheuchl, Dr Jeremie Mouginot and Dr Lin Liu. I learned a lot from them and their cooperation are of great importance for the completion of this thesis. I want to thank Eric Rignot for inviting me to his group for a three weeks visit, and Bernd Scheuchl for coordinating the whole trip. The three weeks at UCI with Eric, Bernd and Jeremie was a productive and memorable time. I want to thank the Alaska Satellite Facility (ASF) for their great service of providing freely accessible SAR data. My sincerely gratitude goes to Mr. Scott Arko from ASF for providing unconventional SAR product, which is not his responsibility, but he was willing to spend his time working on it. I want to thank Giorgio Gomba for the helpful discussion about SAR and ionosphere technique.

I want to thank my colleagues at the Geophysical Institute, UAF. Special thanks go to Wenyu Gong for her assistance for helping me to get adapted to Alaskan life at the early days when I just arrived Fairbanks. I want to thank David McAlpin. He is always there whenever I need for help. I want to thank my other colleagues Olaniyi Ajadi, Oliver Dammann and Alex Sacco for their support and help.

Lastly, my deepest gratitude goes to my parents and my sister for their unconditional support and love. I want to thank my aunt and my uncle for their support and encouragement. I dedicate this thesis to my wife, Shanshan Li, for her love, support, and to our lovely daughter Miranda.

Chapter 1
Introduction

1.1 Background

Forty years have passed since the launch of the first spaceborne synthetic aperture radar (SAR) satellite Seasat by NASA. After forty year's development and growth, SAR/InSAR has finally become another mainstream technique following the glory of GPS, and has been widely used in a range of geophysical applications such as monitoring of glaciers, permafrost zones, earthquakes, volcanos, and landslides and so on (Bürgmann et al., 2000; Massonnet and Feigl, 1998).

Following the success of Seasat, many other SAR sensors, such as the legacy ERS-1/2, RADARSAT, ALOS PALSAR, TerraSAR-X, were developed and launched. Among these satellites, it is especially the SAR sensors operating at low-frequencies such as L-band (~24cm wavelength) or P-band (~60cm wavelength) that have attracted increasing attention. This is largely due to the higher penetration into vegetation volumes and the improved interferometric coherence that is offered by these sensors. This situation is especially important for the analysis of geophysical environments such as glaciers and permafrost, whose relevant scattering interfaces often undergo significant seasonal change (such as vegetation growth, snow accumulation and melt, and so on) (Joughin et al., 2010; Rignot et al., 2011; Rykhus and Lu, 2008; Short et al., 2011). Despite these benefits, however, low-frequency SAR data suffers from a higher sensitivity to ionospheric distortions (Xu et al., 2004).

1.2 Ionospheric Effects on SAR/InSAR Data

The ionosphere is a mixture of electrons, ions, and molecules in a layer at an altitude ranging between several tens of km to more than 1,000 km above the Earth's surface. The ionosphere density is strongly affected by solar activity and its distribution is controlled by the magnetic field and convection, storms and other meteorology activity (reference, Pi, et al, 2011). The ionosphere can introduce a variety of distortions, such as azimuth/range image geometric distortions, phase advance, Faraday rotation, amplitude and phase scintillation, as well as image resolution degradation in low-frequency SAR data. A wide range of SAR-based studies, including both C- and L-band data, have reported enormous ionospheric effects (Feng, 2011; Gray et al., 2000; Liao et al., 2018; Mattar and Gray, 2002; Raucoules and de Michele, 2010; Rykhus and Lu, 2008). The ionosphere is a function of solar cycle, geographical location, time (seasonal and

diurnal). Ionospheric irregularities predominantly happen in the aurora zones, the polar caps, and the postsunset geomagnetic equatorial region (Fejer and Kelley, 1980; Perkins, 1975). Thus, applying the InSAR technique, especially using low frequency data, at high latitude is at high risk of strong ionospheric distortion.

When a SAR signal traverses the ionosphere, its refractive index becomes (Meyer et al., 2006):

$$n_{iono} = \sqrt{1 - \frac{e_l^2}{4\pi^2 m\epsilon_0}\frac{n_e}{f^2}} \approx 1 - \frac{1}{2}\frac{e_l^2}{4\pi^2 m\epsilon_0}\frac{n_e}{f^2} = 1 - \mathrm{K}\frac{n_e}{f^2} \quad (1.1)$$

Where $\mathrm{K} = 40.28\ {}^{m^3}/_{s^2}$, e_l is the elementary charge, m is the electron mass, and ϵ_0 is the dielectric permittivity of vacuum. Eq. (1.1) shows that the refractive index is a function of electron density and the radar system's center frequency. What's more, we can see the refractive index is smaller than one, implying that the phase velocity in the ionosphere is higher than the vacuum speed of light. Hence, the corresponding phase and group velocity becomes,

$$v_{ph} = \frac{c}{n} = \frac{c}{1 - K\frac{n_e}{f^2}} \quad (1.2)$$

$$v_{gr} = cn = c(1 - \frac{Kn_e}{f^2}) \quad (1.3)$$

1.2.1 Faraday Rotation

When a linearly polarized radar signal traverses the ionosphere, which is immersed in the geomagnetic field, the polarized signal will be split to a left and right circular polarized wave that propagate at slightly different speeds. These slightly different speeds introduce a relative phase shift, resulting in a rotation of the orientation of a wave's linear polarization (Faraday rotation). The magnitude of this rotation in one way for a signal with frequency f that transverses ionosphere within a thickness h in radians is (Wright et al., 2003)

$$\Omega = \frac{K}{f^2}\int_0^H N_e B\cos\psi\sec\theta\, dh \quad (1.4)$$

Where B is the geomagnetic filed value, N_e is the electron density, and ψ is the cross-angle between wave prorogation and the earth's magnetic field, θ is the incidence angle. A good approximation to Eq. (1.4) is given by (Wright et al., 2003):

$$\Omega = \frac{K}{f^2} * \overline{B cos\psi sec\theta} * TEC \quad (1.5)$$

Where the total electron content (TEC) is defined as:

$$\mathrm{TEC} = \int_0^H N_e dh \quad (1.6)$$

As we see in Eq. (1.5), the magnitude of the Faraday rotation depends on several factors, such as the ionosphere activity (measured by TEC), the radar carrier frequency *f*, the incident angle θ of the radar signal, the strength of the geomagnetic field, and the orientation ψ of the geomagnetic field relative to radar signal propagation direction.

To get a quantitative magnitude of the Faraday rotation for an L-band SAR system, we calculated the FR angle of four different latitude locations on earth (details included in Table 1.1), using the configuration of the ALOS PALSAR SAR system (Table 1.1) and assuming an average ionospheric electron density of 40 TECU (1 TEC unit $\approx 10^{16}\ {electrons}/{m^2}$) (Meyer, 2011). In this calculation, the ionosphere is assumed to be a single thin layer at a height of 400 km (Meyer and Nicoll, 2008b). We assume a satellite carrier frequency of $f = 1.27\ GHz$ observing at an incidence angle of $\theta = 21.5^{\circ}$. The geomagnetic field is calculated from an international geomagnetic field model (Finlay et al., 2010) and its cross-angles ψ with incidence angle direction for the four different locations are shown in Table 1.1. The Faraday rotations at these four places under the above condition are listed in Table 1.1.

Table 1.1 Faraday rotation angle at different latitudes under an ionospheric magnitude of 40 TECU

Locations (Lat, Lon)	ALOS-1 PALSAR data	Cross-angle ψ (degree)	Faraday rotation angle Ω (degree)
Malaysia (5.0, 101.0)	ALPSRP276510090	94.1	-0.9
California, USA (34.8, -118.5)	ALPSRP187470690	29.0	12.9
Greenland 1 (65.2, -40.2)	ALPSRP068551310	25.8	15.2
Greenland 2 (81.5, -57.5)	ALPSRP257301670	21.8	16.3

From Table 1.1 we see that the cross-angle ψ between the magnetic field and the radar look direction is close to perpendicular for areas near the geomagnetic equator (e.g., Malaysia) resulting in a near-zero Faraday rotation angle even during high ionospheric electron density; the cross-angle decreases, and Faraday rotation angle increases with the increase of (geomagnetic) latitude. According to Meyer (2011), Faraday rotation should be smaller than $\Omega = 1.2$ degree for polarimetric applications. Obviously, this is problematic at middle and high latitude.

Faraday rotation effects could also be problematic for polarimetric and interferometric SAR application (Freeman and Saatchi, 2004; Rignot, 2000; Wright et al., 2003). It can bring a large drop of signal-to-noise ratio (SNR) and may result in radiometric calibration errors (Freeman and Saatchi, 2004). Experiments showed that phase coherence is reduced up to 33% when Faraday

rotation changes in InSAR data (Rignot, 2000). Also a differential phase will be brought to InSAR data because of differences in penetration depth between horizontal and vertical polarization signals (Rignot, 2000).

1.2.2 Phase Shift and Group Delay

In the following, a quantitative description of a range of ionospheric effects on SAR images is derived. The effective phase-path length from the satellite to the ground is given by:

$$P = \int_0^S n dl \quad (1.7)$$

Where n is the refractive index, s stands for the distance from satellite to ground object. The change Δl in the phase-path length (in a round-trip) introduced by the presence of ionosphere is given by according to Eq. (1.1):

$$\Delta l = 2\int_0^S (n-1)dl = 2\int_0^S \frac{-Kn_e}{f^2} dl = \frac{-2K}{f^2}\int_0^S n_e dl = \frac{-2K}{f^2} TEC \quad (1.8)$$

The phase shift (or phase advance) corresponding to the ionospheric effect is:

$$\Delta\emptyset_{iono} = -2\pi f\frac{\Delta l}{c} = \frac{4\pi K}{cf} TEC \quad (1.9)$$

Eq. (1.10) is derived under the assumption of a monochromatic signal, a chirp signal however is often used in SAR system. For a chirp signal, a Taylor series approximation of the phase shift is expressed as:

$$\Delta\emptyset_{iono} = \frac{-4\pi K}{cf_0} TEC + \frac{4\pi K}{f_0^2} TEC(f - f_0) - \frac{4\pi K}{f_0^3} TEC(f - f_0)^2 \quad (1.10)$$

The group delay is defined as the rate of change of phase angle with respect to frequency:

$$\tau_{gr} = -\frac{1}{2\pi}\frac{d\emptyset_{iono}}{df} = \frac{2K}{cf_0^2} TEC \quad (1.11)$$

Using the following typical SAR system specifications in Table 1.2 (ESA, 2014; Canadian space Agency, 2014), 1 TECU ionosphere induced phase shift for different SAR system is shown in Table 1.2.

As we can see from Table 1.2, one TECU of ionospheric electron content will introduce half phase cycle in C-band and 2.12 phase cycle for L-band signals. This is not acceptable for many geophysics applications, like post-seismic deformation or volcanic deformation. A spatially varying ionosphere with a mean deviation exceeding 1 TECU is very likely to occur if the images used for InSAR processing were acquired at different times.

Table 1.2 1 TECU Ionospheric induced phase shifts for typical SAR systems

Parameters	Radar		
	Radarsat-2 (C-band)	ALOS-1(L-band)	Biomass (P-band)
Center Frequency	5.405 GHz	1.27 GHz	435 MHz
Bandwidth	100 MHz	14 MHz	6 MHz
Phase shift	0.50 Phase cycle	2.12 Phase cycle	6.16 Phase cycle

1.2.3 Azimuthal Image Shifts

To discuss the ionospheric effects on SAR image quality, we need to briefly address the SAR image formation process, in which the signal processing procedures make ionospheric effects more complicated. A typical linear frequency-modulated signal (usually named a chirp signal) used in SAR systems is shown in Figure 1.1 (a-e). When the transmitted chirp signal returns after its interaction with the ground, a convolution of the reference signal (conjugate of the chirp signal) with this echo will generate a range compressed image. For illustration, the range impulse response of a point scatter after range compression is shown in Figure 1.1 (f). Through the process of range compression, high-resolution imaging capabilities are achieved (narrow beam width of the signal) in range direction. In azimuth, the movement of the satellite changes the distance between the satellite and ground object, which generates a pseudo-chirp signal. We get the focused high-resolution pixel similar to the process in range direction. A synthetic reference signal is created based on satellite orbit information and used to compress the image information in azimuth using a matched filter process.

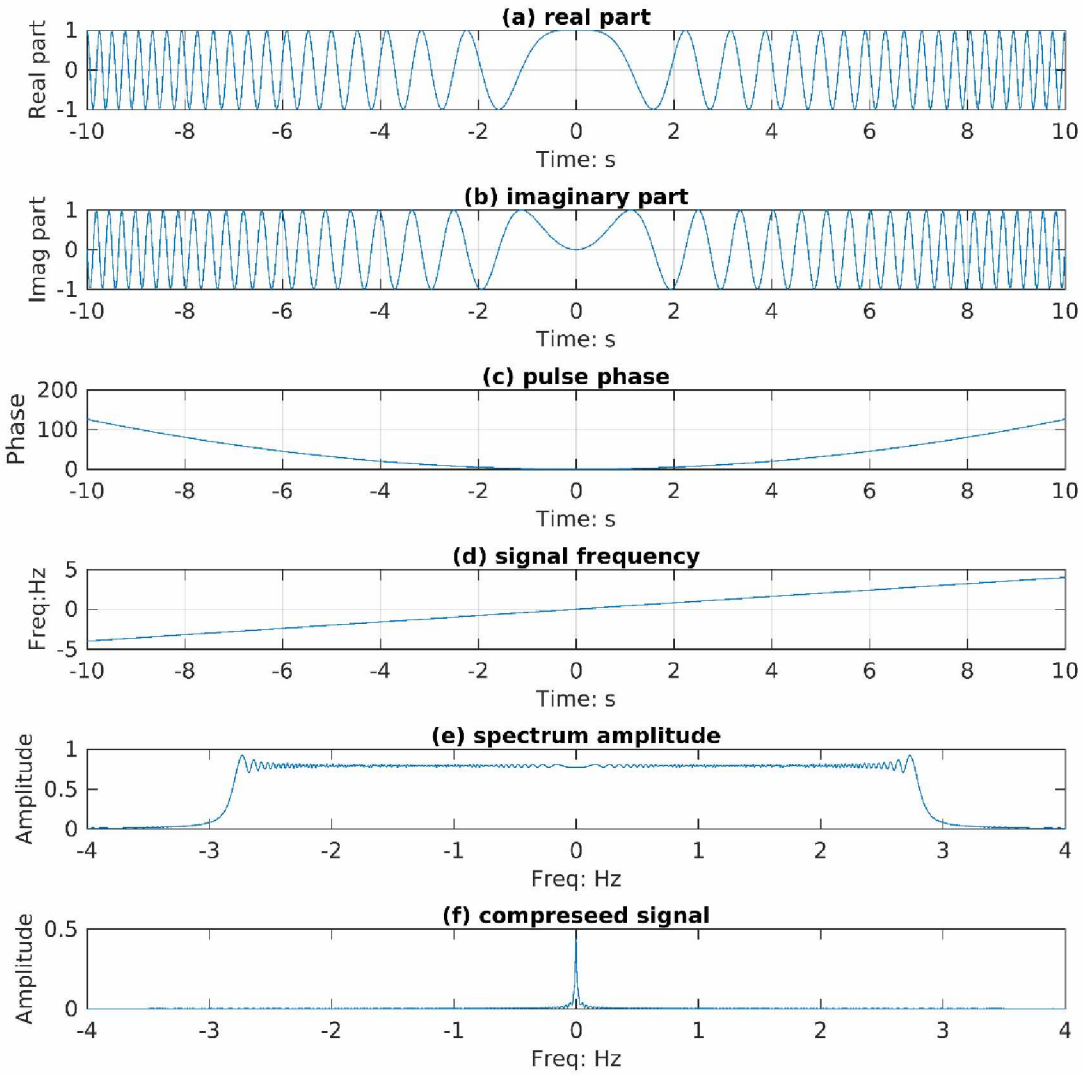

Figure 1.1 A typical chirp signal and the corresponding compressed signal.(a) Real part of the chirp signal. (b) Imaginary part of the chirp signal. (c) Phase variation with time of the chirp signal. (d) Frequency vs time of the chirp signal. (e) Spectrum amplitude.

The above case is an ideal situation without considering ionospheric effects. The ionosphere leads to a phase shift of the transmitted signal that will be different for different parts of the chirp signal both in range and azimuth. Distortions of the range chirp are due to the dispersivity of the ionosphere. Distortions of the azimuth chirp are related to spatial variations of the ionospheric phase delay. Both effects will degrade the performance of image compression and

leads to different kinds of SAR image distortions such as range/azimuth shifts, range/azimuth resolution degradation, as well as image amplitude scintillation.

An inhomogeneous ionosphere with significant TEC variation within the length scale of the synthetic aperture could cause phase gradients across the aperture resulting in azimuthal shifts of the affected areas in a focused SAR image. An equation describing such shifts was derived in several papers (Chen and Zebker, 2014; Meyer, 2011) and can be expressed as:

$$\frac{d\emptyset_{iono}}{dT} = \frac{d\frac{4\pi K}{cf}TEC}{dT} = \frac{4\pi K}{cf}\frac{dTEC}{dT} \qquad (1.12)$$

$$\Delta\alpha = \frac{d\theta_{iono}}{dT}\frac{v_{sat}}{FM} = \frac{4\pi K}{cf}\frac{dTEC}{dT}\frac{v_{sat}}{FM} = \frac{4\pi K}{cf}\frac{dTEC}{v_{sat}*dT}\frac{v_{sat}^2}{FM} = \frac{4\pi K}{cf}\frac{\mathrm{dTEC}}{\mathrm{dR_{az}}}\frac{\mathrm{v_{sat}^2}}{\mathrm{FM}} \qquad (1.13)$$

Where $\mathrm{v_{sat}}$ is satellite velocity, FM is azimuth frequency modulation rate of the system. If the ionosphere-induced phase gradient is constant for every pixel of an image, then the image will suffer from a constant azimuth shift, otherwise variable azimuth shifts will occur leading to geometric distortions across the whole image.

With the configuration parameters of ALOS PALSAR PLR data, an approximation for the satellite velocity of 7.5 km/s, and a zero-Doppler range R_0 of 700 km, a TEC gradient of 1TEC/100 km, which is very likely to happen in ionosphere event, will introduce an azimuth shift of 11.4 m for a zero squint angle acquisition, corresponding to approximately 3 pixels at the ALOS PALSAR azimuth resolution.

This ionosphere-induced azimuth shift has been observed in both C-band and L-band SAR data (Gray et al., 2000; Joughin et al., 1996; Meyer and Nicoll, 2008a), in particular in data acquired at higher latitudes. Local azimuth shifts cause coherence loss due to registration mismatch in interferometric SAR application (Meyer, 2011).

1.2.4 Range Image Shifts

As seen in Eq. (1.11), the ionosphere induces a group delay that may measurably affect the range location of a geocoded image. The linear term in the Taylor series expansion of the ionosphere-induced phase shift (Eq. (1.10)) will introduce a range shift in focused SAR images, which can be expressed by:

$$\Delta r = \tau_{gr} \cdot \frac{c}{2} \qquad (1.14)$$

For an L-band SAR, $1TECU$ will induce 0.25 m range shift, which is 0.0255 pixels for a PALSAR range resolution cell of about 9.8 m. An average of 40 TECU will induces 1-pixel shift in the range direction of the image. Range shifts for different sensor frequencies are shown in

Table 1.3. Spatially varying range shifts also distort SAR image geometry and causes coherence loss in InSAR applications.

Table 1.3 1 TECU Ionosphere-induced range shifts in typical SAR system

	Radarsat-2 (C-band)	ALOS-1 (L-band)	Biomass (P-band)
Center Frequency	5.405 GHz	1.27 GHz	435 MHz
Range shift	0.014 m	0.25 m	2.13 m

1.2.5 Resolution Degradation

Due to the dispersive property of the ionosphere, different parts of the transmitted range chirp will experience slightly different phase advance based on their different frequencies. An approximate summative phase error can be derived based on Eq. (1.10).

Terms of higher order can be omitted since the error related to cubic term of the Taylor series does not exceed 0.5 degree, even for low frequency and wide bandwidth systems (Meyer et al., 2006). The quadratic term in Eq. (1.10) changes the chirp rate and, if uncompensated, leads to a discrepancy between the received chirp echo and the chirp used for image compression. This discrepancy would reduce focusing performance in range direction (image blur in range).

A simple way to measure resolution degradation in range direction consists of estimating the spread $\Delta\tau$ of the transmitted/received pulse at the chirp signal edge using Eq. (1.11) (Kim, 2014)

$$\Delta\tau = \frac{2K}{c(f_c-\frac{W}{2})^2}TEC - \frac{2K}{c\left(f_c+\frac{W}{2}\right)^2}TEC = 2K\frac{TEC}{c}\frac{2f_cW}{(f_c^2-\frac{W^2}{4})^2} \qquad (1.15)$$

As seen in Eq. (1.15), $\Delta\tau$ depends on the radar's bandwidth W and center frequency f_c as well as the TEC value of the ionosphere. Using the parameters of ALOS PALSAR polarimetric (PLR) data, where $f_c = 1.27 \times 10^9 Hz$, $W = 14 \times 10^6$Hz and a pulse repetition frequency (PRF) $PRF = 1915.7\,Hz$, range defocusing can be calculated as a function of TEC. For an average ionosphere of 40 TECU, the pulse spreading $\Delta\tau$ is only 1.48 ns. Comparing to the original chirp signal duration of 522 us, this effect remains unnoticeable such that range resolution degradation from the ionosphere for an L-band SAR system is negligibly small.

Similarly, small scale ionosphere variation in the synthetic aperture can introduce a defocusing effect in the azimuth direction of a SAR image. This azimuth defocusing effect is related to a variation of the first right-hand term of Eq. (1.10) along the flight track. As a range chirp signal always 'sees' a constant ionosphere while the azimuth pseudo-chirp signal 'sees' a spatially variable ionosphere which can be inhomogeneous, the azimuth direction is more sensitive

to the ionospheric variation. The phase shift induced by inhomogeneous ionosphere can lead to a degradation of the azimuth image resolution. However, research has shown that the ionosphere is unlikely to significantly degrade L band SAR image azimuth resolution (Meyer, 2011).

1.2.6 Image Intensity Scintillation

Shimada et al., (2008) reported the discovery of stripe features in ALOS PALSAR data acquired over the Amazon area. By correlating these features with GPS data they concluded that these stripes were introduced by ionospheric scintillation. Simulation results also confirmed this initial assessment and calculated the likelihood for scintillation-induced striping effects globally. It was found they that are most likely to occur at low geomagnetic latitudes (Meyer et al., 2016).

1.2.7 Summary

We summarized and reviewed the most typical ionospheric effects in SAR and InSAR data. Ionospheric effects in SAR, especially for low-frequency data have been recognized as an important error source (Meyer et al., 2006; Meyer, 2010; Wegmuller et al., 2006; Xu et al., 2004), however, developing effective tools for estimating and correcting ionosphere-induced distortions is still at an early age and reliable tools for compensating ionospheric effects are still in great need. The need for robust ionospheric correction tools is further evidenced by the large number of upcoming SAR systems operating at L-band such as NISAR, BIOMASS, Tandem-L, SAOCOM.

The main objectives of this study are to develop a robust and effective algorithm for ionospheric correction of InSAR data and to evaluate its performance in real geophysical applications such as permafrost deformation monitoring and glacier velocity tracking.

1.3 Thesis Structure

The thesis consists of three main chapters, plus this introduction and a concluding chapter. My main contributions in Chapter 2 are that I developed a robust and accurate split spectrum-based approach for InSAR ionospheric correction, and I demonstrated its performance through case study. In this study, I thoroughly examined the practical implementation of the split spectrum technique and provided improved and more robust solutions. I discuss the case of InSAR data with large perpendicular baselines and incorporate the related spectral shift effect into the mathematical model used for ionospheric correction. I show that this addition leads to a significant increase in the split spectrum performance for InSAR ionospheric correction for data with large perpendicular baselines. In addition, I propose a least squares-based multiple sub-band solution for ionospheric correction. This expanded approach increases the robustness and accuracy of correction results,

especially for data with unfavorable coherence conditions. I conceived the study with help from my advisor Dr Franz Meyer, conducted all experiments, did initial result analysis, and wrote the draft paper.

Chapter 3 presents our work on implementing the techniques in Chapter 2 for glacier ice velocity tracking in both Greenland and Antarctica. I demonstrate that the ionosphere is an important error source for ice velocity tracking with L-band InSAR data: ionospheric errors in the interior of Greenland and Antarctica can be larger than the real ice motion signal. I show that the split spectrum technique is an effective approach for the correction of SAR-derived ice velocity measurements for ionospheric influence. The study also demonstrates that the split spectrum technique outperforms the traditionally used multiple temporal data averaging approach. I demonstrate that 100 InSAR measurements would be needed for the temporal average approach to achieve the performance of only a single InSAR observation with split spectrum correction applied. Antarctic SLC datasets and reference ice velocities are provided by my co-author Eric Rignot's group through Jeremie Mouginot. Greenland experiment SLC data are provided by co-author Ian Joughin. The standard deviations compared to reference data for Greenland were calculated by Ian Jouphin. I conducted all experiments, performed result analysis, and wrote the paper draft.

In Chapter 4, I apply the developed ionosphere correction tool to a permafrost deformation study. I demonstrate that ionosphere is an important error source when using InSAR for permafrost research in Northern Alaska. I demonstrate the effectiveness of the developed ionosphere correction technique. Through ionospheric correction, I show that a significantly improved estimate of permafrost dynamics in a tundra fire region can be achieved. In addition, it is shown that after ionospheric correction, short term variations of permafrost deformation can be revealed that was previously inaccessible due to accuracy limitations. I also show that the ionospheric correction improves the accuracy of time series InSAR approach for permafrost deformation estimation. I conceived the whole study with input from Dr Franz Meyer and Dr Lin Liu, conducted all experiments, did initial result analysis and wrote the paper draft.

All the studies were conducted under the supervision of my Ph.D. advisor Dr. Franz J. Meyer. All co-authors of the abovementioned three main chapters contributes to discussion, results analysis and paper revision.

In Chapter 5, I summarize the main finding in this thesis and discuss the possible future work.

1.4 References

Bürgmann, R., Rosen, P.A., Fielding, E.J., 2000. Synthetic aperture radar interferometry to measure Earth's surface topography and its deformation. Annual review of earth and planetary sciences 28, 169–209.

Chen, A.C., Zebker, H.A., 2014. Reducing Ionospheric Effects in InSAR Data Using Accurate Coregistration. IEEE Transactions on Geoscience and Remote Sensing 52, 60–70. https://doi.org/10.1109/TGRS.2012.2236098

Fejer, B.G., Kelley, M.C., 1980. Ionospheric irregularities. Reviews of Geophysics 18, 401–454.

Feng, G., 2011. Coseismic deformation and ionospheric variation associated with Wenchuan earthquake estimated from InSAR.

Finlay, C.C., Maus, S., Beggan, C.D., Bondar, T.N., Chambodut, A., Chernova, T.A., Chulliat, A., Golovkov, V.P., Hamilton, B., Hamoudi, M., others, 2010. International geomagnetic reference field: the eleventh generation. Geophysical Journal International 183, 1216–1230.

Freeman, A., Saatchi, S.S., 2004. On the detection of Faraday rotation in linearly polarized L-band SAR backscatter signatures. IEEE Transactions on Geoscience and Remote Sensing 42, 1607–1616. https://doi.org/10.1109/TGRS.2004.830163

Gray, A.L., Mattar, K.E., Sofko, G., 2000. Influence of ionospheric electron density fluctuations on satellite radar interferometry. Geophysical Research Letters 27, 1451–1454.

Joughin, I., Smith, B.E., Howat, I.M., Scambos, T., Moon, T., 2010. Greenland flow variability from ice-sheet-wide velocity mapping. Journal of Glaciology 56, 415–430.

Joughin, I., Winebrenner, D., Fahnestock, M., Kwok, R., Krabill, W., 1996. Measurement of ice-sheet topography using satellite-radar interferometry. Journal of Glaciology 42, 10–22.

Kim, J., 2014. Development of ionosphere estimation techniques for the correction of SAR data.

Liao, H., Meyer, F.J., Scheuchl, B., Mouginot, J., Joughin, I., Rignot, E., 2018. Ionospheric correction of InSAR data for accurate ice velocity measurement at polar regions. Remote Sensing of Environment 209, 166–180. https://doi.org/10.1016/j.rse.2018.02.048

Massonnet, D., Feigl, K.L., 1998. Radar interferometry and its application to changes in the Earth's surface. Reviews of Geophysics 36, 441–500. https://doi.org/10.1029/97RG03139

Mattar, K.E., Gray, A.L., 2002. Reducing ionospheric electron density errors in satellite radar interferometry applications. Canadian Journal of Remote Sensing 28, 593–600.

Meyer, F., 2010. A review of ionospheric effects in low-frequency SAR—Signals, correction methods, and performance requirements, in: Geoscience and Remote Sensing Symposium (IGARSS), 2010 IEEE International. IEEE, pp. 29–32.

Meyer, F., Bamler, R., Jakowski, N., Fritz, T., 2006. The Potential of Low-Frequency SAR Systems for Mapping Ionospheric TEC Distributions. IEEE Geoscience and Remote Sensing Letters 3, 560–564. https://doi.org/10.1109/LGRS.2006.882148

Meyer, F.J., 2011. Performance Requirements for Ionospheric Correction of Low-Frequency SAR Data. IEEE Transactions on Geoscience and Remote Sensing 49, 3694–3702. https://doi.org/10.1109/TGRS.2011.2146786

Meyer, F.J., Chotoo, K., Chotoo, S.D., Huxtable, B.D., Carrano, C.S., 2016. The influence of equatorial scintillation on L-band SAR image quality and phase. IEEE Transactions on Geoscience and Remote Sensing 54, 869–880.

Meyer, F.J., Nicoll, J., 2008a. The impact of the ionosphere on interferometric SAR processing, in: Geoscience and Remote Sensing Symposium, 2008. IGARSS 2008. IEEE International. IEEE, pp. II–391.

Meyer, F.J., Nicoll, J.B., 2008b. Prediction, Detection, and Correction of Faraday Rotation in Full-Polarimetric L-Band SAR Data. IEEE Transactions on Geoscience and Remote Sensing 46, 3076–3086. https://doi.org/10.1109/TGRS.2008.2003002

Perkins, F.W., 1975. Ionospheric irregularities. Reviews of Geophysics 13, 884–884.

Raucoules, D., de Michele, M., 2010. Assessing Ionospheric Influence on L-Band SAR Data: Implications on Coseismic Displacement Measurements of the 2008 Sichuan Earthquake. IEEE Geoscience and Remote Sensing Letters 7, 286–290. https://doi.org/10.1109/LGRS.2009.2033317

Rignot, E., Mouginot, J., Scheuchl, B., 2011. Ice flow of the Antarctic ice sheet. Science 333, 1427–1430.

Rignot, E.J., 2000. Effect of Faraday rotation on L-band interferometric and polarimetric synthetic-aperture radar data. Geoscience and Remote Sensing, IEEE Transactions on 38, 383–390.

Rykhus, R.P., Lu, Z., 2008. InSAR detects possible thaw settlement in the Alaskan Arctic Coastal Plain. Canadian Journal of Remote Sensing 34, 100–112.

Shimada, M., Muraki, Y., Otsuka, Y., 2008. Discovery of anomalous stripes over the Amazon by the PALSAR onboard ALOS satellite. Proc. IEEE IGARSS, pp II-387–II-390.

Short, N., Brisco, B., Couture, N., Pollard, W., Murnaghan, K., Budkewitsch, P., 2011. A comparison of TerraSAR-X, RADARSAT-2 and ALOS-PALSAR interferometry for monitoring permafrost environments, case study from Herschel Island, Canada. Remote Sensing of Environment 115, 3491–3506. https://doi.org/10.1016/j.rse.2011.08.012

Wegmuller, U., Werner, C., Strozzi, T., Wiesmann, A., 2006. Ionospheric electron concentration effects on SAR and INSAR, in: Geoscience and Remote Sensing Symposium, 2006. IGARSS 2006. IEEE International Conference On. IEEE, pp. 3731–3734.

Wright, P.A., Quegan, S., Wheadon, N.S., Hall, C.D., 2003. Faraday rotation effects on l-band spaceborne sar data. IEEE Transactions on Geoscience and Remote Sensing 41, 2735–2744. https://doi.org/10.1109/TGRS.2003.815399

Xu, Z.-W., Wu, J., Wu, Z.-S., 2004. A survey of ionospheric effects on space-based radar. Waves in Random Media 14, S189–S274.

Chapter 2

On the Practical Implementation of Split Spectrum Technique for Interferometric SAR Ionospheric Effect Correction[1]

2.1 Abstract

Split spectrum InSAR has been proven to be an effective approach for InSAR ionospheric correction in selected case studies. This technique however has not yet been tested for its robustness in unfavorable imaging conditions such as interferometric configurations with large spatial baselines and data with low coherence. Our study analyzes the impact of spectral shifts related to large interferometric baselines on split spectrum InSAR for ionosphere estimation and we propose to include this effect in the mathematical model used for sub-band selection in split spectrum InSAR. In contrast to traditional approaches, which use only a part of the available spectral information, we propose a multiple sub-band approach, which utilizes all the available spectrum information for estimating the ionospheric impact on the SAR phase observables. In addition to improving estimation accuracy, we show that this multiple sub-band approach improves the robustness of the ionosphere estimation through the availability of redundant information. In case studies we show that including the spectral shift effect increases sub-band coherence and ionosphere estimation accuracy for data with a large perpendicular baseline. The proposed multiple sub-band approach provides a cleaner ionosphere estimate and visually improved ionospheric correction. Quantitative analysis confirms that it provides ionospheric estimates with better accuracy.

2.2 Introduction

Interferometric Synthetic Aperture Radar (InSAR) has become an important tool for monitoring topography and deformation, and it has been widely used in geophysical studies such as earthquake deformation, volcano monitoring, landslide detection, ice sheet dynamic mapping, permafrost studies and many more (Bürgmann et al., 2000; Joughin, 2002; Liu et al., 2010; Massonnet and Feigl, 1998). Recent studies with spaceborne InSAR have identified the ionosphere as an important error source, limiting the performance of InSAR in many areas. While this is especially true for low-frequency SAR systems operating in L-band and P-band (Hashimoto et al., 2010; Iwahana et al., 2016; Joughin et al., 2010; Natsuaki et al., 2016; Raucoules and de Michele,

[1] Liao, H., Meyer, F. J. (2018), On the practical implementation of split spectrum technique for Interferometric SAR Ionospheric effect correction. Prepared for submission to IEEE Transactions on Geoscience and Remote Sensing.

2010; Rignot et al., 2011; Tong et al., 2010), ionospheric artifacts have also been identified as a significant error source in C-band (Gray et al., 2000; Rykhus and Lu, 2008) and even some X-band SAR images (Prats-Iraola et al., 2015; Yague-Martinez et al., 2016). Low-frequency radars, with their ability for deep canopy penetration and retaining good coherence for data even separated for several years, are becoming increasingly popular and several low-frequency SAR missions such as the NASA-ISRO SAR mission (NISAR), Tandem-L, and the P-band Biomass mission are expected to be launched in the near future. Therefore, ionospheric correction techniques for InSAR observations are becoming a particularly important topic.

Several studies on the nature of ionospheric effects in SAR data (Gray et al., 2000; Meyer and Nicoll, 2008; Xu et al., 2004) and on techniques estimating and compensating ionospheric signals from SAR/InSAR observations (Brcic et al., 2011, 2010; Freeman, 2004; Gomba et al., 2016; Kim, 2014; Meyer et al., 2006; Rosen et al., 2010) have emerged during the last ten years. One subgroup of ionospheric correction approaches uses external ionosphere information, typically derived from GPS data or ionospheric models, to correct the ionospheric effects in SAR data (Gomba et al., 2017; Tong and Sandwell, 2009.). These methods are usually hindered by the limited spatial resolution and insufficient absolute accuracy of currently available ionospheric information and are, thus, of only limited applicability (Gomba et al., 2017; Tong and Sandwell, 2009.). The other group of ionosphere correction techniques utilizes the ionospheric distortion in the SAR data itself to identify and correct SAR observations. Under this category, three popular techniques have been introduced: the Faraday rotation-based method (Freeman, 2004; Kim et al., 2015; Meyer et al., 2013), the azimuth shift-based method (including the MAI based approach) (Hu et al., 2012; Jung et al., 2013; Jung and Lee, 2015; Z. Liu et al., 2014) and the azimuth shift based approach (Chen and Zebker, 2014; Meyer et al., 2006; Raucoules and De Michele, 2010; Zhang et al., 2016)), and the family of split spectrum techniques (Brcic et al., 2011, 2010; Fattahi et al., 2017; Gomba et al., 2016; Rosen et al., 2010). Requirements for the performance of ionospheric correction techniques were formulated in Meyer (2011).

The Faraday rotation-based method is a classic and effective technique for ionospheric estimation and correction (Freeman and Saatchi, 2004; Kim and Papathanassiou, 2010; Rogers and Shaun Quegan, 2014), however, the quad-polarimetric data that are required for this algorithm are rare and often only available for a small portion of a sensor's data collections. Furthermore, the accuracy of Faraday rotation-based ionospheric estimates becomes less reliable as data

approach the geomagnetic equator, raising concerns about the global applicability of this technique. While azimuth shift-based techniques have become popular in recent years (Jung et al., 2013; Jung and Lee, 2015; Kim, 2014; Raucoules and de Michele, 2010; Zhang et al., 2016), they still suffer from several issues: 1) Effective and robust methods for the separation of ground motion-induced and ionosphere-induced azimuthal shifts still need to be further studied, although some initial work is evolving (Kim and Papathanassiou, 2015);2) this family of techniques is insensitive to ionospheric variation in the range direction (Chen and Zebker, 2014; Gomba and De Zan, 2015); 3) as the relationship between ionospheric structure and related azimuth shifts depends on the altitude of the observed ionospheric anomaly, the results from this technique can be inaccurate (Gomba and De Zan, 2015).

The split spectrum technique, usually dividing the full SAR range spectrum into non-overlapping sub-bands, forms several interferograms with the corresponding sub-bands of the master/slave data. These interferograms have slightly different center frequencies and, thus, experience a slightly different phase advance when traveling through the ionosphere. By exploring this phase difference, the differential ionosphere signal can be retrieved. The initial concept and limited case studies using this technique for interferometric SAR ionosphere estimation and correction were published in (Brcic et al., 2011, 2010; Rosen et al., 2010). As the typically narrow bandwidth limits the frequency separation of the extracted sub-band data, the differential signal among the sub-band interferograms is small. To retrieve the ionosphere, this small differential signal has to be scaled up by a large constant factor, which also exaggerates the noise inherent to the data. Therefore, estimating the ionosphere signal from SAR data using the split spectrum approach is challenging and sensitive to processing errors such as image mis-registration, low signal-to-noise ratios, phase unwrapping errors, radio-frequency interference, and more. A recent publication by Gomba et al., (2016) makes an important contribution toward improving the robustness of split spectrum InSAR by incorporating some error mitigation techniques into the split spectrum implementation. Selected case studies in this paper show encouraging performance of split spectrum InSAR for data with sufficient coherence (Gomba et al., 2016). Fattahi et al. (2017) recently extended this technique into time series InSAR data analysis and further demonstrate its performance using GPS data validation.

Given the potential for operational processing of the split spectrum technique, we studied this technique extensively and applied it in different scenarios such as glacier velocity tracking,

permafrost subsidence and earthquake deformation (Liao et al., 2018, 2017; Liao and Meyer, 2016). In practical implementation, we found factors related to imaging geometry and signal quality that drives ionospheric correction performance and were not addressed in previous publications. If taken into consideration, these factors can further improve correction accuracy and robustness. For a dataset with large perpendicular baseline, the geometry-induced spectral shift can be large, reducing the available spectral bandwidth for ionospheric correction and reducing sub-band interferogram coherence if not properly considered in the processing workflow. In addition, previous approaches divide the full range spectrum into three non-overlapping sub-bands each with a bandwidth of one-third of the original full range bandwidth, and then use the lower and upper sub-band for the ionospheric estimate (Brcic et al., 2011, 2010; Gomba et al., 2016). This strategy utilizes only two thirds of the available total bandwidth and is therefore ignoring some available information that could be used to improve estimation accuracy and robustness. We propose a least-squares multiple sub-bands solution for ionosphere estimation which utilizes all available sub-band information. We identify two main advantages of this approach: (1) using all available spectral information combined with a proper covariance model can improve the robustness of ionospheric estimates; (2) by exploring the full range of possible sub-band combinations, an estimation result with higher accuracy can be achieved for all acquisition situations.

In the following section we first summarize the ionosphere effect on InSAR data and briefly introduce the conventional split spectrum InSAR approach with its advantages and limitations. We then discuss the spectral shift effect for large perpendicular baselines, and we propose to incorporate this shift effect in the process of sub-band generation for ionosphere estimation (Section 2.4.1). In Section 2.4.2, we propose a least-squares based multiple sub-bands solution for ionosphere estimation. We analyze its theoretic accuracy compared with conventional approach, and we also analyze the bandwidth effect of its accuracy in Section 2.4.3. We propose a pixel-based outlier detection approach under the framework of the multiple sub-bands solution in Section 2.4.5. We briefly summarize the steps for implementing this multiple sub-bands approach for ionosphere estimation 2.4.6. In Section 2.5, a case study is presented to validate our arguments. We end with a summary of our main findings and discuss the potential application of our proposed technique.

2.3 Split Spectrum InSAR Ionospheric Correction

2.3.1 Ionospheric Effects on InSAR Data

The ionosphere is a mixture of electrons, ions, and molecules in a layer at an altitude ranging between several tens of km to more than 1,000 km above the Earth's surface. The ionosphere density is strongly affected by solar activity and its distribution is controlled by the magnetic field and convection, storms and other meteorology activity (Pi et al., 2011). When a SAR signal traverses the ionosphere, two main effects are introduced to the signal: the polarimetric plane of the traversing signal is rotated (Faraday rotation) and the phase of the SAR observation is altered. Through the image formation process, these two effects cause a range of distortions in SAR images including polarimetric distortions, range/azimuth offsets, defocusing, decorrelation and InSAR phase artifacts (Xu et al., 2004).

2.3.2 Range Split Spectrum InSAR Ionosphere Estimation

The InSAR phase is a superposition of different phase components such as topography, troposphere, ionosphere, deformation and noise:

$$\emptyset_0 = \emptyset_{flat} + \emptyset_{topo} + \emptyset_{def} + \emptyset_{atmo} + \emptyset_{iono} \quad (2.1)$$

Where the flat earth phase can be written as $\emptyset_{flat} = \frac{4\pi}{c} B_{\parallel} \cdot f_0$, the topographic phase as $\emptyset_{topo} = \frac{-4\pi B_{\perp} h}{R\, c \sin\theta} \cdot f_0$, the deformation phase as $\emptyset_{def} = \frac{4\pi}{c} \Delta r \cdot f_0$ and the atmospheric delay as $\emptyset_{atmo} = \frac{4\pi}{c} \int Ndl \cdot f_0$. In these equations, $B_{\perp}$ is the perpendicular baseline, , $B_{\parallel}$ is the parallel baseline, h is the topographic height above a reference plane, R is the slant range distance between the satellite and antenna position of the master acquisition, θ is the incidence angle, c is the speed of light, f_0 is the radar center frequency, $\int Ndl$ is the integrated atmospheric refractivity along the path, and Δr is the surface deformation signal along the line-of-sight between the acquisition times of an InSAR data pair. The ionospheric phase in Eq. (2.1) can be described as (F. Meyer et al., 2006):

$$\emptyset_{iono} = \frac{4\pi K}{c f_0} \Delta TEC \quad (2.2)$$

Where ΔTEC is the difference in the ionospheric total electron content between the master and the slave image acquisition time, integrated along the line-of-sight, c is the light speed in vacuum, K is a constant with value 40.28 $m^3/_{S^2}$; and f_0 is the center frequency of the SAR signal.

As we can see, the flat earth phase $\emptyset_{flat}$, topographic phase $\emptyset_{topo}$, the tropospheric phase $\emptyset_{tropo}$, and the deformation phase $\emptyset_{def}$ are all linearly related to radar signal center frequency f_0.

Hence, these terms are usually categorized as the non-dispersive phase component: $\emptyset_{non-disp} = \frac{4\pi}{c} B_{\parallel} \cdot f_0 + \frac{-4\pi Bh}{R\,c \sin\theta} \cdot f_0 + \frac{4\pi \int \Delta n dl}{c} \cdot f_0 + \frac{4\pi}{c} \Delta r \cdot f_0$. In contrast, the ionospheric effect is inversely related to the center frequency ($\emptyset_{iono} = \frac{-4*K*\pi*\Delta STEC}{c*f_0}$) and is therefore categorized as a dispersive signal. Therefore Eq. (2.1) can be written as:

$$\emptyset_0 = \emptyset_{non-disp} \frac{f}{f_0} + \emptyset_{iono} \frac{f_0}{f} \quad (2.3)$$

SAR utilizes chirp signals centered at frequency f_0 with a bandwidth B_0. The split spectrum technique, utilizing the dispersive and non-dispersive property differences with respect to frequency, usually divides the range spectrum of a SAR signal into non-overlapping sub-bands with equal bandwidth but slightly different center frequencies.

Assuming the chirp signal bandwidth B_0 is divided into N sub-bands, then N sub-band interferograms can be generated between the corresponding master and slave sub-bands. The bandwidth of each sub-band will be $B_{sb} = \frac{B_0}{N}$, where B_0 is the full available range bandwidth and B_{sb} is the sub-bands bandwidth, $f_1, f_2, \ldots f_N$ are the center frequencies of the N sub-bands and the center frequency of the m^{th} sub-band ($m \in [1,2,3, \ldots, N]$) is

$$f_m = f_0 - \frac{\mathrm{B_0}}{2} + (m - \frac{1}{2})\mathrm{B_{sb}} = f_0 + \mathrm{B_0}(\frac{1}{2} - \frac{m-\frac{1}{2}}{N}) \quad (2.4)$$

Theoretically, using any two of the generated sub-bands is sufficient to derive the differential ionospheric phase from an available interferogram, using the following approach. The interferometric phase of the two selected sub-band interferograms can be written as

$$\emptyset_{iono} \frac{f_0}{f_1} + \emptyset_{non-disp} \frac{f_1}{f_0} = \emptyset_1 \quad (2.5)$$

$$\emptyset_{iono} \frac{f_0}{f_2} + \emptyset_{non-disp} \frac{f_2}{f_0} = \emptyset_2 \quad (2.6)$$

Connecting these two equations, the $\emptyset_{iono}$ and $\emptyset_{non-disp}$ can be derived as:

$$\emptyset_{iono} = \left(\emptyset_1 - \emptyset_2 \frac{f_1}{f_2}\right) \frac{f_2}{f_0} \frac{f_1 f_2}{(f_2^2 - f_1^2)} \quad (2.7)$$

$$\emptyset_{non-disp} = \left(\emptyset_1 - \emptyset_2 \frac{f_2}{f_1}\right) \frac{f_1 f_0}{(f_1^2 - f_2^2)} \quad (2.8)$$

where Eq. (2.7) expresses the targeted ionospheric phase that needs to be removed from the InSAR observations.

The accuracy of the sub-band interferometric phase dispersion equation (Bamler and Eineder, 2005) is

$$\sigma_{\emptyset_{sub-band}} = \frac{1}{\sqrt{2N_b}} \cdot \frac{\sqrt{1-\gamma_0^2}}{\gamma_0} \quad (2.9)$$

where $N_b = {Pix_N \cdot B_{sb}}/{B_0}$ stands for the number of pixels in a system with bandwidth B_{sb}. Pix_N stands for the number of pixels at the original full band data, which is decided by the multi-looking number. B_0 is the full bandwidth of the original data and $\gamma_{sub-band}$ is the sub-band interferometric coherence. As the sub-bands have equal bandwidth, it is reasonable to assume each sub-band interferogram has the same phase dispersion property that equals $\sigma_{\emptyset_{sub-band}}$.

Ionospheric phase estimation accuracy can be quantified as:

$$\sigma_{\emptyset_{iono}} = \frac{f_2}{f_0}\frac{f_1 f_2}{(f_2^2-f_1^2)}\sqrt{1+(\frac{f_1}{f_2})^2}\sigma_{\emptyset_{sub-band}} \approx \frac{f_2}{f_0}\frac{f_1 f_2}{(f_2-f_1)(f_2+f_1)}\sqrt{2}\frac{\sqrt{N}}{\sqrt{2Pix_N}} \cdot \frac{\sqrt{1-\gamma_0^2}}{\gamma_0} \quad (2.10)$$

For current SAR systems, carrier frequencies f_0 are at the level of GHz and the chirp bandwidth is usually at tens of MHz (e.g., L-band ALOS-1 PALSAR, $f_0 = 1.27GHz$, $\mathrm{B}_0 = 14\,MHz\ or\ 28\,MHz$), therefore $f_0 \gg \mathrm{B}_0$ and the sub-band data center frequencies are close to each other $f_0 \cong f_2 \cong f_1$. Hence, for an N sub-band configuration, Eq. (2.10) can be approximated as:

$$\sigma_{\emptyset_{iono}} = \frac{f_0}{2(f_2-f_1)}\frac{\sqrt{N}}{\sqrt{Pix_N}} \cdot \frac{\sqrt{1-\gamma_0^2}}{\gamma_0} \quad (2.11)$$

Eq. (2.11) shows that the achievable accuracy of the ionospheric phase estimate $\sigma_{\emptyset_{iono}}$ improves as the separation between the two sub-bands center frequencies $(f_2 - f_1)$ is maximized. Therefore, the minimal standard deviation $\sigma_{\emptyset_{iono}}$ is achieved using the first (f_1) and last sub-band f_N. Following the definition of sub-band center frequencies in Eq. (2.4), the accuracy of the ionospheric phase estimate for an optimized configuration can be described as

$$\sigma_{\emptyset_{iono}} = \frac{1}{2\sqrt{Pix_N}}\frac{f_0}{B}\frac{\sqrt{1-\gamma_0^2}}{\gamma_0}\frac{\sqrt{N}}{(1-\frac{1}{N})} \quad (2.12)$$

Conventional studies focused on two-sub-band solutions to the ionospheric correction problem (Bamler and Eineder, 2005; Brcic et al., 2011, 2010; Gomba et al., 2016) showed that dividing the full range spectrum into three sub-bands (N=3), and utilizing the upper and lower sub-bands achieve the optimal ionosphere estimation. For N=3, the ionosphere estimation accuracy is:

$$\hat{\sigma}_{\emptyset_{iono}} = \frac{3\sqrt{3}}{4\sqrt{Pix_N}}\frac{f_0}{B}\frac{\sqrt{1-\gamma_0^2}}{\gamma_0} \quad (2.13)$$

2.4 Practical Implementation of the Split Spectrum Technique for InSAR Ionosphere Estimate

As $f_0 \gg B_0$ and as the sub-band center frequencies f_1 and f_2 are close to each other, we can simplify Eq. (2.7) to aid in its conceptual interpretation

$$\emptyset_{iono} \cong \left(\emptyset_1 - \emptyset_2 \frac{f_1}{f_2}\right) \frac{f_0}{2(f_2 - f_1)} \quad (2.14)$$

We can see from Eq. (2.14) that the information content of the ionospheric phase estimate stems from a small differential sub-band phase estimate $\left(\emptyset_1 - \emptyset_2 \frac{f_1}{f_2}\right)$, which is subsequently scaled up by a large multiplication constant $(\frac{f_0}{2(f_2 - f_1)})$. Therefore, any processing error or noise in $\left(\emptyset_1 - \emptyset_2 \frac{f_1}{f_2}\right)$ will result in large biases in the final ionosphere estimate, requiring careful processing when generating the sub-band interferograms $\emptyset_1$ and $\emptyset_2$. Gomba et al. (Gomba et al., 2016) discussed this issue by proposing data processing steps such as fine co-registration, multi-looking, sub-band center frequency estimation, and phase unwrapping error correction, to arrive a more robust ionospheric phase estimates $\emptyset_{iono}$.

Through applying split spectrum techniques to a large number of InSAR data from a variety of SAR sensors, we found a set of additional processing details that need to be considered to warrant robust and unbiased ionospheric phase correction. These additional factors include the consideration of baseline-dependent spectral shifts in the data processing flow as well as the use of a multiple sub-band solution for more robust and accurate ionospheric phase estimation especially for low coherence data. Both factors are introduced in the following sub-sections.

2.4.1 Split Spectrum InSAR Processing for Case with Large Perpendicular Baseline

For an area on ground surveyed by a SAR sensor from different incidence angles, the same ground spectrum will be projected into different SAR signal spectra. This phenomenon is called the wavenumber shift (or spectral shift) effect and it affects the width of the common spectrum that is observed by the two interferometric partner images.

Spectral shifts in SAR images originate from the difference between the ground spectrum of an observed surface and the SAR signal spectrum as shown in Figure 2.1. The ground spectrum is a function of the object properties (e.g., radar reflectivity of the surface) and is independent of the imaging characteristics. The SAR signal spectrum is the segment of the object spectrum that

is observed by an imaging system and is therefore dependent on its specifications, foremost its bandwidth, sampling frequency, and observation geometry.

In interferometry, two images observing the ground at different times and from slightly different across-track locations are combined to form an interferogram. Due to their difference in observation geometry, expressed by different look angles θ_1 and θ_2, a slightly different section of the object spectrum will be mapped into the respective observed signal spectra (see Figure 2.1).

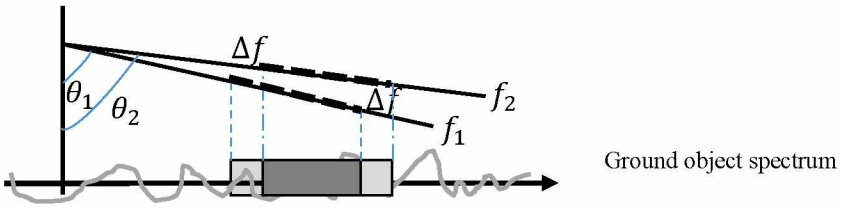

Figure 2.1 Spectral shift principle in the frequency domain. For SAR data acquired at different incidence angle θ_1, θ_2, the same spectrum signal in the acquired SAR data corresponding to two ground object spectrums which is shifted each other by Δf.

The size of the relative spectral shift between the observed object spectra depends on the look angle difference, expressed by the length of the effective perpendicular baseline $B_\perp$, the local surface slopes α, the wavelength of the system λ, and the range to the object on the ground R_0, and can be calculated from (Gatelli, et al 1994, Guilasso, 2006):

$$\Delta f = -\frac{cB_\perp}{\lambda R_0 \tan(\theta-\alpha)} \quad (2.15)$$

The shift between the observed object spectra causes the two images to have an overlapping spectral part, which contains information (illustrated as the light gray area in Figure 2.2), and two non-overlapping parts, which can be considered as noise in an interferogram (cf. Figure 2.2). Hence, if not appropriately accounted for, this spectral shift will lead to InSAR data decorrelation. In split spectrum InSAR processing, where the sub-band data has narrow bandwidth, the spectral shift effect becomes more prominent if not appropriately handled. This in the end will be reflected as sub-band interferogram coherence decrease and leads to the ionosphere estimation degradation.

In addition to potential coherence loss, the spectral shift Δf reduces the common bandwidth that is available for interferometric processing $B_{common} = B_0 - \Delta f$, reducing the amount of achievable spectral separation for split spectrum processing and, hence, limiting the accuracy with which the ionospheric phase contribution $\emptyset_{iono}$ can be estimated (see (Eq. 2.12)).

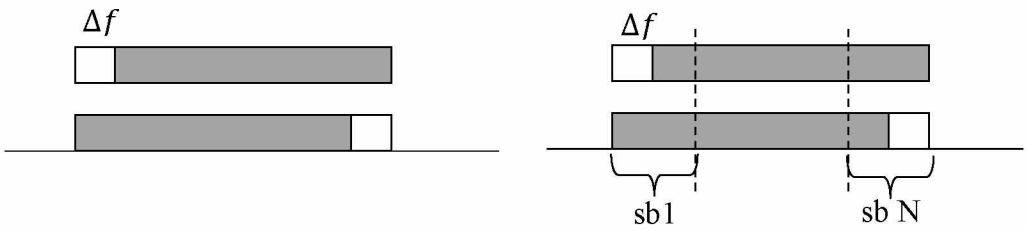

Figure 2.2 (Left) Spectrum shift effect in InSAR data. (Right) Master and slave data sub-band generation without including spectrum shift effect.

Both the decorrelation and bandwidth reduction effects need to be considered when designing a split spectrum processing concept and should be added to the split spectrum mathematical model.

In the traditional formulation of the split spectrum approach, the definition of the sub-band positions and bandwidth is based on the full range bandwidth B_0 of the used SAR imaging system, ignoring the impact of non-zero spatial baselines on the common bandwidth between master and slave image. To define the position and bandwidth of the split spectrum sub-bands, the traditional formulation divides bandwidth B_0 into N equal non-overlapping sub-bands, resulting in nominal sub-band bandwidths of $B_{sb} = \frac{B_0}{N}$. Due to the spectral shift Δf, the true common bandwidth of corresponding master and slave sub-bands is, however, lower than this number and is reduced to

$$B_{sb}^{com1} = \frac{B_0}{N} - \Delta f \qquad (2.16)$$

Figure 2.2 conceptually shows this effect. The ground spectrum observed by corresponding sub-bands are shifted by Δf from each other, reducing the common bandwidth captured by each sub-band pair. In this approach, each sub-band will have to be band-pass filtered to remove non-overlapping spectral components and avoid decorrelation. This reduces sub-band bandwidth, changes their center frequency, and, hence, modifies the split spectrum configuration. Also, note that due to the narrow bandwidths of the N sub-bands, B_{sb}^{com1} degrades quickly with baseline $B_\perp$, potentially leading to complete decorrelation and breakdown of the split spectrum concept even for rather moderate $B_\perp$.

To avoid these unintended consequences, we propose to incorporate the spectral shift information in the process of sub-band generation for split spectrum InSAR processing. In our approach, information about Δf is used in the definition of both the sub-band center-frequency positions and the sub-band bandwidths.

The modified equation for calculating sub-band center frequencies is as follows

$$f_m = f_0 - \frac{(\mathrm{B}_0 - \Delta f)}{2} + (m - \frac{1}{2})B_{sb}^{com2} = f_0 + (\mathrm{B}_0 - \Delta f)(\frac{1}{2} - \frac{m-\frac{1}{2}}{N}) \quad (2.17)$$

The variable B_{sb}^{com2} in Eq. (2.17) corresponds to the modified sub-band bandwidth which can be calculated from

$$B_{sb}^{com2} = \frac{B_0 - \Delta f}{N} \quad (2.18)$$

We can see that the values for B_{sb}^{com} are different between the conventional processing strategy (where common bandwidth is expressed in Eq. (2.16)) and in our proposed approach (where common bandwidth is expressed in Eq. (2.18)). In the traditional approach, sub-band spectral will no longer overlap once $N > \frac{B_0}{\Delta f}$. This will cause complete decorrelation of the sub-band interferograms, resulting in a breakdown of the split spectrum processing concept. However, this will not happen in our proposed strategy, unless the spectrum shift $\Delta f > B_0$ where sub-band will become fully decorrelated in both cases.

As a final note on the modified processing strategy, we want to highlight that the spectral shift Δf should be considered when extracting the sub-bands from the observed full-band SAR data. All sub-bands need to be extracted with a shift by Δf from each other (See Figure 2.3 for illustration).

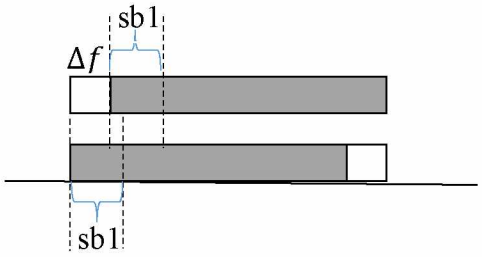

Figure 2.3 Master/slave sub-band generation including the spectrum shift effect.

2.4.2 Expanding toward A Multiple Sub-band Split Spectrum InSAR Concept

In the conventional approach, the full band data is divided into three equal non-overlapping sub-bands and only the upper and lower sub-bands are used for ionosphere estimation. This leads to the rejection of available information, resulting in sub-optimal performance. Furthermore, using only two sub-bands results in zero redundancy in the estimation model, making the split spectrum concept vulnerable to non-random processing errors (e.g., phase unwrapping errors) as well as spurious errors in the data, such as radio-frequency interference.

To alleviate these concerns, we propose a multiple sub-band approach for the ionosphere estimation, which utilizes all available spectral information in a redundant least-squares inversion and thus leads to a more accurate and robust ionosphere estimate.

2.4.3 Solving the Multiple Sub-bands Split Spectrum Problems

Dividing the full spectrum of the master/slave data into N sub-bands with a center frequency $f_1, f_2, f_3, \ldots, f_N$, and we can form N sub-band interferograms, which relate the original N sub-band InSAR phase observables $[\emptyset_1 \quad \ldots \quad \emptyset_N]^T$ to the desired ionospheric phase signals $\emptyset_{iono}$:

$$\begin{bmatrix} f_0/f_1 & f_1/f_0 \\ f_0/f_2 & f_2/f_0 \\ \cdots & \cdots \\ f_0/f_N & f_N/f_0 \end{bmatrix} \begin{bmatrix} \emptyset_{iono} \\ \emptyset_{non-disp} \end{bmatrix} = \begin{bmatrix} \emptyset_1 \\ \emptyset_2 \\ \cdots \\ \emptyset_N \end{bmatrix} \quad (2.19)$$

This redundant equation system can be solved using a general least-squares inverse model of the form

$$G \cdot m = d_{obs} \quad (2.20)$$

With

$$G = \begin{bmatrix} f_0/f_1 & f_1/f_0 \\ f_0/f_2 & f_2/f_0 \\ \cdots & \cdots \\ f_0/f_N & f_N/f_0 \end{bmatrix}, m = \begin{bmatrix} \emptyset_{iono} \\ \emptyset_{non-disp} \end{bmatrix}, d_{obs} = \begin{bmatrix} \emptyset_1 \\ \emptyset_2 \\ \cdots \\ \emptyset_N \end{bmatrix} \quad (2.21)$$

Since all sub-bands have non-overlapping equal bandwidth, it is reasonable to assume that all sub-bands are independent and have identical phase statistical property. A covariance matrix of all the sub-bands can be written as: $cov(d_{obs}) = \sigma_{subband} \cdot eye(N, N)$, where eye($N$,$N$) represents the identity matrix with dimension N by N, and $\sigma_{subband}$ is the sub-band interferometric phase standard deviation. The weighted least square estimate using its covariance matrix can be written as (Tarantola, 2005)

$$m = \begin{bmatrix} \emptyset_{iono} \\ \emptyset_{non-disp} \end{bmatrix} = (G^T G)^{-1} G^T d_{obs} \quad (2.22)$$

The ionosphere estimate will be the first element of parameter m. The parameter covariance matrix can be written as:

$$cov(m) = [\,(G^T G)^{-1} G^T\,] \cdot cov(d_{obs}) \cdot [\,(G^T G)^{-1} G^T\,]^T \quad (2.23)$$

and the accuracy of the ionosphere estimation $\sigma_{\emptyset_{iono}}$ will be the square root of the first element of the parameter covariance matrix $cov(m)$.

2.4.4 Accuracy Analysis

We evaluate the multiple sub-bands solution accuracy and compare it with conventional the conventional two sub-bands solution. In all the following simulations, we assume that we have an ALOS FBS InSAR pair as a base data set for ionospheric correction. The parameters assumed for this data set are as follows: Range bandwidth $B_0 = 28\,MHz$; InSAR data coherence: $\gamma = 0.6$; and the number of pixels averaged through the multi-looking process is 800. Based on these parameters, we calculated the theoretical estimation accuracy $\sigma_{\phi_{iono}}$ of the ionospheric phase screen for both the conventional approach (E.q. (2.12)) and our proposed multiple sub-band solution (E.q. (2.22)). Figure 2.4 shows $\sigma_{\phi_{iono}}$ for both the conventional and the modified approach as a function of the number of sub-bands that were created from the full-bandwidth data for split spectrum processing. Note that in the traditional concept, only two of the N sub-bands (namely the first and last sub band) are used for estimating $\sigma_{\phi_{iono}}$.

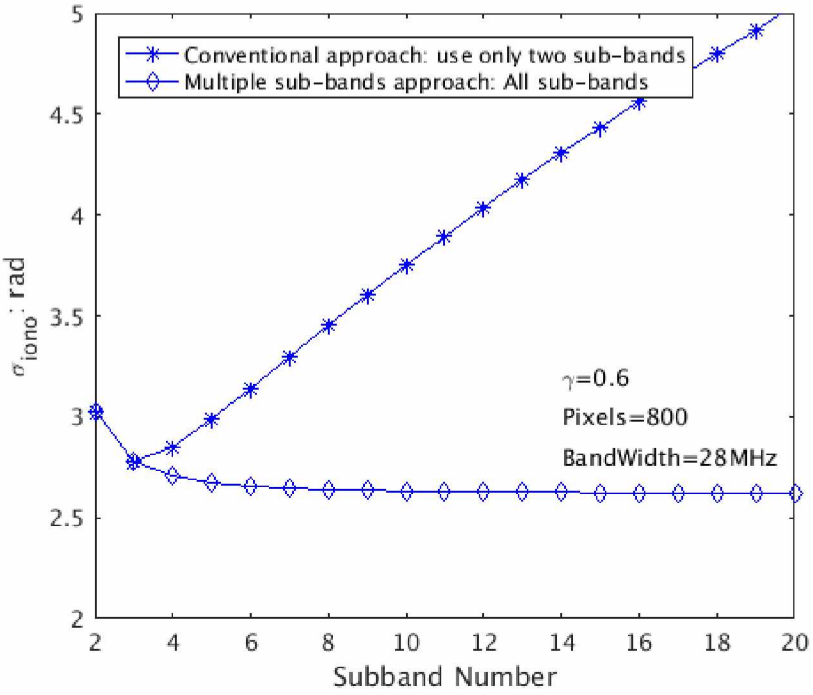

Figure 2.4 Different approaches derived ionosphere estimate accuracy. Stars line represent the conventional approach derived ionosphere accuracy under different sub-band configurations; diamond line represents the proposed multiple sub-band approach ionosphere accuracy under different sub-band configurations.

Figure 2.4 shows that in the traditional processing concept, the ionospheric phase estimate achieves the minimal standard deviation when the full band is divided into three sub-bands. This result agrees well with previous studies (Bamler and Eineder, 2005; Brcic et al., 2011, 2010;

Gomba et al., 2016). For the proposed multiple sub-bands approach, we see that the ionosphere estimate standard deviation decreases while sub-band number increases. More importantly the ionospheric estimate always achieves a better accuracy than the case with only two sub-bands derived ionospheric estimate (they are nearly identical for N=2, 3). This result is similar to the finding in a study using multiple sub-bands InSAR for Digital Elevation Model (DEM) retrieval (Bovenga et al., 2013). We note that when N approaches too large a number, the sub-band bandwidth will decrease to a quite small number, and sub-band data is highly possible to be dominant by noise. Therefore, in implementation of the multiple sub-bands approach, there should be a trade-off of the sub-band number and sub-band quality.

We also analyzed the dependence of the ionosphere estimation accuracy on the total bandwidth B_0 that is available for split spectrum processing. We calculate the ionosphere standard deviation for both the conventional and the proposed multiple sub-band solutions for different bandwidth settings (namely an ALOS PALSAR FBS ($B_0 = 28\,MHz$) and an ALOS-2 PALSAR $B_0 = 42\,MHz$ configuration). The results of this analysis are shown in Figure 2.5.

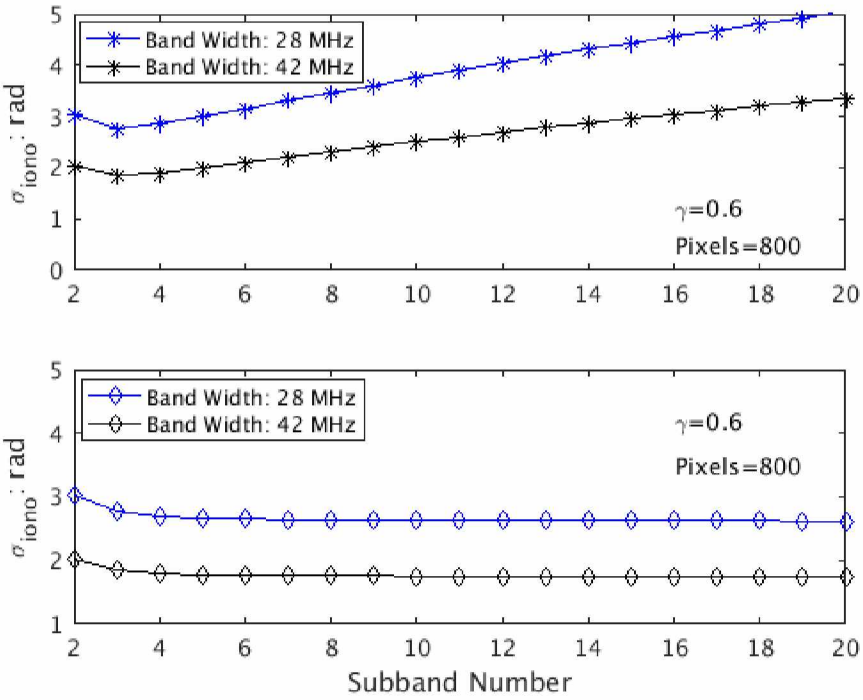

Figure 2.5 Accuracy of ionospheric phase estimates derived from data with different bandwidths. Upper panel: Conventional approach; lower panel: Proposed multiple sub-band approach.

It can be seen from Figure 2.5. that larger bandwidth tends to increase the accuracy of the ionospheric phase estimate for the same sub-band configuration. This is in good correspondence

of the prevailing understanding of the split spectrum estimation process. For the proposed multi-sub-band approach, large bandwidths and large numbers of sub-bands result in higher accuracy of $\widehat{\emptyset}_{iono}$.

2.4.5 Benefits on the Robustness against Gross Errors in the InSAR Observations

In contrast to the conventional approach where only two sub-bands are used, the multiple sub-bands approach introduces redundancy into the estimation process, which can be used to improve algorithmic robustness with respect to gross errors in the InSAR observations. Such gross errors can be related to spurious phase unwrapping errors or to frequency contaminations such as radio frequency interference that may affect certain sub-bands more than others. The redundancy in the equation system can be used to identify outliers and iteratively remove them from the inversion model to achieve higher robustness.

For any two sub-bands *m*, *n*, their differential sub-band phase is:

$$\emptyset_m - \emptyset_n = \left(\frac{f_0}{f_m} - \frac{f_0}{f_n}\right)\emptyset_{iono} + \left(\frac{f_m}{f_0} - \frac{f_n}{f_0}\right)\emptyset_{non-disp} \quad (2.24)$$

Based on Eq. (2.4) and because $f_0 \cong f_m \cong f_n$, it follows that $\emptyset_m - \emptyset_n = \frac{f_n - f_m}{f_0}\left(\emptyset_{iono}\frac{f_0^2}{f_m f_n} - \emptyset_{non-disp}\right) \cong -\frac{f_m - f_n}{f_0}\left(\emptyset_{iono} - \emptyset_{non-disp}\right) = \frac{(m-n)B_w}{Nf_0}\left(\emptyset_{iono} - \emptyset_{non-disp}\right)$. We can rewrite Eq. (2.24) as:

$$\frac{\emptyset_m - \emptyset_n}{(m-n)} \cong \frac{B_w}{Nf_0}\left(\emptyset_{iono} - \emptyset_{non-disp}\right) \quad (2.25)$$

For a specific data set, the $\emptyset_{iono}$, $\emptyset_{non-disp}$ are the ionosphere component and nondispersive component corresponding to the radar carrier frequency f_0, and these two are therefore the same for all sub-bands. $\frac{B_w}{Nf_0}$ is also a constant when N is fixed; therefore $\frac{\emptyset_m - \emptyset_n}{(m-n)}$ is always a constant in theory. For N sub-bands, we can get a combination of C_N^2 differential phases (e.g diff_ph1, diff_ph2, …, diff_ph(C_N^2)) through equation (2.25) which all have identical statistical properties. Therefore, we can calculate a pixel-based phase quality through calculating the standard deviation of these C_N^2 differential phase values.

$$Pixel_{quality} = std([diff_{ph1}, diff_{ph2}, \dots, diff\_ph\{C_N^2\}]) \quad (2.26)$$

Pixels whose sub-band differential phase standard deviation $Pixel_{quality}$ is larger than a threshold (e.g, the average phase standard deviation) will be identified as outliers.

For the outlier pixels, the ionosphere estimate will not be used; instead its estimate will be replaced by the median of its surrounding valid pixels. By implementing this outlier removal processing, the multiple sub-bands solution will be more robust.

2.4.6 Practical Implementation of Split Spectrum Technique for InSAR Ionosphere Estimate

The implementation of our ionospheric correction approach, including the proposed accommodation of spectral-shift effects as well as the proposed multi sub-band solution can be broken down into the following steps:

(1) Sub-band generation.

For this processing, a bandpass filter is used to generate the sub-band data. To account for baseline-dependent spectral shifts, the corresponding sub-bands in the master and slave images are selected to have coinciding ground spectral. For the multiple sub-band configuration, we found data sub-band data quality usually does not decrease much if sub-band bandwidth stays above 3 MHz. As the SAR signal is a modulated signal, we then need to demodulate it to make sure its center frequency is correct for the generated sub-band.

(2) Fine registration.

In addition to conventional InSAR processing, which uses polynomial approximations to co-register image pairs, split spectrum processing requires an additional fine-registration process to estimate and remove small scale offsets caused by local gradients in the ionospheric total electron content. Detailed process refers to our other paper in Chapter 3 (Liao et al., 2018).

(3) Sub-band interferogram generation and phase unwrapping.

We use the polynomial fitted offset plus the additional fine-registration extracted fine localized offset maps for the sub-band slave data co-registration and resampling. Multiple sub-band interferograms are generated and each interferogram is unwrapped using a minimum-cost-flow phase unwrapper (Werner et al., 2000).

(4) Ionosphere estimate and post-processing

We estimate the raw ionosphere using all generated sub-band interferograms. We followed the phase unwrapping error correction strategy proposed in (Gomba et al., 2016) and correct the phase unwrapping error for each sub-band. Following that, outliers are detected based on the theory proposed in 2.4.5. Raw ionosphere phase screens with the pixels identified as outliers will

be removed and its value will be replaced by its surrounding valid pixels median value. We then implemented a 2D gaussian filter for the ionosphere filtering to suppress noise effects.

The detailed processing flow is shown in Figure 2.6.

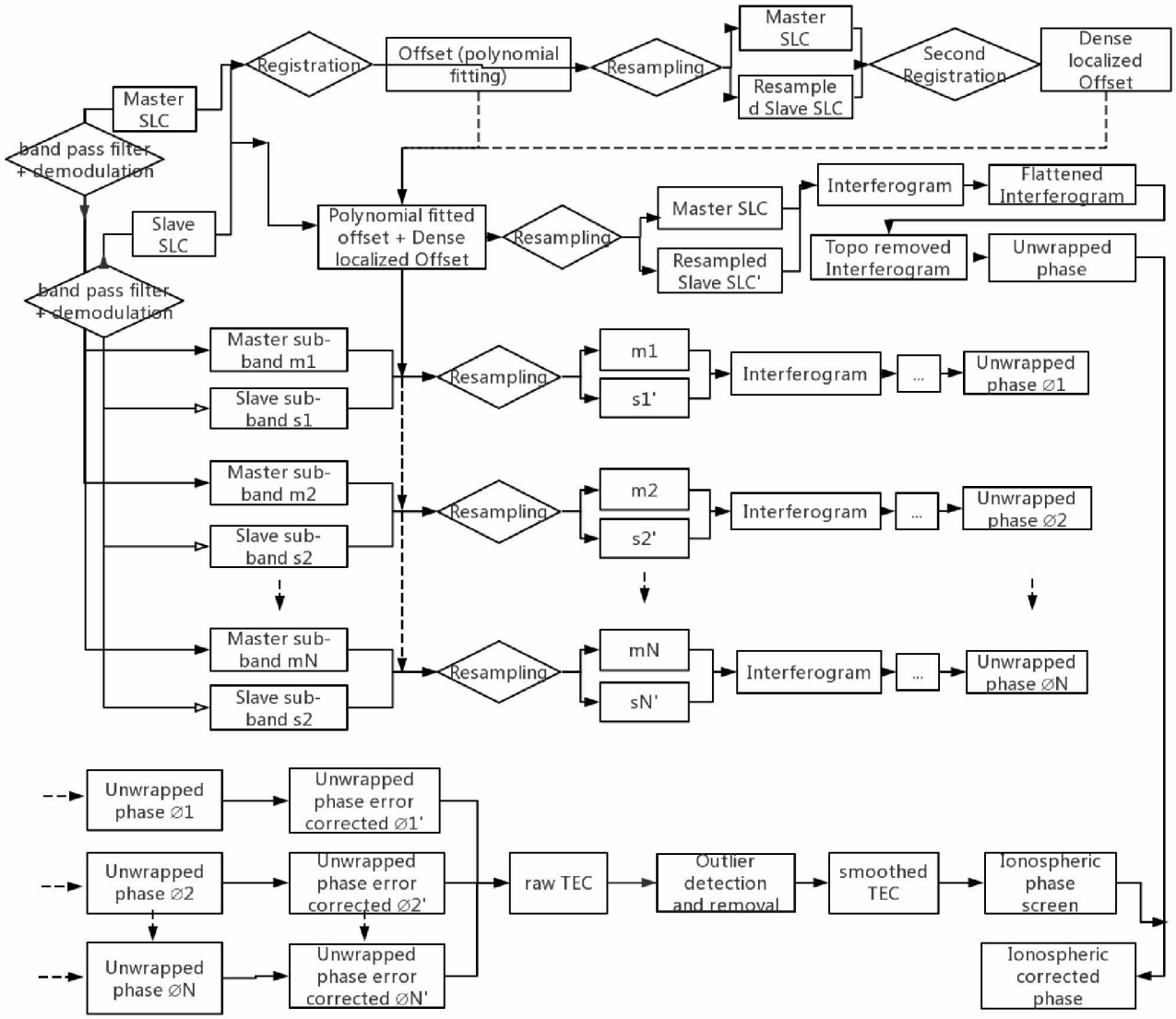

Figure 2.6 Proposed practical split spectrum approach for InSAR Ionospheric correction workflow.

2.5 Case Study Analysis to Assess Split Spectrum Performance

2.5.1 Study Site and Used Datasets

To validate our proposed processing strategy and evaluate its performance, we select an ALOS PALSAR InSAR data set acquired over the North Slope of Alaska. The geographical location of the dataset is shown in Figure 2.7. Two consecutive image frames were concatenated

to provide sufficiently large spatial coverage to evaluate the ionospheric correction performance across a broad range of spatial scales.

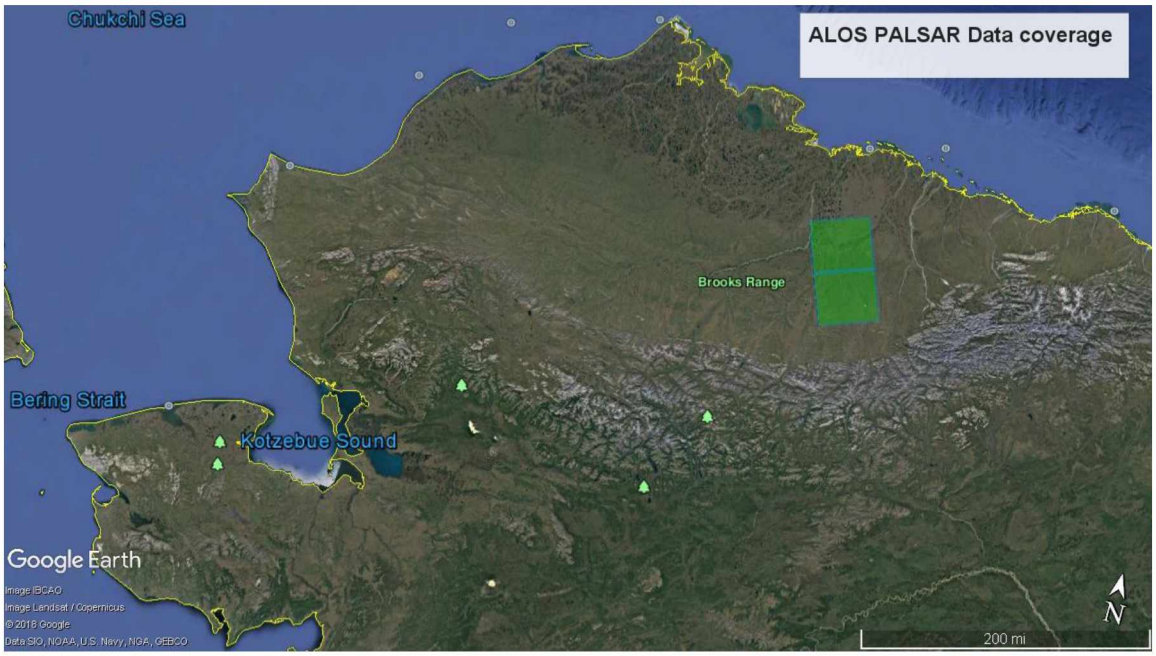

Figure 2.7 Coverage of dataset used in this study.

More detailed information about this InSAR data set can be found in Table 2.1

Table 2.1 Data Information.

Data	Acquisition date	Perpendicular baseline (m)	Bandwidth (MHz)	Sampling Frequency (MHz)
ALPSRP126361380 **ALPSRP126361390**	2008/06/08	-5137	28 MHz	32 MHz
ALPSRP186751380 **ALPSRP186751390**	2009/07/27		28 MHz	32 MHz

The data set used for validation includes the footprint of the Anaktuvuk River fire, the largest tundra fire in recent history (Qiu, 2009). The fire lasted from early July until early Oct 2007 and caused significant changes in the local permafrost environment (L. Liu et al., 2014). Due to the fire event, the upper organic layer of the permafrost was removed, and the scattering property of this area changed dramatically. Several studies using both InSAR and lidar indicate an increased post-fire subsidence rate of the burnt area related to increased summer melting, usually at several cm/season (Iwahana et al., 2016; Jones et al., 2015; L. Liu et al., 2014).

The images used for interferogram formation were both acquired after the tundra fire and therefore are suitable for post-fire deformation monitoring. The two SAR data have a large spatial

baseline of more than 5000m. The large baseline leads to a significant spectral shift of $\Delta f = 9.3$ MHz between the ground spectra observed by the master and slave datasets. Therefore, considering spectral shifts in the split spectrum processing flow is mandatory to warrant sufficient data coherence as well as predictable sub-band configurations. Due to the fire effect, the organic layer removal and the vegetation retrieval after the fire, the fire scar area experienced a lot of surface change, leading to lower coherence within the burnt area. The coherence image used in this study is shown in Figure 2.9 left panel.

As can be seen in Figure 2.8 of the azimuth offset map measured between the master and slave image, this L-band interferogram shows significant ionospheric impacts on this dataset. The offset map shows so called azimuth streaks (Gray et al., 2000) that are typically associated with the presence of ionospheric phase distortions in the data. We can see that ionosphere-induced pixel offsets reach values as large as two pixels for this dataset. The associated ionosphere phase screen is superimposed on the deformation signal in the fire scar area, potentially leading to biases in permafrost information derived from InSAR. Therefore, ionosphere correction becomes a necessity for this data set.

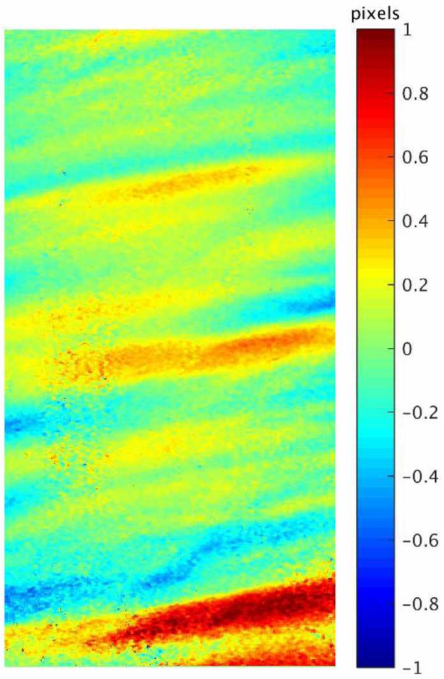

Figure 2.8 Ionosphere induced Azimuth offset. Data set: 20080608/20090727. The unit is Pixel, the pixel spacing is 3.13 m.

2.5.2 Experiment With and Without including the Spectral Shift Effect

We follow the procedure in Section 2.4.6 to implement our data processing flow. First, we generate the sub-band data without considering the spectral shift effect. We split the spectrum into three sub-bands to be consistent with the conventional split spectrum setup, resulting in three sub-bands with a nominal sub-band bandwidth of $B_{sb} = \frac{B_w}{3} = 9.33\ MHz$. However, the spectrum in the data is shifted by about 9.3 MHz, so the common bandwidth becomes $B_{sb} = \frac{B_w}{3} - |\Delta f| = 0.03\ MHz$ resulting in complete decorrelation if Δf is not considered in the split spectrum design (Figure 2.9, right panel).

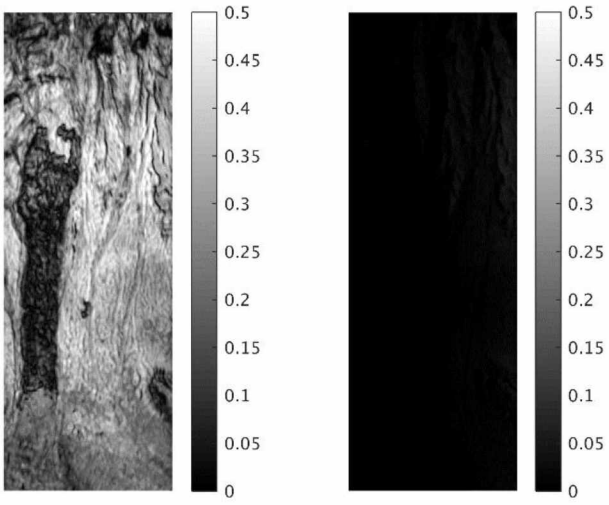

Figure 2.9 Sub-band coherences histogram comparison for the cases with (Left) and without (Right) considering spectrum shift effect.

When the spectral shift is included for sub-band generation, sub-band center frequencies are automatically designed to compensate for Δf and the common bandwidth for sub-band data in a three sub-band configuration is: $B'_{sb} = \frac{B_w - |\Delta f|}{3} = 6.3\ MHz$. The interferogram after topographic phase removal is shown in the first panel of Figure 2.10, and its coherence map is shown in the left panel of Figure 2.9. We can see significant improvement in the interferometric phase quality and coherence compared to the case without inclusion of spectral shift effects. Under this three sub-bands configuration and utilizing only the lower and upper sub-bands, we get the ionospheric estimate shown in the center panel in Figure 2.10.

2.5.3 Multiple Sub-bands Approach for Ionospheric Phase Estimation

We also tested our proposed multi sub-bands approach for its ionospheric phase estimation performance. Based on the theory, the more sub-bands are used in the analysis, the better the accuracy of the derived product. However, we noticed that when the number of sub-bands increases, the performance improvement gained from adding additional sub-bands diminishes. Furthermore, increasing the number of sub-bands also increases processing cost. We found that 6-8 sub-bands provide a good compromise between estimation accuracy and computational load.

In this study, we split the full spectrum into six sub-bands, and every sub-band has a bandwidth of about 3.2 MHz. We implement the multi sub-band processing as described in Section 2.2.4, leading to the results shown in the right panel of Figure 2.10. As we can see, the multi sub-band approach reduces noise in particular in the low coherence area of the burn scar.

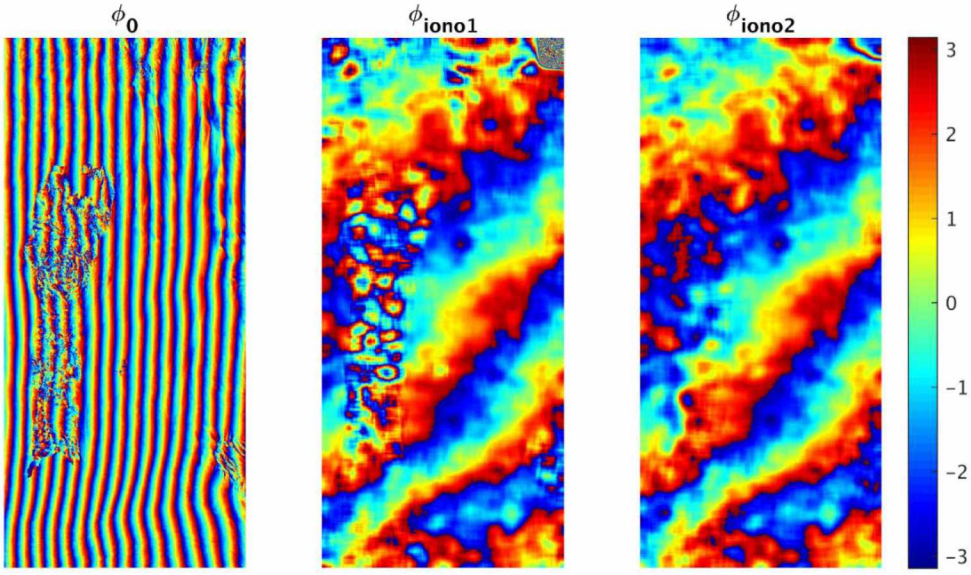

Figure 2.10 Original interferogram and ionospheric estimates. Left panel shows the topographic phase removed interferogram, the central panel is the ionosphere estimate in the case where spectrum shift effect is included in sub-bang generation and the full band is divided into three sub-bands. Right panel is the ionosphere estimate using the proposed multiple sub-bands approach.

2.5.4 Results Analysis

To evaluate the performance of the ionospheric phase correction, we subtract our ionospheric estimates from the original topographic phase removed interferogram. The results are shown in Figure 2.11. The first panel of Figure 2.11 shows the topographic phase removed interferogram, which will be named the original interferogram. The second panel shows the result

if we don't implement ionosphere correction and just implement orbit correction as conventional approaches often do. We can see that at the bottom part of the image, uncompensated ionospheric signals lead to significant phase biases. Similar distortions are also visible across the rest of this scene. The third panel of Figure 2.11 shows the residual phase screen after ionospheric correction via the conventional processing approach was applied. While the main ionospheric phase structures were removed, a range of localized phase artifacts are visible that are related to noise in the ionospheric phase estimate. Particularly notable are significant phase distortions in the low-coherence areas such as within the burn scar. These distortions are largely removed after the multi sub-band processing approach was applied (fourth panel in Figure 2.11).

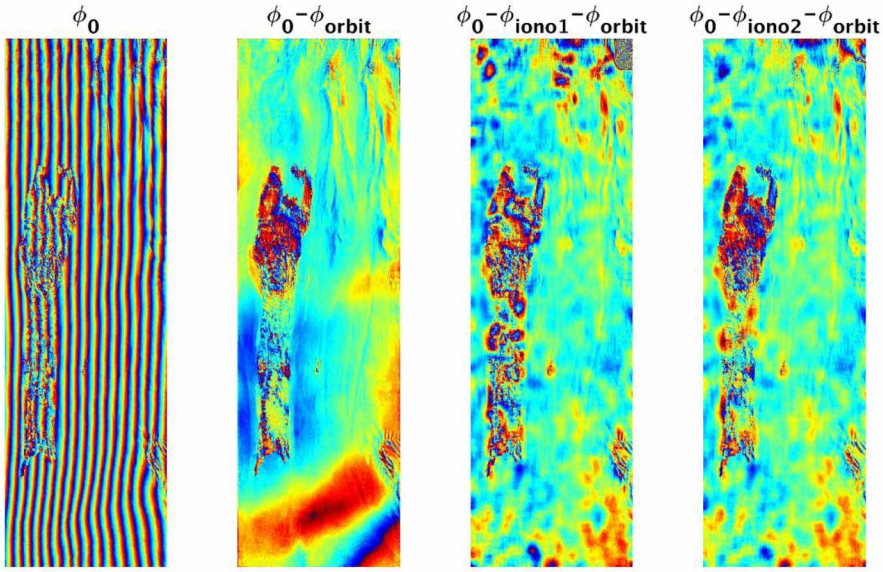

Figure 2.11 Original interferogram and its ionosphere correction results. First panel: Original topographic removed interferogram. Second panel: Original interferogram with only orbit correction result. Third panel: Original interferogram with ionosphere from three sub-band configuration correction. Fourth panel: Original interferogram with multiple sub-bands derived ionosphere correction.

In addition to the visual inspection, we also quantitatively evaluated the performance of the ionospheric phase correction approach. We divide the estimated ionospheric phase screen into small patches and estimate the phase noise (standard deviation) of each patch. For each patch, we calculated its corresponding median coherence value. Each patch is plotted as a dot and is shown in Figure 2.12. For all the patches, we classified them into different coherence range (e.g 0~0.1, 0.1~0.2, …, 0.9~1), and we calculate the median phase standard deviation of all the patches in each coherence range. This result is plotted as the median fitted Iono STD in Figure 2.12.

We can see that the proposed multiple sub-bands ionosphere estimate shows a lower standard deviation comparing to that of the three sub-band configuration derived result. This also demonstrates the superiority of the proposed method.

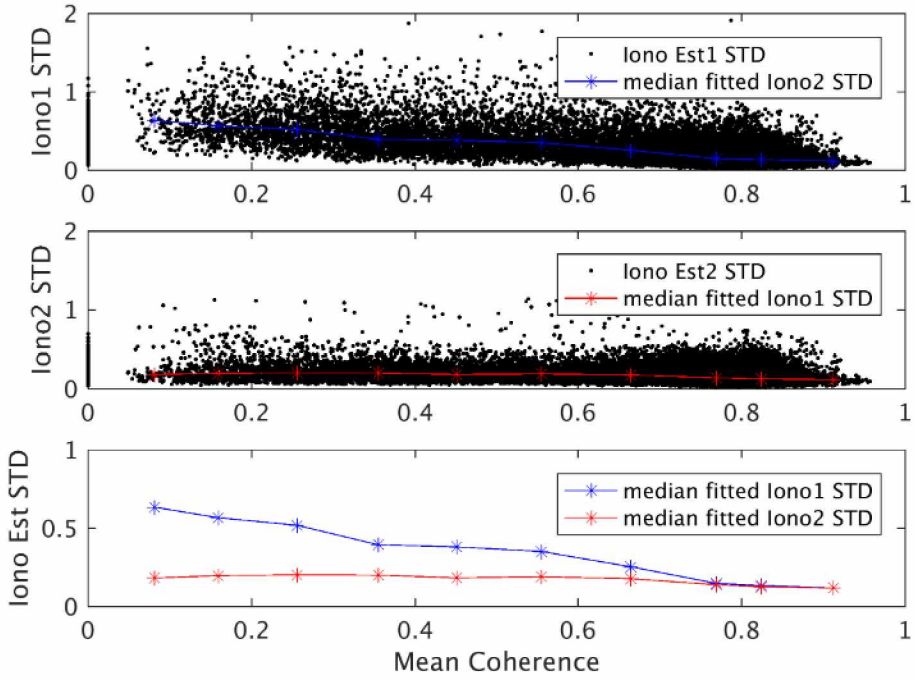

Figure 2.12 Ionosphere estimate quality analysis. Upper panel: each black point shows the ionosphere estimate Iono1 standard deviation VS coherence of each patch. The blue line is its median fitted result. Middle panel: each black point shows the ionosphere estimate Iono2 standard deviation VS coherence of each patch. The red line is its median fitted result. Lower panel: The fitted result comparison.

2.6 Summary and Conclusion

In this paper, we proposed an extension of the conventionally used split spectrum InSAR model to warrant more robust correction ionospheric phase correction results with improved accuracy. In particular, we formally included spectral shift effects caused by non-zero spatial baselines into the mathematical model. This effect can be significant for SAR mission with possible large baseline, such as the L-band ALOS PALSAR. Using a case study with a 28 MHz ALOS PALSAR data set showed improved ionosphere estimation performance once compensation for spectral shifts was incorporated in the split spectrum processing flow.

We also expanded the ionospheric phase estimation concept from a non-redundant two-sub-band solution to a redundant multi sub-band approach to improve estimation accuracy and robustness. We quantitatively analyzed the proposed technique and compared its ionosphere

estimation performance with the approach used in previous studies. We analyzed the bandwidth effect on the ionosphere estimate accuracy. We proposed a new pixel-based outlier detection approach in the framework of the multiple sub-bands solution, which is helpful for improving the robustness of the proposed multiple sub-bands approach. Our case study shows that the ionospheric phase estimate shows reduced noise compared to traditional split spectrum processing. Using this multiple sub-bands estimate, the ionosphere corrected result also shows a better estimate of the fire scar.

Our study will be significant for processing data with large geometric baselines, and the proposed multiple sub-band solution will be very helpful for improving the split spectrum ionosphere estimation accuracy and robustness.

2.7 Acknowledgement

We thank The Japan Aerospace Exploration Agency (JAXA) and The Alaska Satellite Facility (ASF) for providing the ALOS-1 PALSAR SAR data.

2.8 Reference

Bamler, R., Eineder, M., 2005. Accuracy of Differential Shift Estimation by Correlation and Split-Bandwidth Interferometry for Wideband and Delta-k SAR Systems. IEEE Geoscience and Remote Sensing Letters 2, 151–155. https://doi.org/10.1109/LGRS.2004.843203

Bovenga, F., Giacovazzo, V.M., Refice, A., Veneziani, N., 2013. Multichromatic Analysis of InSAR Data. IEEE Transactions on Geoscience and Remote Sensing 51, 4790–4799. https://doi.org/10.1109/TGRS.2012.2230633

Brcic, R., Parizzi, A., Eineder, M., Bamler, R., Meyer, F., 2011. Ionospheric effects in SAR interferometry: An analysis and comparison of methods for their estimation, in: Geoscience and Remote Sensing Symposium (IGARSS), 2011 IEEE International. IEEE, pp. 1497–1500.

Brcic, R., Parizzi, A., Eineder, M., Bamler, R., Meyer, F., 2010. Estimation and compensation of ionospheric delay for SAR interferometry, in: Geoscience and Remote Sensing Symposium (IGARSS), 2010 IEEE International. IEEE, pp. 2908–2911.

Bürgmann, R., Rosen, P.A., Fielding, E.J., 2000. Synthetic aperture radar interferometry to measure Earth's surface topography and its deformation. Annual review of earth and planetary sciences 28, 169–209.

Chen, A.C., Zebker, H.A., 2014. Reducing Ionospheric Effects in InSAR Data Using Accurate Coregistration. IEEE Transactions on Geoscience and Remote Sensing 52, 60–70. https://doi.org/10.1109/TGRS.2012.2236098

Fattahi, H., Simons, M., Agram, P., 2017. InSAR Time-Series Estimation of the Ionospheric Phase Delay: An Extension of the Split Range-Spectrum Technique. IEEE Transactions on Geoscience and Remote Sensing 55, 5984–5996. https://doi.org/10.1109/TGRS.2017.2718566

Freeman, A., 2004. Calibration of linearly polarized polarimetric SAR data subject to Faraday rotation. IEEE Transactions on Geoscience and Remote Sensing 42, 1617–1624. https://doi.org/10.1109/TGRS.2004.830161

Freeman, A., Saatchi, S.S., 2004. On the detection of Faraday rotation in linearly polarized L-band SAR backscatter signatures. IEEE Transactions on Geoscience and Remote Sensing 42, 1607–1616. https://doi.org/10.1109/TGRS.2004.830163

Gomba, G., De Zan, F., 2015. Estimation of ionospheric height variations during an aurora event using multiple semi-focusing levels, in: 2015 IEEE International Geoscience and Remote Sensing Symposium (IGARSS). IEEE, pp. 4065–4068.

Gomba, G., Parizzi, A., De Zan, F., Eineder, M., Bamler, R., 2016. Toward operational compensation of ionospheric effects in SAR interferograms: the split-spectrum method. IEEE Transactions on Geoscience and Remote Sensing 54, 1446–1461.

Gomba, G., Rodriguez Gonzalez, F., De Zan, F., 2017. Ionospheric Phase Screen Compensation for the Sentinel-1 TOPS and ALOS-2 ScanSAR Modes. IEEE Transactions on Geoscience and Remote Sensing 55, 223–235. https://doi.org/10.1109/TGRS.2016.2604461

Gray, A.L., Mattar, K.E., Sofko, G., 2000. Influence of ionospheric electron density fluctuations on satellite radar interferometry. Geophysical Research Letters 27, 1451–1454.

Hashimoto, M., Enomoto, M., Fukushima, Y., 2010. Coseismic Deformation from the 2008 Wenchuan, China, Earthquake Derived from ALOS/PALSAR Images. Tectonophysics 491, 59–71. https://doi.org/10.1016/j.tecto.2009.08.034

Hu, J., Li, Z., Zhang, L., Ding, X., Zhu, J., Sun, Q., Ding, W., 2012. Correcting ionospheric effects and monitoring two-dimensional displacement fields with multiple-aperture InSAR technology with application to the Yushu earthquake. Science China Earth Sciences 55, 1961–1971. https://doi.org/10.1007/s11430-012-4509-x

Iwahana, G., Uchida, M., Liu, L., Gong, W., Meyer, F.J., Guritz, R., Yamanokuchi, T., Hinzman, L., 2016. InSAR Detection and Field Evidence for Thermokarst after a Tundra Wildfire, Using ALOS-PALSAR. Remote Sensing 8, 218.

Jones, B.M., Grosse, G., Arp, C.D., Miller, E., Liu, L., Hayes, D.J., Larsen, C.F., 2015. Recent Arctic tundra fire initiates widespread thermokarst development. Scientific Reports 5. https://doi.org/10.1038/srep15865

Joughin, I., 2002. Ice-sheet velocity mapping: a combined interferometric and speckle-tracking approach. Annals of Glaciology 34, 195–201.

Joughin, I., Smith, B.E., Howat, I.M., Scambos, T., Moon, T., 2010. Greenland flow variability from ice-sheet-wide velocity mapping. Journal of Glaciology 56, 415–430.

Jung, H.-S., Lee, D.-T., Lu, Z., Won, J.-S., 2013. Ionospheric Correction of SAR Interferograms by Multiple-Aperture Interferometry. IEEE Transactions on Geoscience and Remote Sensing 51, 3191–3199. https://doi.org/10.1109/TGRS.2012.2218660

Jung, H.-S., Lee, W.-J., 2015. An Improvement of Ionospheric Phase Correction by Multiple-Aperture Interferometry. IEEE Transactions on Geoscience and Remote Sensing 53, 4952–4960. https://doi.org/10.1109/TGRS.2015.2413948

Kim, J.S., Papathanassiou, K.P., Scheiber, R. and Quegan, S., 2015. Correcting distortion of polarimetric SAR data induced by ionospheric scintillation. IEEE Transactions on Geoscience and Remote Sensing, 53(12), pp.6319-6335.

Kim, J., 2014. Development of ionosphere estimation techniques for the correction of SAR data.

Kim, J.S., Papathanassiou, K., 2015. On the separation of Dynamic Scattering and Ionospheric Effects in SAR data.

Kim, J.S., Papathanassiou, K.P., 2010. Faraday rotation estimation performance analysis. EUSAR 2010.

Liao, H., Meyer, F.J., 2016. Ionospheric Correction of InSAR for Accurate Ice Motion Mapping at High Latitudes, in: AGU Fall Meeting Abstracts.

Liao, H., Meyer, F.J., Liu, L., 2017. Ionospheric Correction in Using ALOS PALSAR InSAR Data for Monitoring Permafrost Subsidence associated with an Arctic Tundra Fire, in: AGU Fall Meeting Abstracts.

Liao, H., Meyer, F.J., Scheuchl, B., Mouginot, J., Joughin, I., Rignot, E., 2018. Ionospheric correction of InSAR data for accurate ice velocity measurement at polar regions. Remote Sensing of Environment 209, 166–180. https://doi.org/10.1016/j.rse.2018.02.048

Liu, L., Jafarov, E.E., Schaefer, K.M., Jones, B.M., Zebker, H.A., Williams, C.A., Rogan, J., Zhang, T., 2014. InSAR detects increase in surface subsidence caused by an Arctic tundra fire. Geophysical Research Letters 41, 3906–3913. https://doi.org/10.1002/2014GL060533

Liu, L., Zhang, T., Wahr, J., 2010. InSAR measurements of surface deformation over permafrost on the North Slope of Alaska. Journal of Geophysical Research 115. https://doi.org/10.1029/2009JF001547

Liu, Z., Jung, H.-S., Lu, Z., 2014. Joint Correction of Ionosphere Noise and Orbital Error in L-Band SAR Interferometry of Interseismic Deformation in Southern California. IEEE Transactions on Geoscience and Remote Sensing 52, 3421–3427. https://doi.org/10.1109/TGRS.2013.2272791

Massonnet, D., Feigl, K.L., 1998. Radar interferometry and its application to changes in the Earth's surface. Reviews of Geophysics 36, 441–500. https://doi.org/10.1029/97RG03139

Meyer, F., Bamler, R., Jakowski, N., Fritz, T., 2006. The Potential of Low-Frequency SAR Systems for Mapping Ionospheric TEC Distributions. IEEE Geoscience and Remote Sensing Letters 3, 560–564. https://doi.org/10.1109/LGRS.2006.882148

Meyer, F.J., 2011. Performance Requirements for Ionospheric Correction of Low-Frequency SAR Data. IEEE Transactions on Geoscience and Remote Sensing 49, 3694–3702. https://doi.org/10.1109/TGRS.2011.2146786

Meyer, F.J., Nicoll, J., 2008. The impact of the ionosphere on interferometric SAR processing, in: Geoscience and Remote Sensing Symposium, 2008. IGARSS 2008. IEEE International. IEEE, pp. II–391.

Meyer, F.J., Nicoll, J.B., Doulgeris, A.P., 2013. Correction and Characterization of Radio Frequency Interference Signatures in L-Band Synthetic Aperture Radar Data. IEEE Transactions on Geoscience and Remote Sensing 51, 4961–4972. https://doi.org/10.1109/TGRS.2013.2252469

Natsuaki, R., Nagai, H., Motohka, T., Ohki, M., Watanabe, M., Thapa, R.B., Tadono, T., Shimada, M., Suzuki, S., 2016. SAR interferometry using ALOS-2 PALSAR-2 data for the Mw 7.8 Gorkha, Nepal earthquake. Earth, Planets and Space 68. https://doi.org/10.1186/s40623-016-0394-4

Pi, X., Freeman, A., Chapman, B., Rosen, P., Li, Z., 2011. Imaging ionospheric inhomogeneities using spaceborne synthetic aperture radar. Journal of Geophysical Research 116. https://doi.org/10.1029/2010JA016267

Prats-Iraola, P., Rodriguez-Cassola, M., Yague-Martinez, N., Lopez-Dekker, P., Scheiber, R., De Zan, F., Kraus, T., Wollstadt, S., 2015. Repeat-pass interferometric experiments with the Tandem-X constellation for accurate along-track motion estimation. IEEE, pp. 4077–4080. https://doi.org/10.1109/IGARSS.2015.7326721

Qiu, J., 2009. Arctic ecology: Tundra's burning. Nature 461, 34–36. https://doi.org/10.1038/461034a

Raucoules, D., de Michele, M., 2010. Assessing Ionospheric Influence on L-Band SAR Data: Implications on Coseismic Displacement Measurements of the 2008 Sichuan Earthquake. IEEE Geoscience and Remote Sensing Letters 7, 286–290. https://doi.org/10.1109/LGRS.2009.2033317

Rignot, E., Mouginot, J., Scheuchl, B., 2011. Ice flow of the Antarctic ice sheet. Science 333, 1427–1430.

Rogers, N.C., Shaun Quegan, 2014. The Accuracy of Faraday Rotation Estimation in Satellite Synthetic Aperture Radar Images. IEEE Transactions on Geoscience and Remote Sensing 52, 4799–4807. https://doi.org/10.1109/TGRS.2013.2284635

Rosen, P.A., Hensley, S., Chen, C., 2010. Measurement and mitigation of the ionosphere in L-band interferometric SAR data, in: Radar Conference, 2010 IEEE. IEEE, pp. 1459–1463.

Rykhus, R.P., Lu, Z., 2008. InSAR detects possible thaw settlement in the Alaskan Arctic Coastal Plain. Canadian Journal of Remote Sensing 34, 100–112.

Tarantola, A., 2005. Inverse problem theory and methods for model parameter estimation.

Tong, X., Sandwell, D., n.d. Experiment of Ionospheric Corrections to ALOS L-Band Interferograms [WWW Document]. URL ftp://topex.ucsd.edu/pub/tong/ionosphere/ionosphere_ppt.pdf (accessed 11.18.16).

Tong, X., Sandwell, D., Luttrell, K., Brooks, B., Bevis, M., Shimada, M., Foster, J., Smalley, R., Parra, H., Báez Soto, J.C., Blanco, M., Kendrick, E., Genrich, J., Caccamise, D.J., 2010. The 2010 Maule, Chile earthquake: Downdip rupture limit revealed by space geodesy: DOWNDIP RUPTURE MAULE, CHILE EARTHQUAKE. Geophysical Research Letters 37, n/a-n/a. https://doi.org/10.1029/2010GL045805

Werner, C., Wegmüller, U., Strozzi, T., Wiesmann, A., 2000. Gamma SAR and interferometric processing software, in: Proc. ERS-ENVISAT Symposium, Gothenburg, Sweden, 16–20 October 2000.

Xu, Z.-W., Wu, J., Wu, Z.-S., 2004. A survey of ionospheric effects on space-based radar. Waves in Random Media 14, S189–S274.

Yague-Martinez, N., Prats-Iraola, P., Kraus, T., Wollstadt, S., Scheiber, R., 2016. Experimental validation with TerraSAR-X/TanDEM-X of advanced interferometric modes for accurate retrieval of azimuthal displacements. IEEE, pp. 1444–1447. https://doi.org/10.1109/IGARSS.2016.7729369

Zhang, B., Ding, X., Zhu, W., Wang, C., Zhang, L., Liu, Z., 2016. Mitigating Ionospheric Artifacts in Coseismic Interferogram Based on Offset Field Derived From ALOS-PALSAR Data. IEEE Journal of Selected Topics in Applied Earth Observations and Remote Sensing 9, 3050–3059.

Chapter 3

Ionospheric Correction of InSAR Data for Accurate Ice Velocity Measurement at Polar Regions[2]

3.1 Abstract

Interferometric synthetic aperture radar (InSAR) has become an essential tool for measuring ice sheet velocity in the Polar Regions. At low radar frequencies, e.g. L-band (1.2 GHz) but also at higher frequency, e.g. C-band (5.6 GHz), the ionosphere has been documented to be an important source of noise in these data. In this paper, we employ a split spectrum technique and investigate its performance for correcting ionospheric effects in InSAR-based ice velocity measurements in Greenland and Antarctica. Three case studies using ALOS PALSAR data are used to assess the performance of the split spectrum technique for ionosphere correction over a range of environmental parameters. We employ several approaches to evaluate the results, including visual inspection, profile analysis, comparison of experimental and theoretic errors, comparison with reference data from other sources, generation of double difference interferograms, and analysis of time series of multi-temporal data. Our experiments show that ionospheric distortions are observed regularly, and in our analyzed Greenland dataset and Antarctic dataset the ionospheric noise reaches 14 m/yr and 10 m/yr, respectively, which exceeds the signal associated with ice motion. Our analysis using several different approaches demonstrates that the split spectrum technique provides an effective correction. The split spectrum technique is also found to be superior to currently used approaches such as baseline fitting and multi-temporal averaging. The noise level is reduced by a factor of 70% in Greenland test areas and 90% in Antarctic test areas.

3.2 Introduction

Ice velocity is an important parameter for quantifying a variety of glaciological processes and understanding their related mechanisms (Joughin et al., 2010a). Large scale ice velocity measurements in polar regions are crucial for measuring ice mass loss and its contribution to the sea level rise (Dowdeswell, 2006). Remote sensing techniques allow measurements of ice dynamics over wide areas that would be otherwise difficult to access, making them an ideal tool for studying ice motion across Earth's large ice sheets (Joughin et al., 2010a; König et al., 2001).

[2] Liao, H., Meyer, F. J., Scheuchl, B., Mouginot, J., Joughin, I., & Rignot, E. (2018). Ionospheric correction of InSAR data for accurate ice velocity measurement at polar regions. *Remote Sensing of Environment*, *209*, 166-180.

Among all available remote sensing techniques, radar remote sensing, specifically synthetic aperture radar (SAR), has advantages due to its all-day and all-weather capabilities. Through the extensive use of SAR data in the last decade, several large scale ice velocity maps were published for both the Greenland and Antarctic ice sheets, which—for the first time—provided continent-wide and highly accurate ice dynamics data at high spatial resolution (Joughin et al., 2010b; Mouginot et al., 2017, 2012; Nagler et al., 2015; Rignot et al., 2011; Rignot and Mouginot, 2012). Two main approaches are used to derive ice velocity from multi-temporal SAR images: Speckle (ST) and Feature Tracking (FT) as well as SAR interferometry (InSAR) (Gray et al., 1998; Joughin, 2002; Joughin et al., 1998; Michel and Rignot, 1998). The ST approach uses cross-correlation of the coherent portion of the broad-band Speckle noise pattern to estimate ice motion from multi-temporal SAR image pairs. FT also uses cross-correlation but relies on image features rather than the speckle pattern. InSAR techniques derive ice motion from phase differences between repeated SAR acquisitions. Compared to InSAR, the cross-correlation methods used in ST is more robust for regions of fast flow, such as major outlet glaciers, where the interferometric phase may be impossible to unwrap because of excessive deformation. Sometimes it even works in areas where the speckle is decorrelated, but features provide enough correlation to measure fast flow area (feature tracking). Moreover, ST (as well as FT) provides estimates in both range and azimuth and therefore only requires a single multi-temporal SAR image pair to retrieve ice velocity in range/azimuth directions. A reduced need for reference points is an additional benefit of ST. One disadvantage of this technique is, however, that its resolution is limited by the need to cross-correlate patches with widths of several 10s of pixels. InSAR measures only signal in the range direction, but it provides a higher accuracy (by a factor of 10) and better spatial resolution (Bamler and Eineder, 2005). In areas of slow flow, e.g. the interior of Greenland and Antarctic, InSAR phase-based ice velocity estimates significantly improve the quality of the measurements compared to ST.

Accurate measurements of ice velocity are important in the interior regions of the large ice sheet as a reduced error in flow direction will allow a better determination of drainage basins. Accurate ice velocity is also of great importance for constraining ice sheet models, and better understanding the mechanisms of ice flow (Morlighem et al., 2011). One of the challenges for using SAR data for ice velocity measurement has been the impact of ionospheric disturbance (Gray et al., 1999; Joughin, 2002; Joughin et al., 2010b; Mouginot et al., 2017, 2012; Sánchez-Gámez

and Navarro, 2017; Rignot et al., 2011; Rignot and Mouginot, 2012; Strozzi et al., 2008). The ionosphere is particularly active in the Polar Regions. Variations in the spatial structure of the ionosphere between InSAR data acquisition times introduce a differential ionospheric phase screen in the interferograms, which acts as a source of noise for the ice velocity measurements. This ionospheric signal varies with time (e.g., time relative to solar max, diurnal variations) and location (e.g., stronger near the magnetic poles), and distorts ice velocity measurements if not appropriately corrected. A recent study revealed that the ionosphere introduces an average of 17m/yr and 8m/yr error in ST-based ice velocity estimates from (Advanced Land Observing Satellite) ALOS (Phased Array type L-band Synthetic Aperture Radar) PALSAR SAR data for the West Antarctic and the East Antarctic region, respectively. (Rignot et al., 2011). Despite the recognized significance of the ionosphere in Polar Regions, there has been little work published on the correction of ionosphere effects for ice sheet velocity measurements. This is especially true for InSAR phase-based ice velocity measurement. Assessing this issue is important due to an increasing preference for low frequency SAR systems for cryosphere studies, which are more susceptible to the ionosphere than sensors at C- or X-band (9.6 GHz). In part, this trend is related to the higher coherence of L-band InSAR SAR data and the promise of better InSAR-based ice velocity information. An increase in the availability of L-band SAR images through past (ALOS PALSAR-1), current (ALOS-2 PALSAR-2) and future (NASA-ISRO Synthetic Aperture Radar mission (NISAR); Tandem-L; SAOCOM) L-band SAR sensors is contributing as well. Moreover, decreasing the revisit times of future mission also means that ionospheric effects will have a greater impact on ice velocity measurements.

Several techniques have been published in recent years that enable the correction of ionospheric effects from InSAR phase observables (Brcic et al., 2011, 2010; Gomba et al., 2016; Jung et al., 2013; Kim, 2014; Liao and Meyer, 2016; Liu et al., 2014; Meyer and Nicoll, 2008; Raucoules and de Michele, 2010; Rosen et al., 2010; Zhang et al., 2016). Among all available techniques, the split spectrum approach is seen as the most reliable technique for ionospheric phase correction. So far, however, the split spectrum ionosphere correction technique has not been tried in the context of ice velocity application and its performance in areas affected by significant ice motion has not yet been assessed.

In this paper, we apply the range split spectrum technique for correcting the ionospheric effect in InSAR ice velocity measurements. Selective case studies using the L-band ALOS-1 data

in Greenland and Antarctica are conducted to evaluate the effectiveness of the split spectrum processing in correcting InSAR phase observations at high latitude affected by ionosphere distortions. The paper is organized as follows: We reiterate the theory of split spectrum technique for InSAR ionosphere correction with an emphasis on ice velocity measurement. Subsequently, selected L-band InSAR case studies in both Greenland and Antarctica are presented to evaluate the significance of ionospheric effects for ice sheet velocity measurements. Using the split spectrum technique, differential ionospheric phase screens are extracted from the data and the interferograms with and without ionosphere correction are compared. Several approaches for correction performance assessment are introduced, including (1) comparing InSAR estimates with/without ionosphere correction to reference data, (2) experimental result and theoretical performance cross-validation, and (3) comparison of repeated velocity measurements, which includes double difference interferogram comparison and multi-temporal estimates standard deviation analysis. We show that the accuracy of split spectrum processing is commensurate with expectations. We compare the split spectrum approach to other methods such as the conventional baseline (polynomial) fitting and averaging of multiple observations approaches. We then conclude on ionospheric corrections for ice sheet motion.

3.3 Methodology

3.3.1 Ionosphere Effect on SAR and InSAR

The ionosphere is a mixture of electrons, ions and neutral molecules extending from tens of kilometers to around a thousand kilometers altitude. In Polar Regions, ionospheric turbulence are observed regularly due to plasma processes associated with aurora activities such as particle precipitation, high speed plasma convection, plasma instability and gravity waves (Pi et al., 2011). When a radar signal propagates through the ionosphere, the microwave signal experiences a signal phase shift (group delay and phase advance) and a polarimetric plane change (Faraday rotation). These effects, through image focusing, cause a range of image distortions depending on the spatial structure of the ionospheric refractivity. At macro-scales (>=synthetic aperture length at the ionosphere height), the ionosphere causes a polarization rotation and a phase shift. At shorter length-scales (<synthetic aperture length) turbulent signatures in the ionosphere distribution will lead not only to a variable phase shift but also geometric (e.g., azimuth and range shift) and polarimetric distortions (Meyer et al., 2006; Meyer, 2010; Xu et al., 2004). Variations of the ionospheric delay within the synthetic aperture will introduce a varying phase shift in the phase

history. The linear component of this ionosphere-induced phase shift causes an apparent Doppler shift that leads to an azimuth shift of affected parts on an image. Higher order terms of the ionosphere-induced within aperture phase advance lead to a reduction of image focus.

Differences in ionospheric phase advance at the acquisition times of an InSAR data pair manifest themselves as a differential ionospheric phase screens and differential azimuth shift that cause local decorrelation in SAR interferograms (often referred to as 'azimuth streaking effects' (Gray et al., 2000)) Azimuth streaks appear frequently in Polar Regions where ionospheric turbulence is often large. The magnitude of these shifts can be significant, potentially several single-look pixels. Phase-based ice velocity estimates are affected by the ionosphere in two aspects: (1) The aforementioned image distortion, especially the azimuth shift, usually causes decorrelation in SAR interferometry (Meyer and Nicoll, 2008); and (2) the differential ionospheric phase screen is superimposed on the ice velocity phase, and this needs to be separated from the true ice velocity signal.

3.3.2 Ionosphere Mitigation Strategies

3.3.2.1 Traditionally-used Empirical Methods

A set of mostly empirical approaches have traditionally been used to mitigate the impact of ionospheric effects on ice velocity measurement. These include: (1) Data weighting (Joughin et al., 2010b; Mouginot et al., 2017, 2012; Rignot et al., 2011; Rignot and Mouginot, 2012). (2) Data stacking (Joughin, 2002; Mouginot et al., 2012, 2017). (3) Directional filtering (Chae et al., 2017; Millan et al., 2017; Strozzi et al., 2008). **Data weighting** is typically applied if data at different sensor wavelengths are available. Due to the prevalence of ionospheric effects in L-band, lower weights are typically assigned to L-band measurements in a joint analysis of multi-frequency data. This method helps in some cases, but it largely removes the advantage of having the high-coherence L-band data. While relative weights take the general relative sensitivity of L-band, C-band, and X-band data with respect to the ionosphere into account, they do not consider the strong variability of ionospheric turbulence with time. E.g., as data at different wavelengths are acquired on different times, the ionosphere effect may in fact be worse in C-band if data were acquired on a day with particularly strong ionospheric turbulence. Some other studies (Sánchez-Gámez and Navarro, 2017) simply throw away ionosphere contaminated estimates, but data in a lot of cases is limited.

Data stacking relies on the availability of multi-temporal data and performs temporal averaging of all available observations to reduce ionospheric delay effects. In many cases, this approach has been shown to reduce the impact of ionospheric distortions as well as other noise sources on ice velocity maps. However, this approach follows the assumption that the ionospheric effects are zero-mean random processes, a prerequisite that has not yet been verified. Existing ionospheric data (e.g. ionosphere derived from GPS or climatology ionospheric models) usually lacks the spatial and temporal resolution to provide sufficient ionospheric statistical information (Orús et al., 2002). Studies show ionospheric TEC at specific location varies with time (e.g. diurnal, seasonal), solar activity and space weather related event (Bagiya et al., 2009; Hernández-Pajares et al., 2011).

Directional filters take advantage of the often-distinct spatial patterns of ionospheric effects to separate ionospheric signal from ice velocity information. Filtering methods assume that ionospheric distortions have very specific shapes and that their spatial patterns are distinct from the structure of the geophysical signal of interest. Therefore, these empirical approaches often lead to insufficiently corrected data or to the unintentional removal of geophysical signal from the observations (Raucoules and de Michele, 2010).

3.3.2.2 Formal self-calibration Approaches

Several self-calibration approaches, that utilize the ionosphere distortion in SAR data to retrieve the ionosphere, have been developed in recent years and tested in non-polar regions. These approaches are categorized into the following types: The Faraday rotation based approach (Chen and Quegan, 2010; Freeman, 2004; Freeman and Saatchi, 2004; Kim and Papathanassiou, 2010; Li et al., 2014); the azimuth shift-based approach (the azimuth shift-based approach and the multi-aperture InSAR technique) (Chen and Zebker, 2014; Jung et al., 2013; Kim, 2014); and the split spectrum based approach (Brcic et al., 2011, 2010; Gomba et al., 2016; Liao and Meyer, 2014; Rosen et al., 2010). In essence, these methods estimate selected ionosphere-induced signal distortions (e.g., the previously mentioned geometry, phase and scattering matrix distortions) to derive an ionospheric phase screen that can be corrected from the data. Each category of correction techniques has their unique strengths and limitations. While the Faraday rotation approach provides absolute (in contrast to differential) ionospheric phase screens, it requires full-polarimetric datasets and its accuracy is reduced near the geomagnetic equator (Kim et al., 2015). Azimuth shift-based techniques have been successfully applied in earthquake applications

(Raucoules and de Michele, 2010; Zhang et al., 2016); but the effective separation of shifts caused by ionosphere from shifts related to ground motion is still difficult, making it a difficult to use method on ice sheets where there is strong surface motion [note that first techniques for separating ionospheric from deformation-related shifts are currently evolving (Gomba and De Zan, 2015; Kim and Papathanassiou, 2015)]. The split spectrum method decomposes the range spectrum of InSAR data into sub-bands with different center frequencies and inverts the differential ionosphere signal by exploring phase differences between sub-band interferograms. This technique has been tested for its effectiveness and shown to have high accuracy for ionosphere correction (Gomba et al., 2016). However, its functionality and performance has not been demonstrated for ice velocity application where processing is complicated by strong surface motion. In this paper, we apply the split spectrum technique to conduct ionosphere correction for ice velocity measurements.

3.3.3 The Split Spectrum Technique for Ionosphere Correction of InSAR Data over the Ice Sheets

The InSAR phase is a superposition of different phase components related to the earth curvature ($\emptyset_{flat}$), surface topography ($\emptyset_{topo}$), ionospheric ($\emptyset_{iono}$) advance and atmospheric ($\emptyset_{atmo}$) delay, as well as surface deformation ($\emptyset_{defo}$):

$$\emptyset_0 = \emptyset_{flat} + \emptyset_{topo} + \emptyset_{defo} + \emptyset_{atmo} + \emptyset_{iono} \quad (3.1)$$

where the flat earth phase can be written as $\emptyset_{flat} = \frac{4\pi}{c} B_{\parallel} \cdot f_0$, the topographic phase as $\emptyset_{topo} = \frac{-4\pi B_{\perp} h}{R\, c\, sin\,\theta} \cdot f_0$, the deformation phase as $\emptyset_{def} = \frac{4\pi}{c} \Delta r \cdot f_0$ and the atmospheric delay as $\emptyset_{atmo} = \frac{4\pi}{c} \int Ndl \cdot f_0$. In these equations, $B_{\perp}$ is the perpendicular baseline, $B_{\parallel}$ is the parallel baseline, h is the topographic height above a reference plane, R is the slant range distance between the satellite and antenna of the master data, θ is the incidence angle, c is the speed of light, f_0 is the radar center frequency, $\int Ndl$ is the integrated atmospheric refractivity along the path, and Δr is the surface deformation signal along the line-of-sight between the acquisition times of an InSAR data pair.

The ionospheric phase in Eq. (3.1) can be described as (F. Meyer et al., 2006):

$$\emptyset_{iono} = \frac{4\pi K}{c f_0} \Delta TEC \quad (3.2)$$

where ΔTEC is the differential total electron content integrated along the line-of-sight, and K is a constant of value 40.28. Eq. (3.2) shows that $\emptyset_{iono}$ is inversely related to the center frequency f_0

and is therefore a dispersive signal; all other phase components are linearly related to the radar center frequency f_0 and can therefore be summarized under a non-dispersive component $\emptyset_{non-disp}$ resulting in a simplified form of Eq. (3.1):

$$\emptyset_0 = \emptyset_{non-disp} + \emptyset_{iono} \quad (3.3)$$

The split spectrum approach (Brcic et al., 2011, 2010; Gomba et al., 2016; Liao and Meyer, 2014; Rosen et al., 2010), utilizes the dispersive nature of $\emptyset_{iono}$ in order to extract and correct ionospheric signatures from the data. To this end, the range spectrum of a SAR signal is typically divided into non-overlapped sub-bands with equal bandwidth. This process is implemented by applying a band-pass filter to the range spectrum of the full bandwidth dataset. In this work, a bandpass filter of 1/3 of the original range bandwidth is used, resulting in three sub-band SAR images with 1/3 of the original range resolution and slightly different center frequencies. The choice of sub-band bandwidth is in accordance with recent research, recommending 1/3 of the original bandwidth as the optimal choice for split spectrum processing (Bamler and Eineder, 2005; Gomba et al., 2016). Sub-band interferograms can then be formed within the corresponding sub-band data.

$$\emptyset_1 = \emptyset_{iono}\frac{f_0}{f_1} + \emptyset_{non-disp}\frac{f_1}{f_0} \quad (3.4)$$

$$\emptyset_2 = \emptyset_{\mathrm{iono}}\frac{\mathrm{f_0}}{\mathrm{f_2}} + \emptyset_{\mathrm{non-disp}}\frac{\mathrm{f_2}}{\mathrm{f_0}} \quad (3.5)$$

Where $\emptyset_1$ and $\emptyset_2$ stands for the interferometric phase corresponding to sub-bands with center frequencies of f_1, f_2, respectively. f_0 is the frequency of the full-band data.

This linear equation system can be solved for the dispersive ionospheric signal $\emptyset_{iono}$ as according to:

$$\emptyset_{iono} = \left(\emptyset_1 - \emptyset_2\frac{f_1}{f_2}\right)\frac{f_2}{f_0}\frac{f_1 f_2}{(f_2^2 - f_1^2)} \quad (3.6)$$

If $\emptyset_1$ and $\emptyset_2$ are two non-overlapping equal bandwidth sub-band interferograms, it is reasonable to assume that $\emptyset_1, \emptyset_2$ have the same statistical properties (i.e., $\sigma(\theta_1) = \sigma(\theta_2)$). Under these conditions, the accuracy of the ionosphere estimate is:

$$std(\emptyset_{iono}) = \sqrt{1 + \left(\frac{f_1}{f_2}\right)^2}\frac{f_2}{f_0}\frac{f_1 f_2}{(f_2^2 - f_1^2)}std(\emptyset_{sub-band}) \quad (3.7)$$

The sub-band interferogram accuracy can be expressed as (Bamler and Eineder, 2005):

$$std(\emptyset_{sub-band}) = \frac{1}{\sqrt{2N_b}}\frac{\sqrt{1-\gamma_{sub-band}^2}}{\gamma_{sub-band}} \quad (3.8)$$

Where $N_b = {}^{P_N \cdot \mathrm{B}_{sub-band}}/_{\mathrm{B}_{\mathrm{full-band}}}$ stands for the number of independent looks in the multi-looked sub-band data. P_N stands for the number of looks in the original full band data. $\mathrm{B}_{\mathrm{full-band}}$ is the full bandwidth of original image and $\gamma_{sub-band}$ is the sub-band interferometric coherence. It can be seen that the accuracy of the ionosphere signal estimate mainly depends on the frequency separation of the sub-bands and the coherence of the sub-band interferograms.

Once an estimated ionosphere phase screen $\emptyset_{iono}$ was derived using Eq. (3.5)-(3.7), we can then determine the ionosphere-corrected InSAR phase ready for ice velocity measurements according to

$$\emptyset_{def} = \emptyset_0 - \emptyset_{flat} - \emptyset_{topo} - \emptyset_{atmo} - \emptyset_{iono} \quad (3.9)$$

When applied to deriving ice velocity measurements, the topography-related phase $\emptyset_{topo}$ is typically corrected using an available DEM. For L-band data, atmospheric effects are limited and are, therefore ignored in our study. Furthermore, potential effects from orbit errors are calibrated out using reference data. Interested reader should refer to (Joughin, 2002; Mouginot et al., 2012) for more information on orbit calibration techniques over ice sheets.

3.4 Case Studies and Ionospheric Correction Performance Analysis

3.4.1 Data

3.4.1.1 ALOS PALSAR SAR Data

ALOS-1 PALSAR is an L-band SAR instrument with a revisit time of 46 days. L-band data is preferred for InSAR on the ice sheets as it retains coherence over longer time scale and provides higher quality information for ice motion analysis than data acquired at the C-band and X-band frequencies. In this study, three long tracks of ALOS-1 PALSAR SAR data are used to assess the performance of the ionospheric correction using the split spectrum technique. These data are selected from the archives of the ice velocity processing centers at the University of California Irvine and the University of Washington . All data used in this study have previously been used in the generation of ice velocity maps (Ian Joughin, 2015; Rignot et al., 2017.) , where ice velocity information was estimated through a weighted combination of data from different sensors (Joughin, 2002; Joughin et al., 2010b; Mouginot et al., 2012, 2017; Rignot et al., 2011; Rignot and Mouginot, 2012). Two of the datasets (track-41 and track-53) are located on the Greenland ice sheet. Track-41 data were acquired on Jan 20th, 2009 and Mar 7th, 2009, respectively and track-53 data were acquired on Nov 9th, 2008 and Feb 9th, 2009, respectively.

Track-41 consists of seven consecutive SLCs and spans about 400 km, while Track-53 consists of five SLCs and spans about 300 km. The coverage of these two datasets is shown in Figure 3.1(a). Detailed information on these two tracks can be found in Table 3.1. Both Greenland tracks traverse the interior of the ice sheet where the motion is small so that InSAR is the preferred method for measuring the ice velocity. As it is typical in this area, both interferometric data sets are contaminated by ionospheric effects. This noise can be easily identified from the prominent azimuth striking feature in the azimuth offset maps (Meyer et al., 2006). An example of the striking azimuth shift feature from track-53 is shown in Figure 3.2. As ice motion for large parts of these swaths is small, accurate correction of ionospheric signals is paramount to enable the unbiased extraction of statistically significant ice motion estimates.

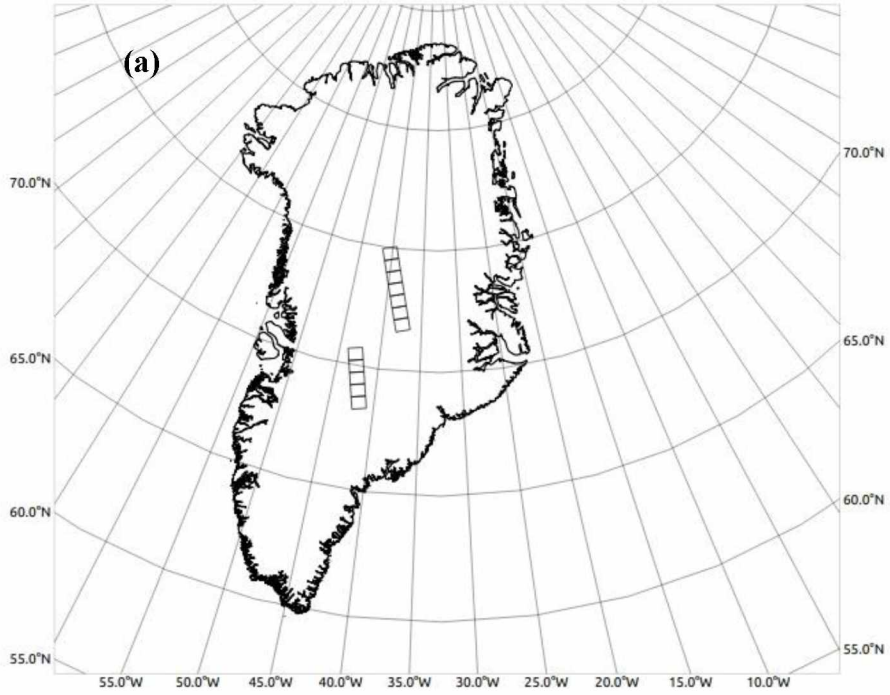

Figure 3.1 Data coverage for Greenland case study and Antarctica case study. (a) Greenland case studies data coverage. Interferometric ALOS/PALSAR Track 41 (the upper outline) and Track 53 (the lower outline). (b) Antarctica case study data coverage. The outline shows the location of the Interferometric ALOS/PALSAR Track471 frame 5540-5800.

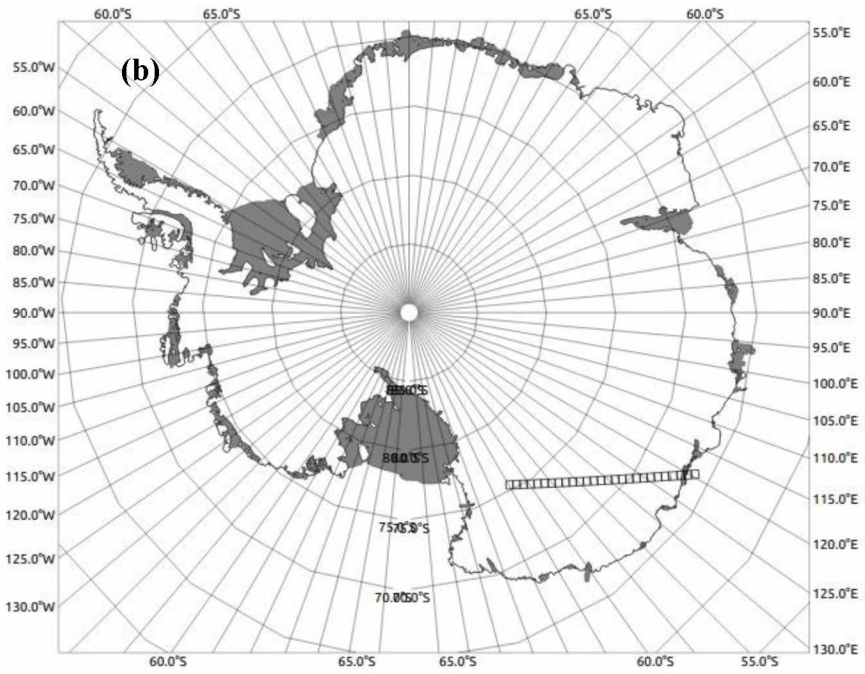

Figure 3.1 cont.

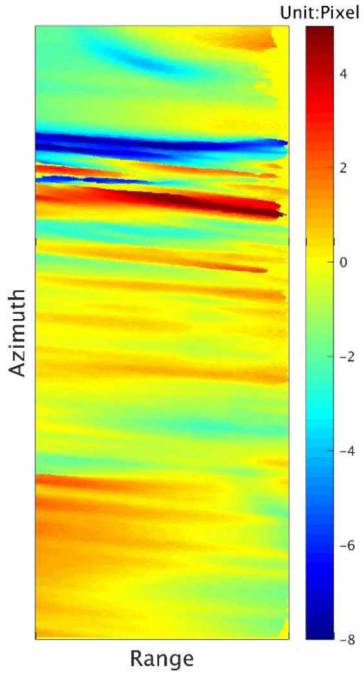

Figure 3.2 Greenland Track-53 azimuth component of the offset map derived using Speckle tracking.Most of the measured azimuth offsets are due to ionospheric effects. The azimuth resolution of Track-53 data is 3.1 m.

The third analyzed track is located in Antarctica and consists of ~30 ALOS-1 PALSAR SLCs spanning the continent from the interior to the coast more than 1500 km away (Figure

3.2(b)). Due to its length, the ice velocity covered by this swath is more diverse and includes slow flow areas in the interior and fast-moving outlet glaciers in the coastal region. Throughout the lifetime of ALOS-1 PALSAR, a total of 11 repeated acquisitions are available for this track, covering a time span from 2007 to 2011. From these 11 acquisitions, we form six interferograms with fixed 46-day temporal baselines. Interestingly, all six of these InSAR data experience significant ionospheric contamination with various signatures across the swath. Detailed information of the parameters of the Antarctic data track is included in Table 3.1.

Table 3.1 Greenland and Antarctica case studies: ALOS PALSAR data information.

InSAR data Information	**Track No.**	**Master**	**Slave**	**SLC Number**	**Temporal baseline**	**Bandwidth**
Greenland dataset	Track-41	2009/01/20	2009/03/07	7	46 days	28 MHz
		ALPSRP159281440~ ALPSRP159281500	ALPSRP165991440~ ALPSRP165991500			
	Track-53	2008/11/09	2009/02/09	5	92 days	
		ALPSRP148781370~ ALPSRP148781410	ALPSRP162201370~ ALPSRP162201410			
Antarctica dataset	Track-471	2007/10/14	2007/11/29	28	46 days	28 MHz
		ALPSRP091695530~ ALPSRP091695800	ALPSRP098405530~ ALPSRP098405800			
		2008/12/01	2008/10/16	27		
		ALPSRP152085540~ ALPSRP152085800	ALPSRP145375540~ ALPSRP145375800			
		2008/12/01	2009/01/16	27		
		ALPSRP152085540~ ALPSRP152085800	ALPSRP158795540~ ALPSRP158795800			
		2009/10/19	2009/12/04	27		
		ALPSRP199055540~ ALPSRP199055800	ALPSRP205765540~ ALPSRP205765800			
		2009/12/04	2010/01/19	27		
		ALPSRP205765540~ ALPSRP205765800	ALPSRP212475540~ ALPSRP212475800			
		2010/12/07	2011/01/22	31		
		ALPSRP259445540~ ALPSRP259445840	ALPSRP266155540~ ALPSRP266155840			

3.4.1.2 Reference Ice Velocity Data

Reference data for Greenland: We used Speckle-tracked results generated by the group of Ian Joughin and published in (Joughin, 2002; Joughin et al., 2017). For error mitigation (including ionospheric distortions), these Speckle-tracking results were averaged over all available data pairs from the Radarsat-1 and ALOS PALSAR sensors. Data pairs significantly affected by the ionosphere were discarded. Beyond that, no formal ionospheric correction was performed on these data. 1000s or more tie points were generated from this data at regular grids. In isolated locations, a few GPS points and some balance ties are added.

The quality of the reference data varies in space, mostly as a function of data availability. In the northern section of the Greenland ice sheet (Greenland Track-41), the reference data is assumed to be of good quality. In this area, good sampling by Radarsat-1 and ALOS resulted in more than 20 independent remote sensing-based velocity measurements, propagating to accurate velocity measurements after multi-temporal averaging was applied. In southern Greenland (Greenland Track-53), however, data availability was less favorable. In many places, reference data stems from only one or two original observations, resulting in lager errors. Unfortunately, the true absolute errors in the reference data are difficult to quantify, but a detailed analysis of the data indicates they are generally in the range of 2-5 m/yr (Joughin et al., 2017).

Reference data For Antarctica: Reference data for Antarctica was derived from a combination of ice velocity measurements based on speckle tracking (from Sentinel-1, Radarsat-2, ALOS/PALSAR, Radarsat-1, ENVISAT/ASAR and ERS) as well as feature tracking (from Landsat-8). While there is no direct correction of Ionosphere effects, Ionosphere mitigation is achieved by using data stacking and weighting from multiple sources acquired at different times. In addition, significant azimuth streaks were removed manually from offset maps before mosaicking a velocity product. The reference data was produced and delivered by the group around Eric Rignot, UCI, and is published in publications (Mouginot et al., 2012, 2017; Rignot et al., 2011). The uncertainty of annual ice velocity derived from each individual sensors was analyzed in (Mouginot et al., 2012, 2017; Rignot et al., 2011) and was found to be largely less than 20 m/yr. As the final velocity product published by UCI is the average of measurements from many sensors, we expect its accuracy to be significantly better.

3.4.2 Implementation of Split Spectrum for InSAR Ionospheric Correction

Our data processing flow consists of the following three major steps:

Fine co-registration: The first step is to precisely register the master/slave dataset using speckle tracking techniques (Joughin, 2002; Michel and Rignot, 1998). Due to the spatial variation of the pixel displacement caused by ice motion and ionospheric effects, conventional polynomial fitting methods for image co-registration do not work well. Instead we use a two-step registration strategy. First, we apply a conventional InSAR registration where we estimate offsets at sparse grid points and apply a low-order polynomial to fit the derived offset measurements. In this processing, we use 256 pixels by 256 pixels registration window and calculate a grid of several tens by several tens of offset estimates throughout the image. This step compensates for large wavelength shifts between InSAR image pair but does not correct for small-scale mis-registration effects related to the ionosphere and/or ice motion. We then implement a second fine registration using the master SLC and co-registered slave SLC from the first registration. While residual shifts are often small, they are typically highly localized and require dense grid sampling. Therefore, we calculate offsets at a dense $100m \times 100m$ sampling distance. We use a smaller registration window of 128 by 128 pixels to keep the registration procedure efficient while remaining robust in offset calculation. In the end, we use the polynomial fitted offset from the first registration and the more localized offset generated in the second registration to perform the final registration and resampling.

Full- and Sub-band interferogram formation and phase unwrapping: A second step in the ionospheric correction process is to generate the full-band and the sub-band interferograms and related full-band and sub-band unwrapped phase. To implement this step, we first apply a band-pass filter to the range spectrum of the SLCs to generate the sub-bands with specific frequency range, at the expense of range resolution. As the SAR signal is a modulated chirp signal, we shift the spectrum of each sub-band to make sure the center frequency of sub-band data matches the real spatial ground range frequencies. Once the sub-bands are prepared, full-band and sub-band interferograms are formed with the fine offset from the previous fine-registration processing. A digital elevation model (DEM) is used to subtract the topographic phase from both the full-band and sub-band data before phase unwrapping is conducted to arrive at an unambiguous phase map. The Greenland Ice Mapping Project (GIMP) DEM (Howat et al., 2014) was used over Greenland, which has a spatial resolution of 30 m and an overall RMS of 8.5 m over ice-cover terrain. For our data located in the interior of Greenland, the DEM quality is assumed to be better than this number (Howat et al., 2014). Over the Antarctic, the Bedmap2 DEM (Fretwell et al., 2013) was used,

which has an elevation uncertainty of 30 m. For SAR systems with narrow bandwidth, the split spectrum technique requires phase unwrapping steps as part of the ionospheric correction workflow. This can limit the correction performance in areas of low coherence, which are prone to phase unwrapping errors. This problem can largely be mitigated for large bandwidth data (e.g. NISAR 80 MHz bandwidth) where split spectrum technique can be used to avoid phase unwrapping (Libert et al., 2017).

In split spectrum processing, a typical strategy is to divide the full range spectrum into three sub-bands with a bandwidth of 1/3 of the full-bandwidth. The upper and lower sub-bands are used for ionosphere estimation (Gomba et al., 2016). This approach uses only a part of the available information (the middle sub-band is typically discarded), and therefore does not achieve the optimal ionospheric correction performance. The accuracy of the ionosphere can be improved by using a multiple sub-bands approach (Liao and Meyer, unpublished results.). Multiple sub-band processing, however, is more computationally intensive so we do not apply it to the large data sets used in this study.

Ionosphere phase screen correction: The third step uses the unwrapped sub-band phases to retrieve the ionosphere phase screen based on Eq. (3.6). The raw estimate of the ionosphere is initially noisy. Hence, it is important to develop appropriate methods to remove outliers and suppress noise. We implement a recursive phase unwrapping correction technique (Gomba et al., 2016) to correct for phase unwrapping errors. Subsequently, we apply a median filter to remove localized outliers in low correlation areas. In this process, a median filter is first applied to the raw ionospheric phase estimate and the difference between the raw ionospheric phase and its median filtered equivalent is calculated. Pixels with a difference larger than a threshold ($3\sigma, \sigma$ derived in accordance with Eq. (3.7) using an average coherence value) are classified as outliers and are discarded. Finally, an isotropic 2D gaussian filter is applied to suppress random noise. The ionosphere signature sometimes changes abruptly, and this usually leads to a high fringe density. A regular isotropic filter kernel may lead to biases in areas of high fringe density or near the edges of the interferogram. To solve this problem, an adaptive edge preserving filter (e.g. the adaptive bilateral filter) or joint estimators (Gomba and De Zan, 2017) can be used. Once the ionospheric phase was estimated, the ionosphere-corrected InSAR ice velocity measurement can be derived via Eq. (3.9). The accuracy of the raw ionosphere estimate can be quantified according to Eq. (3.7). This accuracy will be improved with data smoothing. Using an isotropic 2D Gaussian filter with a

standard deviation of σ_{filter}, the standard deviation of the filtered ionosphere estimate can be derived as:

$$\emptyset_{iono}^{filtered} = \frac{1}{2\sqrt{\pi}\sigma_{filter}} \frac{1}{\sqrt{2N_b}} \sqrt{1+\left(\frac{f_1}{f_2}\right)^2} \frac{f_2}{f_0} \frac{f_1 f_2}{(f_2^2 - f_1^2)} \frac{\sqrt{1-\gamma_{sub-band}^2}}{\gamma_{sub-band}} \quad (3.10)$$

3.4.3 Experimental Results and Analysis

3.4.3.1 Greenland Case Study ---Track 41

For Greenland data track-41, we generate topographic phase removed differential interferogram (Figure 3.3(a)) following the procedures in Section 3.4.2. As orbital state vectors distributed with SAR data are usually not accurate enough for ice velocity application, a baseline fitting process has to be implemented to account for baseline errors using control points with known velocity and elevation (Joughin, 2002; Joughin et al., 2017; Mouginot et al., 2012; Rignot and Mouginot, 2012). We implemented a baseline fitting (4th degree polynomial fitting) approach to the residue between the topography-corrected unwrapped phase and our reference data, which were available in a course grid and generated by averaging SAR data sets from historic sensors. See section 3.1.2 for more details (Joughin, 2002; Joughin et al., 2017). The baseline corrected interferogram for track-41 is displayed in Figure 3.3(a). Herein and after, these topography and baseline corrected but not formally ionosphere corrected data (interferograms and corresponding unwrapped phase) are referred to as the "measurements without ionospheric correction". Although baseline fitting is mainly aimed at correcting orbit errors, it can also help in compensating other longwave signals such as long wavelength tropospheric and ionospheric phase screens. Comparisons shown in Figures 3.3 (also Figure 3.6 and 3.8 in later experiment) show, however, that baseline fitting alone is not sufficient to mitigate ionospheric effects. Hence, using the split spectrum technique following the procedures in Section 3.4.2, we extract the differential ionospheric phase screen between the two image acquisition times (Figure 3.3(b)). The ionospheric correction will not compensate long wavelength signals related to orbit errors, therefore a separate baseline fitting is still needed after an initial ionospheric correction step. Applying the ionospheric phase correction and baseline fitting steps to the topography phase-removed interferogram, we get the topographic phase, ionospheric phase and baseline error-corrected interferogram shown in Figure 3.3 (c). (Herein and after, this topography, ionosphere, and baseline corrected results will be referred to as the "measurement with ionospheric correction"). We note that ionosphere correction should be implemented first before carrying out baseline fitting; otherwise the incorrect

order of ionosphere and baseline fitting will remove the long wavelength signals twice, potentially leading to biases in the InSAR estimates.

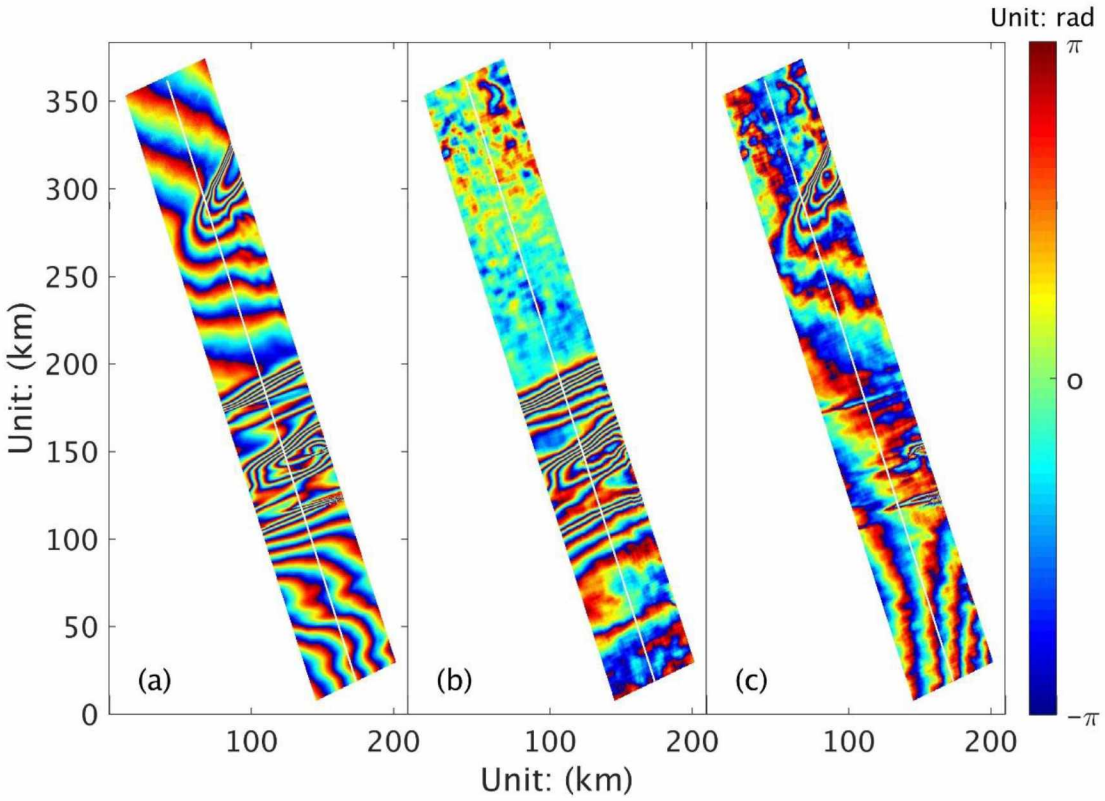

Figure 3.3 Greenland Track-41 data ionospheric correction result.(a) Mosaicked interferogram without ionospheric correction (topographic phase and orbit error removed). Phase related to ice motion and ionospheric signals can be seen. (b) Estimated ionosphere phase screen (wrapped) derived from the algorithm described in this study. (c) Interferogram with ionospheric correction (topographic phase, ionosphere, and orbit error removed; only ice motion left). 1 color cycle [-π, π] converted to ice velocity is about 1 m/yr. The velocity estimates are quoted in slant range.

In the following, four different approaches are used to analyze the achieved ionospheric correction performance. In a visual inspection, we see that the ice flow look-alike features in the central area of the swath (Figure 3.3(a)) are gone after ionosphere correction while the fringe feature at the northern part of the swath (Figure 3.3(c))—a true ice flow signal—remained.

For a more quantitative performance assessment, we compare the phase with and without ionospheric correction along a profile delineated in Figure 3.3. Phase profiles with (Figure 3.3 (c)) and without (Figure 3.3(a)) ionospheric correction are compared in Figure 3.4 (a). The estimated ionospheric phase (Figure 3.3 (b)) along the profile is displayed in Figure 3.4 (b). We see that the ionosphere, if uncorrected, leads to significantly biased ice velocity estimates. E.g.,

approximately 150 km along the profile, the extracted ionospheric signal would lead to an annual ice velocity bias of ~14 m/yr if uncorrected, while the actual ice velocity at that location is less than 1 m/yr. The largest ice velocity along this profile is less than 4 m/yr. After applying the split spectrum processing, this bias is largely removed and ice velocity follows a smoother trend.

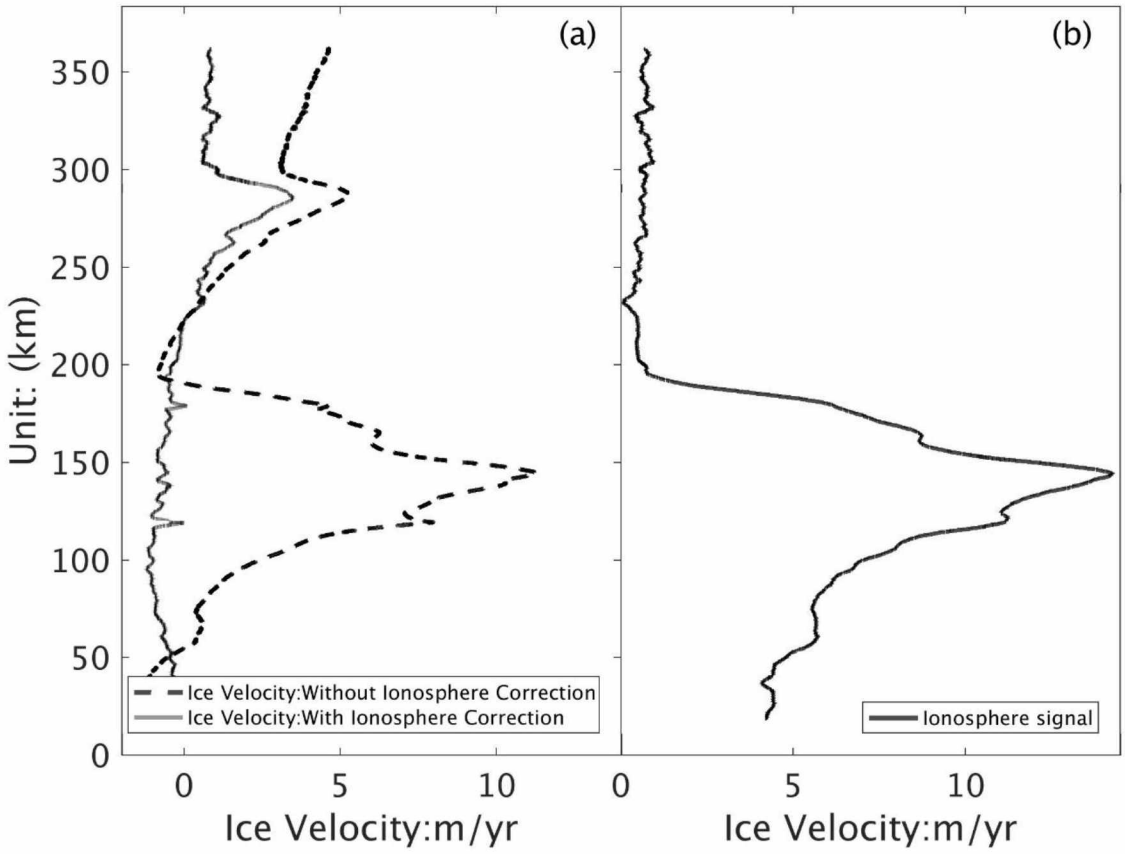

Figure 3.4 Greenland track-41 data ionosphere correction result profile analysis (the profile delineated as white line shown in Figure 3.3). (a) Phase profile without ionosphere correction (dash curve); Phase profile with ionosphere correction (solid curve). (b) The estimated ionosphere phase profile. The velocity estimates are quoted in slant range.

To provide a quantitative analysis of ionospheric correction performance, we calculate the standard deviation of the raw ionospheric estimate from the observed data and compare it to the theoretical error estimate derived from Eq. (3.7). To do so, we divide the ionospheric phase estimate into small tiles and calculate the phase standard deviation as a function of coherence for each tile. Standard deviation estimates are shown in Figure 3.5 as light gray dots. We add the median of all estimates as gray dashed bold line to better show the trend of phase noise with coherence. The theoretical ionosphere estimate estimated from Eq. (3.7) is shown as black line in

Figure 3.5. We see that the standard deviation of the empirical ionospheric phase estimate resembles the shape of the theoretic function. This raw ionosphere is noisy and has to be smoothed. After a multi-looking kernel of 12x18 resolution cells and an isotropic 2D gaussian filtering with a sigma of 30 resolution cells was applied to the raw ionosphere data, an average ionosphere error on ice velocity estimates of track-41 of only 0.04 m/yr could be achieved.

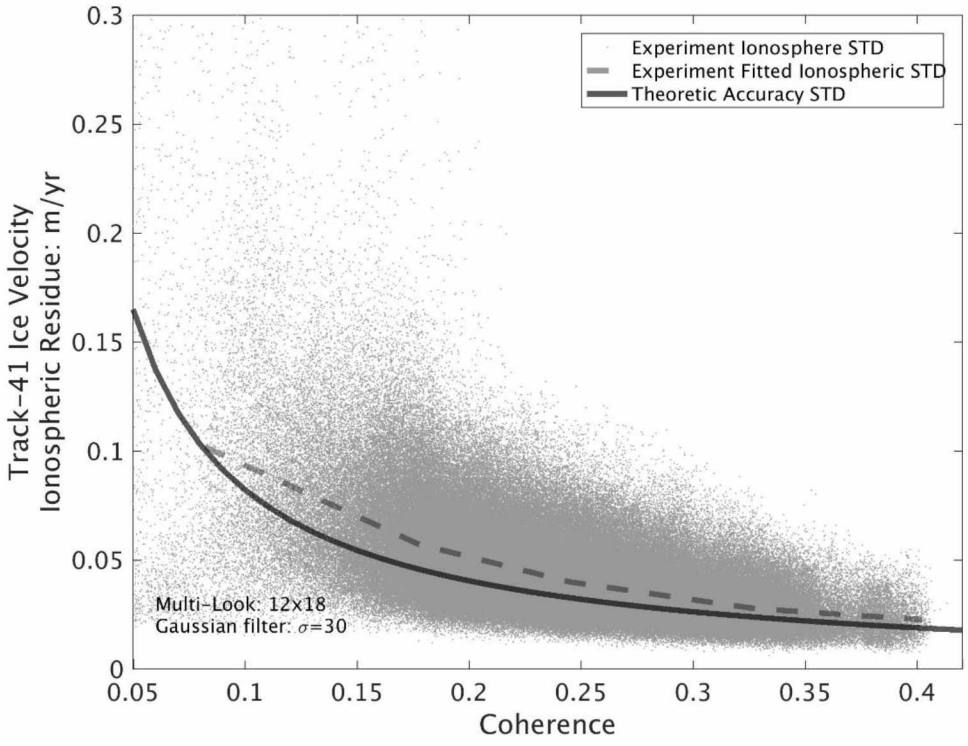

Figure 3.5 Greenland track-41 Ice velocity Ionospheric residue estimate vs its theoretic accuracy.X axis is the interferometric coherence, while Y axis is the ionospheric residue in ice velocity for Track-41 dataset.

As a final performance test, we use the ionosphere-corrected phase to derive ice velocity estimates and compare them to available reference data, which were available in a course grid and generated by averaging SAR data sets from historic sensors. (Joughin, 2002; Joughin et al., 2017). At the grid points for which reference data was available, the residual phase standard deviation between the InSAR estimate and reference data decreases from ~4.8 m/yr to 1.4 m/yr with ionospheric correction, corresponding to 70% accuracy improvement. Some of the remaining residuals are due to uncertainties in the reference points (~1 m/yr) and residual orbit errors, so the actual error with correction is likely better than 1.4 m/yr.

3.4.3.2 Greenland case study---- Track-53

We also test ALOS PALSAR track 53, another dataset located in the interior of Greenland. The interferogram without ionosphere correction is shown in Figure 3.6(a). The estimated ionosphere phase screen is presented in Figure 3.6(b) and the ionosphere-corrected phase is in Figure 3.6(c).

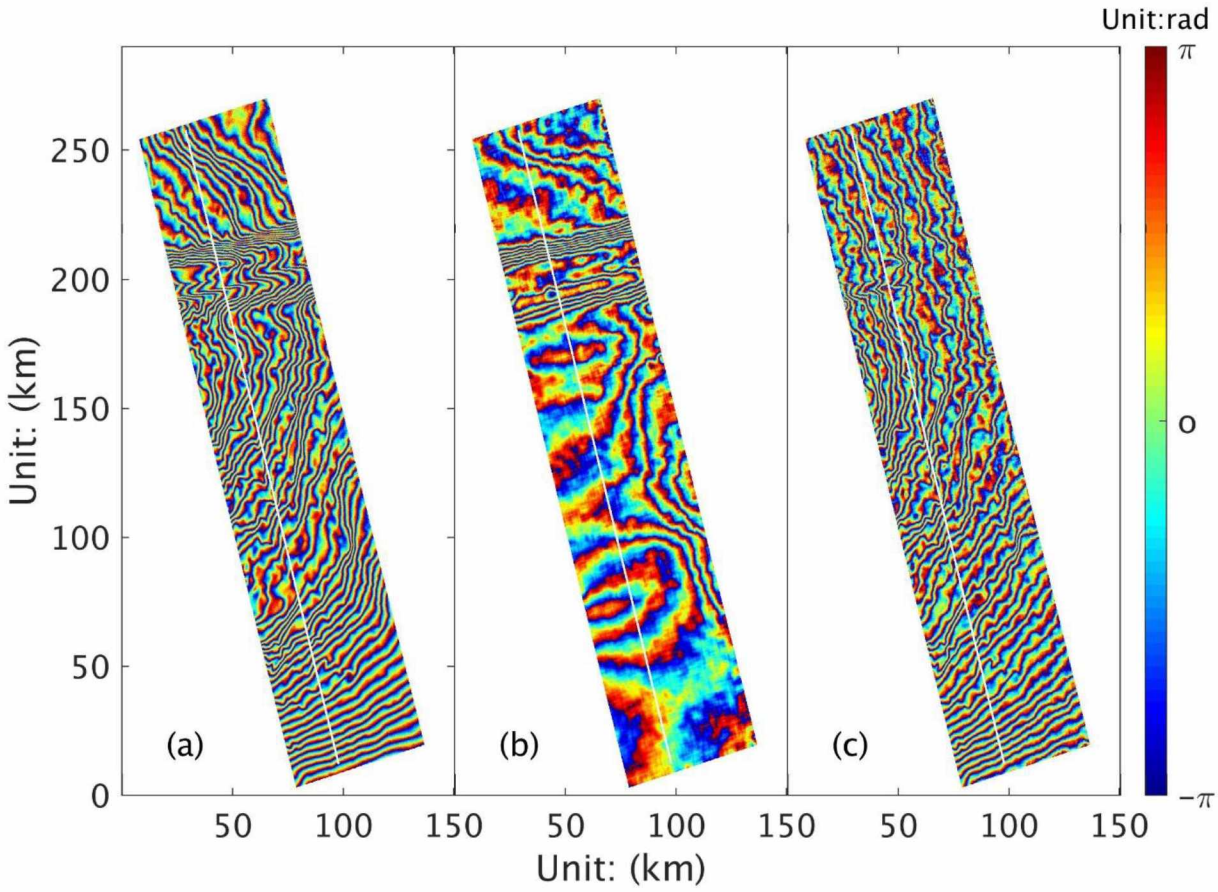

Figure 3.6 Greenland track-53 data ionosphere correction result. (a) Interferogram without ionospheric correction, where topographic phase and orbit error removed, ice motion and ionospheric signal are still presented. (b) Estimated ionosphere phase screen (wrapped) derived from the algorithm described in this study. (c) Interferogram with ionosphere correction (where topographic phase, ionosphere and orbit error has been removed, only ice motion left). 1 color cycle converted to ice velocity is about 0.5 m/yr.

A visual inspection of the uncorrected interferogram (Figure 3.6(a)) shows that the phase pattern that would indicate localized fast ice flow in the northern part of the image is an artifact of the ionospheric distortion. Similar to the previous example, a profile was extracted from the uncorrected and corrected phase and the result is presented in Figure 3.7.

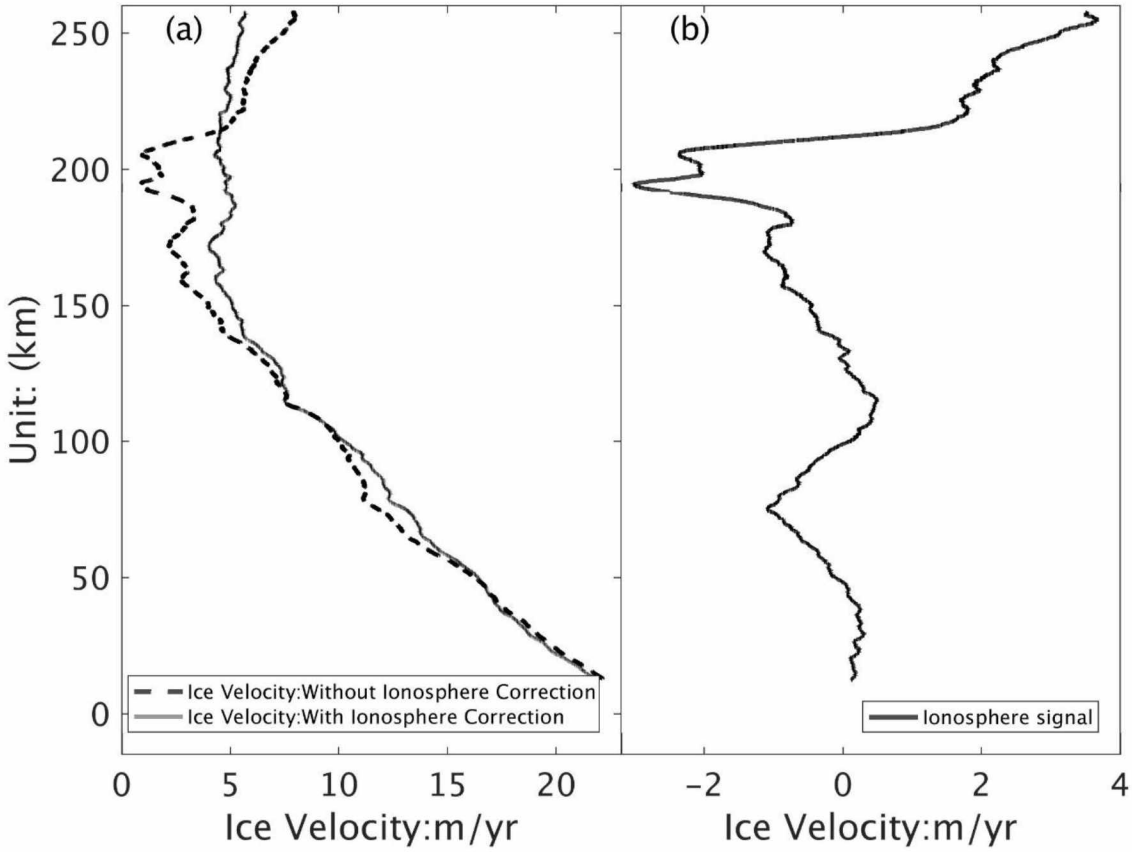

Figure 3.7 Track-53 data ice velocity ionospheric correction result profile analysis (the profile delineated as white line shown in Figure 3.6). (a) Phase profile without ionosphere correction (dash curve); Phase profile with ionosphere correction (solid curve). (b) The estimated ionosphere phase profile. The velocity estimates are quoted in slant range.

Figure 3.7(a) shows that the ionosphere is causing significant local biases in apparent ice velocity. Figure 3.7(b) indicates that ionospheric influence causes peak-to-peak ice velocity errors of 7.1 m/yr in this example. In the slowest moving parts of the profile along this swath, ionospheric errors are larger than the ice velocity signal itself, emphasizing the need for ionospheric correction. A comparison with reference points shows that the difference between InSAR estimates and the reference decreases from 5.2 m/yr to 4.0 m/yr with ionospheric correction. The improvement is less than in the first case study, however, we should note that in this case the fewer historic SAR samples were available to create reference data, resulting in less accurate reference data. The actual improvement with ionosphere correction is likely larger.

3.4.3.3 Antarctic Data

1) Time Series Data Analysis

In contrast to Greenland, where there is only one dataset, several repeat acquisitions are available for the selected ALOS PALSAR track in East Antarctica (see Figure 3.1(b)). In total, we generate six repeated SAR interferograms covering the period from 2007 to 2011. Detailed information about the six interferograms is in Table 3.1. We process the datasets following the procedures described in Section 3.2 and get the topographic phase corrected time series interferograms (Appendix A). We implement a baseline fitting (polynomial fitting) using the MEaSUREs ice velocity map (Mouginot et al., 2012, 2017; Rignot et al., 2011) as reference, the baseline corrected interferograms are displayed in Figure 3.8.

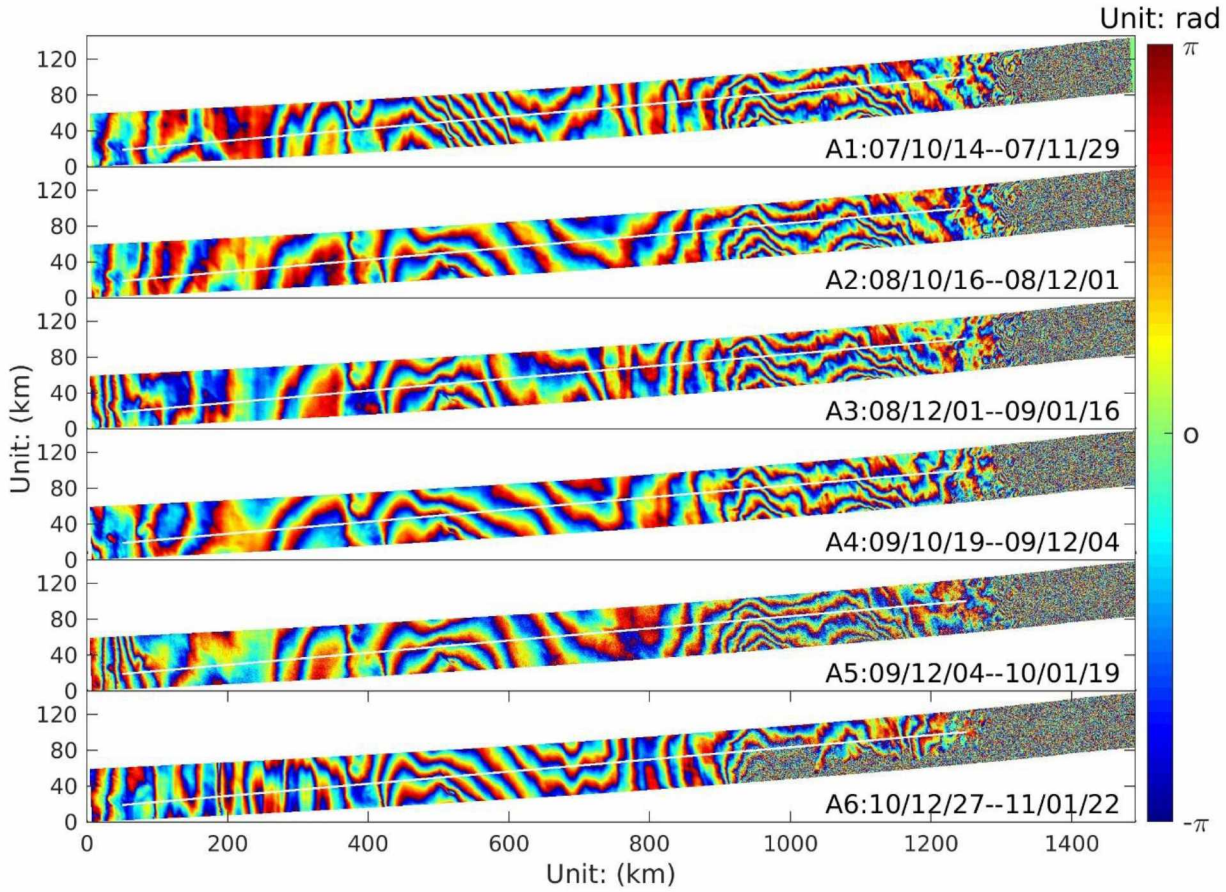

Figure 3.8 Antarctica Time series data Interferograms (A1-A6) without ionospheric correction. From top to bottom, interferograms A1-A6 corresponds to the six time periods as indicated above, where topographic phase is removed and baseline fitting has been implemented to remove orbit error (this may also remove long-wavelength ionospheric signals). Residue ionospheric signal remains in the above interferograms. 1 color cycle [-π, π] converted to ice velocity is about 1 m/yr.

Following the procedure in Section 3.4.2, the differential ionosphere phase screen corresponding to the six interferograms A1-A6 are estimated and the results are presented in Figure 3.9.

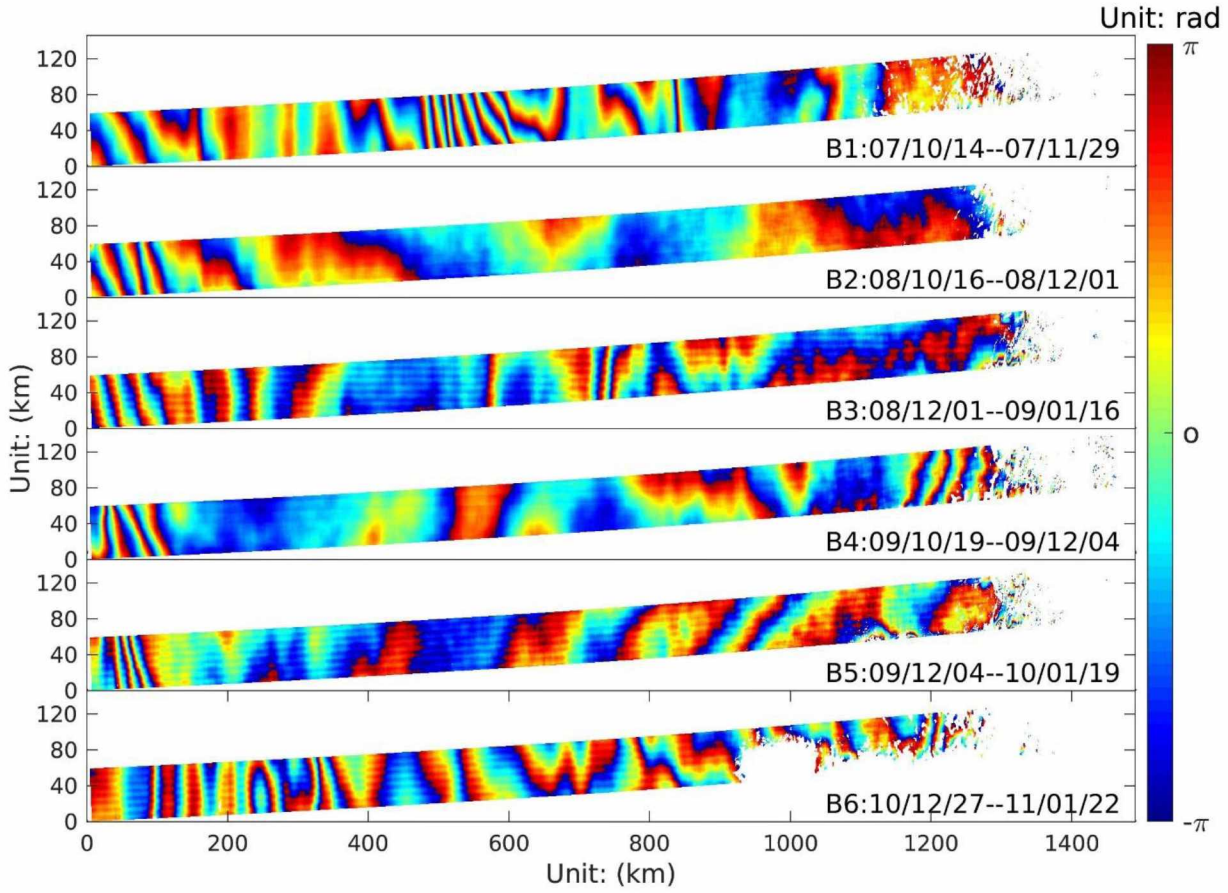

Figure 3.9 Estimated ionosphere phase screens. From top to bottom, B1-B6 indicates the differential ionospheres signal corresponding to the time series InSAR dataset A1-A6. 1 color cycle converted to ice velocity is about 1 m/yr.

Figure 3.9 shows that all six interferograms are contaminated by the ionosphere with peak distortions several tens of centimeters or more (maximum ionospheric distortions are found in the 2007 dataset, where the ionospheric distortion converted to ice velocity can reach about 10 m/yr). In Figure 3.9, the decorrelated area to the right of Figure 3.9 was masked out. Based on the estimates in Figure 3.9, we can see that all six data have severe ionosphere contamination along the 1500 km spanning distance; while the ionospheric distortion changes with geographic location and with times.

Applying the ionosphere phase correction and baseline fitting to the original interferograms, we get the ionosphere phase and baseline error corrected interferograms in Figure 3.10.

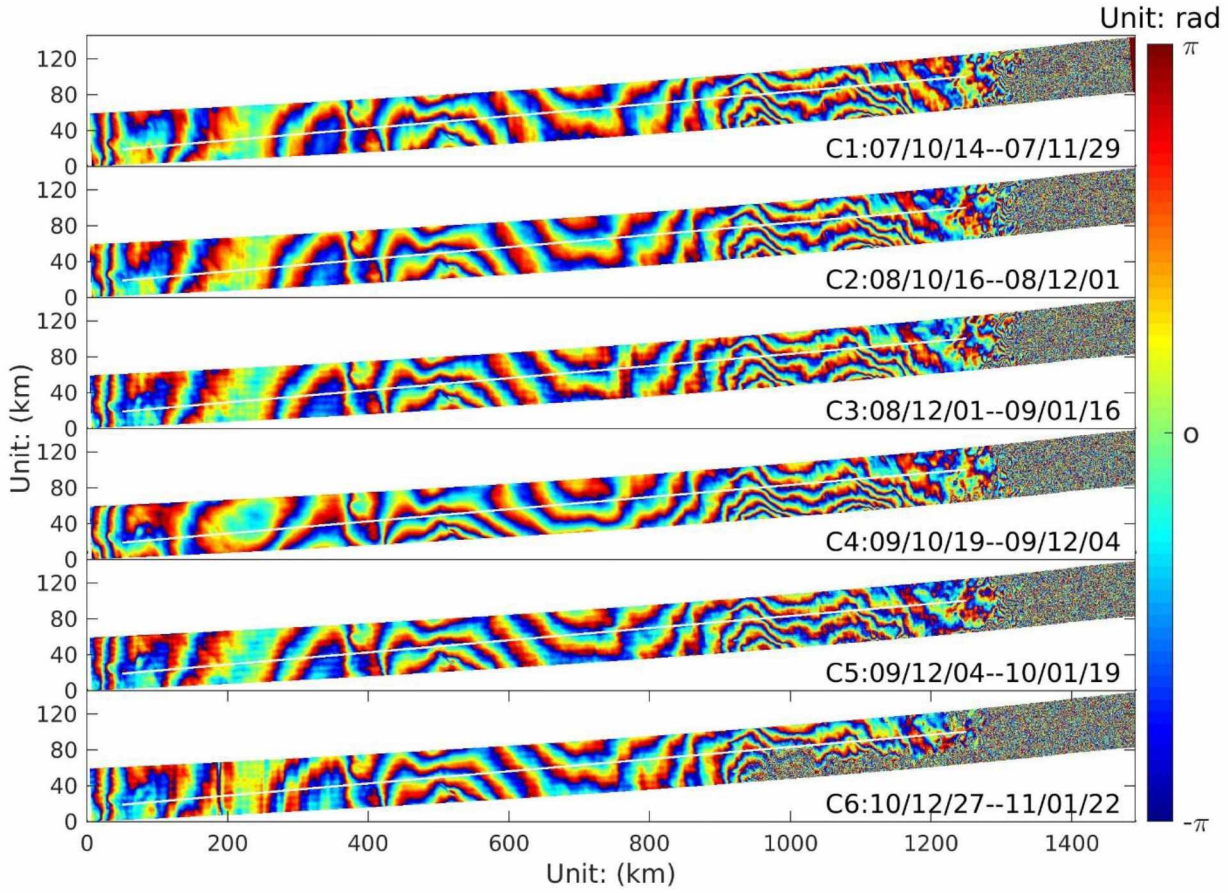

Figure 3.10 Antarctica time series Interferograms with ionosphere correction. From top to bottom, the six interferograms (C1-C6) for the six time periods indicated in the Figure, where topographic phase, ionospheric phase and orbit error has been removed. 1 color cycle converted to ice velocity is about 1 m/yr.

We see that the remaining ice velocity signal with ionosphere correction is now consistent among the six consecutive interferograms, showing a similar spatial pattern and similar magnitude, which is due to ice displacement. As changes in ice speed are not expected in this region of Antarctica (deep interior of East Antarctica), we demonstrate that our algorithm for ionosphere estimate works wells for this long track time series of ALOS acquisitions.

2) Ionosphere Correction Performance Analysis

We carry out several experiments to analyze ionospheric correction performance. We also compare split spectrum-based ionospheric correction to conventional ionosphere mitigation techniques from Section 3.3.1 to emphasize the benefit of a formal correction approach.

(a) Double Difference Interferogram Analysis

In the slow-moving interior of the ice sheet, we may reasonably assume the ice motion signal is the same for all six multi-temporal samples because we do not expect to observe changes in ice dynamics over this time scale in the deep interior of the continent. Hence, once ionospheric signals were removed, double difference interferograms (e.g., C2 – C1, C3-C1, …, C6-C1) should show a zero-mean phase with little phase standard deviation, making them a good means for assessing the performance of an ionospheric correction method and its benefit for ice velocity mapping.

To this end, we calculate double difference interferograms from the six interferograms without and with ionosphere correction (See interferograms without ionosphere correction in Figure 3.8, and with ionosphere correction in Figure 3.10). We select the first interferogram (A1 or C1) in 2007 as a reference and calculate its difference with the remaining five datasets (A2-A6 or C2-C6).

Figure 3.11 shows that without ionospheric correction, the double difference interferograms have large residual signal whose patterns vary with time. The residual signal does not correlate with the ice velocity patterns in the area. This signal does not meet our expectation of stable ice velocity over the different six-time periods, demonstrating that baseline fitting only is not sufficient for removing the ionospheric signal.

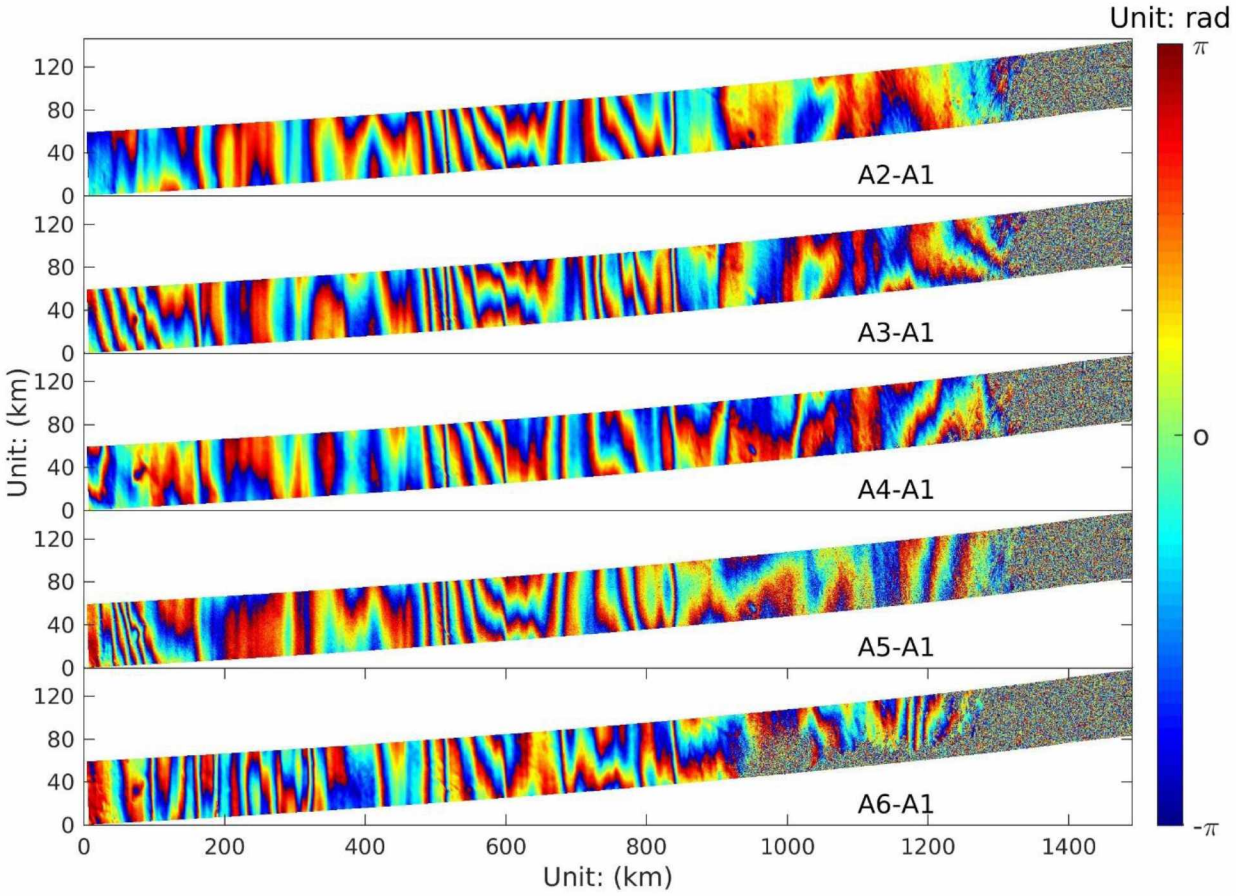

Figure 3.11 Antarctic time series data double difference interferograms (A2-A1, A3-A1,…,A6-A1) without ionosphere correction. 1 color cycle converted to ice velocity is about 1 m/yr. With ionospheric correction, the double difference interferograms (Figure 3.12) are near zero-mean with little residual spatial structure.

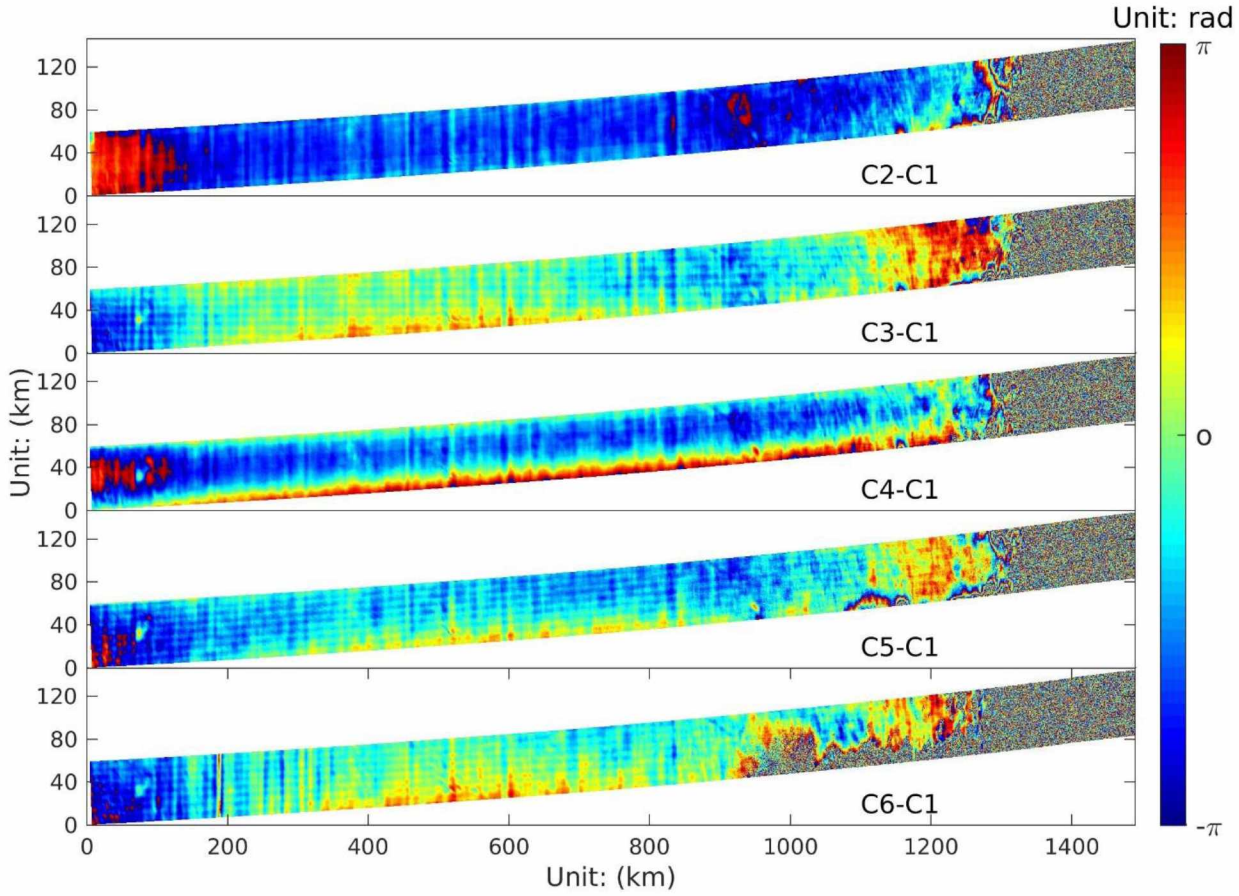

Figure 3.12 Antarctic time series data double difference interferograms (C2-C1, C3-C1,…, C6-C1) with ionosphere correction. 1 color cycle converted to ice velocity is about 1 m/yr.

This result is a strong indicator of the success of the ionosphere correction. Most residual signals are a function of the spatial filter needed to reduce noise in the raw ionospheric phase estimates. Narrow streaks are residual ionospheric signals caused by over-filtering in areas with steep phase gradients. Also visible are edge effects on the sides of the swath that are due to reduced spatial support for the phase filter near the edges.

For the sake of completeness of the experiment, we also calculate the only ionosphere corrected but no baseline fitting corrected interferograms and its double difference interferograms. The result is shown in Figure A-1 and A-3.

(b) Profile Analysis

To show the performance of the ionospheric correction for InSAR ice velocity measurements, we compare the InSAR derived ice velocity measurements to independent data derived via Speckle tracking (Mouginot et al., 2012, 2017; Rignot et al., 2011). We extract a profile

along the center of the swath (white line in Figure 3.8 and Figure 3.10) and plot the InSAR-based ice velocity measurements without and with ionospheric correction for each multi-temporal InSAR pair in Figure 3.13(a) and 3.13(b). Also plotted in Figure 3.13 is the ice velocity reference from ST measurements (Mouginot et al., 2012, 2017; Rignot et al., 2011).

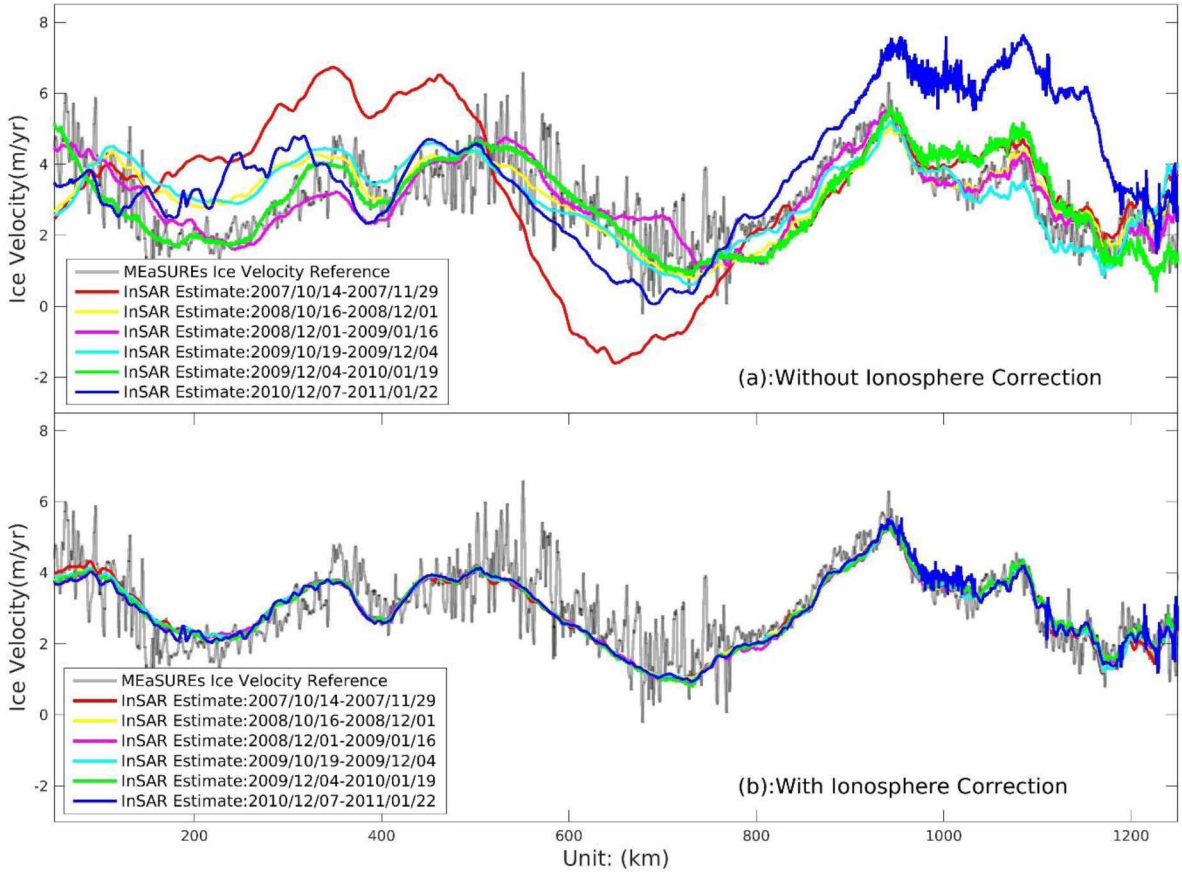

Figure 3.13 Antarctic time series Ice velocity measurements profile analysis without and with ionospheric correction. (a): Reference ice velocity from MEaSUREs, (Mouginot et al., 2012, 2017; Rignot et al., 2011) (Gray), and InSAR-derived ice velocity measurements without ionospheric correction(other colors). (b): Reference ice velocity from MEaSUREs, (Mouginot et al., 2012, 2017; Rignot et al., 2011) (Gray), and InSAR-derived ice velocity measurements with ionospheric correction(other colors). The velocity estimates are quoted in slant range.

Without ionospheric correction, the InSAR-based measurements deviate significantly from the speckle tracking estimate and vary with time. Deviations reaches up to 4 m/yr for some of the InSAR tracks. With ionospheric correction, the InSAR based ice velocity measurements match nicely with the MEaSUREs ice velocity (Figure 3.13 (b)). This agreement demonstrates the importance of the ionosphere correction for ice velocity analysis and indicates both the increase in precision and accuracy that can be achieved by our ionosphere correction algorithm. From Figure

3.13, we also see that the InSAR-based measurements are less noisy than the speckle-tracking-based result.

(c) Standard Deviation Analysis

To quantify the accuracy of our technique, we calculate the standard deviation of ice velocity estimates from the multi-temporal data both without and with ionospheric correction. The standard deviation estimates are shown in Figure 3.14 (a) for data without and in Figure 3.14 (b) for data with ionosphere correction.

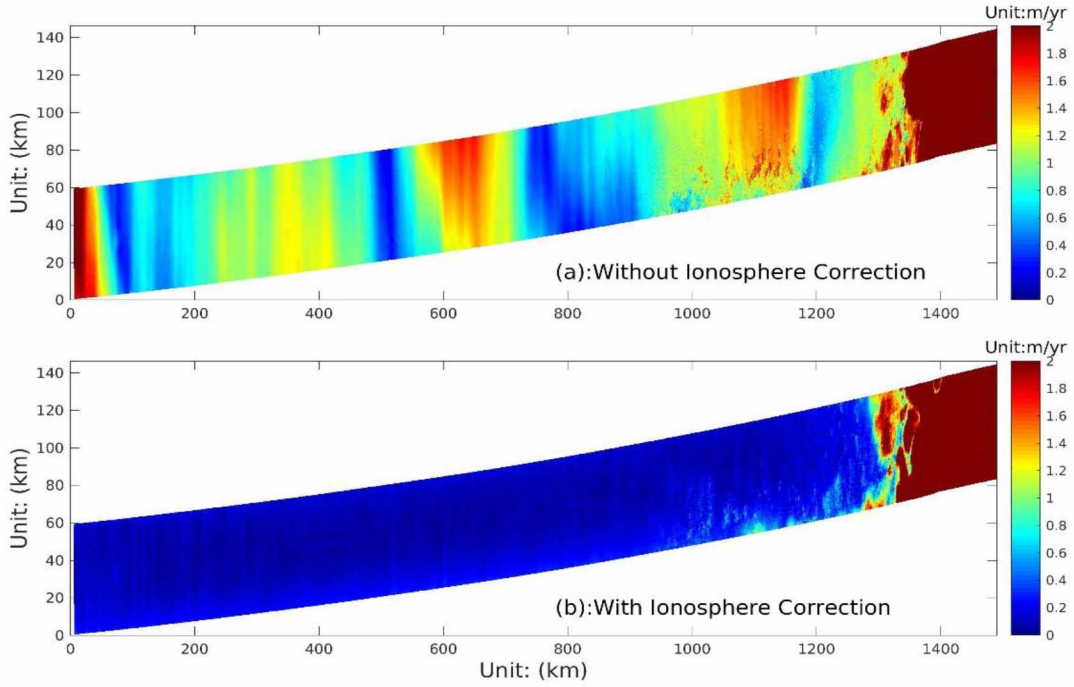

Figure 3.14 Antarctic time series InSAR-based ice velocity measurements standard deviation. Subplot (a) is the time series ice velocity measurements (A1-A6) standard deviation without ionospheric correction; subplot (b) is the time series ice velocity measurements (C1-C6) standard deviation with ionospheric correction.

We find that the phase standard deviation drops significantly after ionospheric correction was applied. Errors drop from 1.11 m/yr to 0.11 m/yr in areas that retain sufficient correlation, corresponding to a 90% decrease.

(d) Traditional Data Stacking vs Formal Split Spectrum Ionospheric Correction

One commonly used approach to reducing ionospheric noise has been the averaging of multiple repeat acquisitions to reduce the impact of the ionosphere on ice velocity estimates. Here, we compare one estimate with split spectrum-based ionospheric correction to this multi-temporal

averaging approach. We average the six measurements without ionosphere correction from Figure 3.8 and compare the result to one of the ionosphere-corrected measurements from Figure 3.10. In Figure 3.15, we plot the averaged ice velocity without ionosphere correction (red line), one of the six ice velocity measurements with ionosphere correction (blue line), and the reference ice velocity along the selected profile (gray line). We also plot the standard error of the average ice velocity without ionosphere correction (red shaded region) and the standard error of only one ionosphere corrected estimate (blue shaded region), respectively.

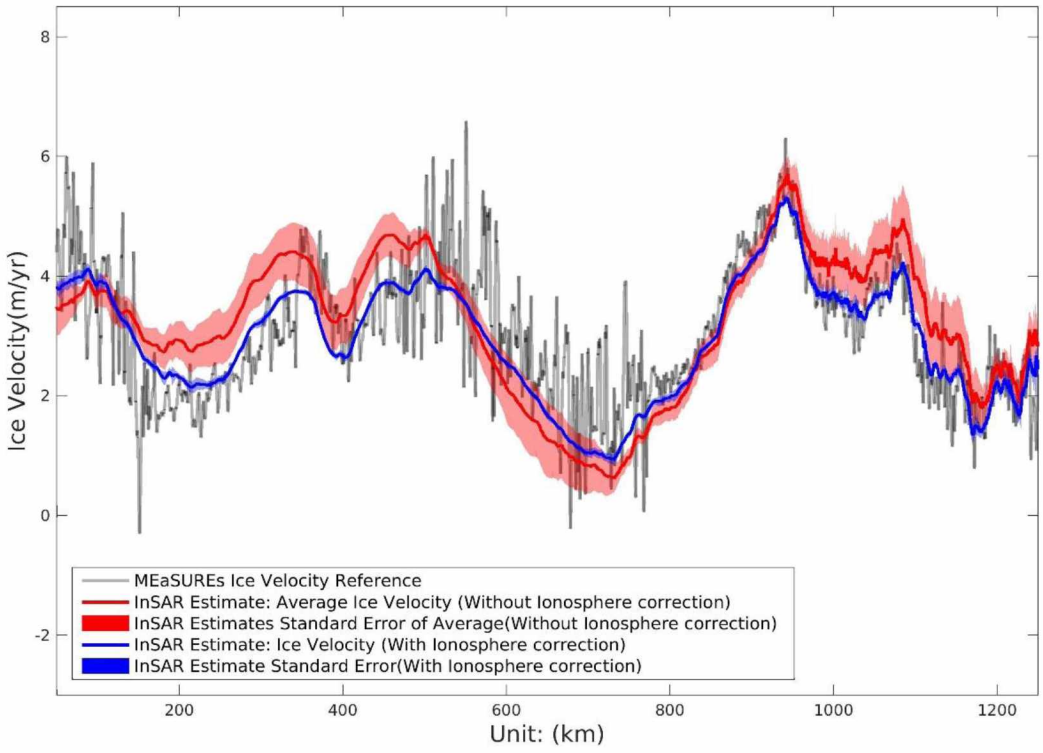

Figure 3.15 Average ice velocity of non-ionosphere-corrected measurements and its standard error (red line and shading) vs the ionosphere-corrected ice velocity and its standard error (blue line and shading). The gray curve is the reference ice velocity from ST (Mouginot et al., 2012, 2017; Rignot et al., 2011). The velocity estimates are quoted in slant range.

We find that the ionosphere-corrected ice velocity matches the reference ice velocity better than the average ice velocity without ionosphere correction. The error bounds for the velocity estimate with ionospheric correction is significantly reduced and only barely visible in Figure 3.15. Using areas with sufficient coherence, we estimate that the standard error of the average of the six interferograms without ionospheric correction corresponds to 1.11/sqrt(6)=0.45 m/yr, while the

standard error of a single measurement with ionospheric correction is 0.11 m/yr. Assuming this is representative of the typical ionospheric noise reduction over ice sheets and assuming that the ionospheric variation is uncorrelated in time, we can conclude that an average of about 100 (1.11/sqrt(N)=0.11, N=100) interferograms with no correction applied would be needed to achieve the noise performance of a single ionosphere-corrected measurement. Obviously, by averaging the ionosphere-corrected multi-temporal dataset, we can achieve even higher performance (standard error of the averaged ice velocity with ionosphere correction: 0.11/sqrt(6)=0.04 m/yr).

3.5 Conclusion

SAR interferometry is an important tool for measuring ice velocity in the Polar Regions, but ionospheric effects limit its performance, especially in regions with slow ice motion. In this paper, we use a range split spectrum technique to correct for ionosphere-induced phase distortions. Three case studies, including two in Greenland and a time series data set in Antarctica, are used to demonstrate the performance of split spectrum-based ionospheric correction by comparing ice velocity measurements without and with ionospheric correction. Visual analysis shows how ionospheric correction improves the determination of the ice flow direction. Quantitative analyses show that ionospheric effects strongly bias motion magnitudes and spatial motion patterns. We find that ionospheric correction reduces biases relative to in-situ reference data by up to 70% in the Greenland cases.

In Antarctica, we compare ice velocities at different times with reference data and calculate reduction in measurement noise. In all cases, we find that ionospheric correction leads to significantly reduced biases and improves ice velocity accuracy by a standard deviation reduction of 90%.

This study demonstrates that the split spectrum technique is effective in removing ionospheric distortions in the Polar Regions. The large reduction after ionospheric correction was applied indicates that the ionosphere has been the main error source in the ice velocity estimates used in our study. Using ALOS PALSAR InSAR data, we compare formal split spectrum-based ionospheric correction to traditionally used mitigation techniques such as baseline fitting and data stacking. From this study we found that in the order of 100 multi-temporal data would be needed to achieve a noise performance equivalent to a single ionosphere-corrected InSAR scene.

Potential drawbacks of adding split spectrum techniques to existing ice velocity approaches include an increase in the complexity of the InSAR processing workflow, higher computational costs, and the need for sufficient coherence to perform the required phase unwrapping steps.

From the Greenland and Antarctic case studies, we found that ionospheric noise in ice velocity estimates can reach up to 14 m/yr in interior Greenland and 10 m/yr in the Antarctic. In both cases, these errors exceed the ice velocity signal itself, making ice velocity analysis from a single SAR-based measurement difficult. Hence, applying the ionosphere correction is of great importance to warrant accurate ice velocity (both magnitude and flow direction) information. We expect that ionosphere correction will be of great importance for the analysis of short term glacier dynamics where averaging of multiple SAR scenes is not feasible. Also, ionospheric correction will allow more accurate small uplift or subsidence measurements near ice masses such as those related to glacier retreat and elastic rebound, oceanic tides, and sub-glacier lake drainage-induced deflation (Mouginot et al., 2017). With the ongoing (ALOS PALSAR-2) and future (NISAR, TanDEM-L) L-band SAR missions designed for ice velocity mapping, more L-band SAR data with shorter interval will be generated. We expect that ionospheric correction will be of great importance for these L-band systems to warrant accurate phase-derived ice velocity mapping and associated glaciology and geophysical research. The necessity of ionospheric correction in C- and X-band SAR still needs to be evaluated.

3.6 Acknowledgement

We thank associate editor George Riggs and the three anonymous reviewers for their effort in evaluating this paper. The insightful comments help greatly to improve the quality of this manuscript. Funding for the development of ionospheric correction techniques was provided through NASA grant NNX16AK55G. Eric Rignot, Bernd Scheuchl and Jeremie Mouginot were supported by NASA grants NNX13AI84A and NNX16AK91G. Ian Joughin was supported by NASA grant NNX16AK53G. ALOS PALSAR data sets were provided by JAXA/METI and were accessed through the services of the ASF DAAC.

3.7 Reference

Bagiya, M.S., Joshi, H.P., Iyer, K.N., Aggarwal, M., Ravindran, S., Pathan, B.M., 2009. TEC variations during low solar activity period (2005–2007) near the equatorial ionospheric anomaly crest region in India.

Bamler, R., Eineder, M., 2005. Accuracy of Differential Shift Estimation by Correlation and Split-Bandwidth Interferometry for Wideband and Delta-k SAR Systems. IEEE Geoscience and Remote Sensing Letters 2, 151–155. https://doi.org/10.1109/LGRS.2004.843203

Brcic, R., Parizzi, A., Eineder, M., Bamler, R., Meyer, F., 2011. Ionospheric effects in SAR interferometry: An analysis and comparison of methods for their estimation, in: Geoscience and Remote Sensing Symposium (IGARSS), 2011 IEEE International. IEEE, pp. 1497–1500.

Brcic, R., Parizzi, A., Eineder, M., Bamler, R., Meyer, F., 2010. Estimation and compensation of ionospheric delay for SAR interferometry, in: Geoscience and Remote Sensing Symposium (IGARSS), 2010 IEEE International. IEEE, pp. 2908–2911.

Chae, S.-H., Lee, W.-J., Jung, H.-S., Zhang, L., 2017. Ionospheric Correction of L-Band SAR Offset Measurements for the Precise Observation of Glacier Velocity Variations on Novaya Zemlya. IEEE Journal of Selected Topics in Applied Earth Observations and Remote Sensing 1–13. https://doi.org/10.1109/JSTARS.2017.2690799

Chen, A.C., Zebker, H.A., 2014. Reducing Ionospheric Effects in InSAR Data Using Accurate Coregistration. IEEE Transactions on Geoscience and Remote Sensing 52, 60–70. https://doi.org/10.1109/TGRS.2012.2236098

Chen, J., Quegan, S., 2010. Improved Estimators of Faraday Rotation in Spaceborne Polarimetric SAR Data. IEEE Geoscience and Remote Sensing Letters 7, 846–850. https://doi.org/10.1109/LGRS.2010.2047002

Dowdeswell, J.A., 2006. The Greenland ice sheet and global sea-level rise. Science 311, 963–964.

Freeman, A., 2004. Calibration of linearly polarized polarimetric SAR data subject to Faraday rotation. IEEE Transactions on Geoscience and Remote Sensing 42, 1617–1624. https://doi.org/10.1109/TGRS.2004.830161

Freeman, A., Saatchi, S.S., 2004. On the detection of Faraday rotation in linearly polarized L-band SAR backscatter signatures. IEEE Transactions on Geoscience and Remote Sensing 42, 1607–1616. https://doi.org/10.1109/TGRS.2004.830163

Fretwell, P., Pritchard, H.D., Vaughan, D.G., Bamber, J.L., Barrand, N.E., Bell, R., Bianchi, C., Bingham, R.G., Blankenship, D.D., Casassa, G., others, 2013. Bedmap2: improved ice bed, surface and thickness datasets for Antarctica. The Cryosphere 7.

Gomba, G., De Zan, F., 2017. Bayesian Data Combination for the Estimation of Ionospheric Effects in SAR Interferograms. IEEE Transactions on Geoscience and Remote Sensing 55, 6582–6593.

Gomba, G., De Zan, F., 2015. Estimation of ionospheric height variations during an aurora event using multiple semi-focusing levels, in: 2015 IEEE International Geoscience and Remote Sensing Symposium (IGARSS). IEEE, pp. 4065–4068.

Gomba, G., Parizzi, A., De Zan, F., Eineder, M., Bamler, R., 2016. Toward operational compensation of ionospheric effects in SAR interferograms: the split-spectrum method. IEEE Transactions on Geoscience and Remote Sensing 54, 1446–1461.

Gray, A.L., Mattar, K.E., Sofko, G., 2000. Influence of ionospheric electron density fluctuations on satellite radar interferometry. Geophysical Research Letters 27, 1451–1454.

Gray, A.L., Mattar, K.E., Vachon, P.W., Bindschadler, R., Jezek, K.C., Forster, R., Crawford, J.P., 1998. InSAR results from the RADARSAT Antarctic Mapping Mission data: estimation of glacier motion using a simple registration procedure, in: Geoscience and Remote Sensing Symposium Proceedings, 1998. IGARSS'98. 1998 IEEE International. IEEE, pp. 1638–1640.

Gray, L., Mattar, K., Short, N., 1999. Speckle Tracking for 2-Dimensional Ice Motion Studies in Polar Regions: Influence of the Ionosphere., in: Proc. of the ESA Fringe'99 Meeting.

Hernández-Pajares, M., Juan, J.M., Sanz, J., Aragón-Àngel, À., García-Rigo, A., Salazar, D., Escudero, M., 2011. The ionosphere: effects, GPS modeling and the benefits for space geodetic techniques. Journal of Geodesy 85, 887–907. https://doi.org/10.1007/s00190-011-0508-5

Howat, I.M., Negrete, A., Smith, B.E., 2014. The Greenland Ice Mapping Project (GIMP) land classification and surface elevation data sets. The Cryosphere 8, 1509–1518. https://doi.org/10.5194/tc-8-1509-2014

Joughin, I., U.O.W., 2015. MEaSUREs Greenland Ice Sheet Velocity Map from InSAR Data, Version 2. https://doi.org/10.5067/OC7B04ZM9G6Q

Joughin, I., 2002. Ice-sheet velocity mapping: a combined interferometric and speckle-tracking approach. Annals of Glaciology 34, 195–201.

Joughin, I., Smith, B.E., Abdalati, W., 2010a. Glaciological advances made with interferometric synthetic aperture radar. Journal of Glaciology 56, 1026–1042.

Joughin, I., Smith, B.E., Howat, I.M., 2017. A complete map of Greenland ice velocity derived from satellite data collected over 20 years. Journal of Glaciology 1–11.

Joughin, I., Smith, B.E., Howat, I.M., Scambos, T., Moon, T., 2010b. Greenland flow variability from ice-sheet-wide velocity mapping. Journal of Glaciology 56, 415–430.

Joughin, I.R., Kwok, R., Fahnestock, M.A., 1998. Interferometric estimation of three-dimensional ice-flow using ascending and descending passes. Geoscience and Remote Sensing, IEEE Transactions on 36, 25–37.

Jung, H.-S., Lee, D.-T., Lu, Z., Won, J.-S., 2013. Ionospheric Correction of SAR Interferograms by Multiple-Aperture Interferometry. IEEE Transactions on Geoscience and Remote Sensing 51, 3191–3199. https://doi.org/10.1109/TGRS.2012.2218660

Kim, J.S., 2014. Development of ionosphere estimation techniques for the correction of SAR data.

Kim, J.S., Papathanassiou, K.P., Scheiber, R., Quegan, S., 2015. Correcting Distortion of Polarimetric SAR Data Induced by Ionospheric Scintillation. IEEE Transactions on Geoscience and Remote Sensing 53, 6319–6335. https://doi.org/10.1109/TGRS.2015.2431856

Kim, J.S., Papathanassiou, K., 2015. On the separation of Dynamic Scattering and Ionospheric Effects in SAR data.

Kim, J.S., Papathanassiou, K.P., 2010. Faraday rotation estimation performance analysis. EUSAR 2010.

König, M., Winther, J.-G., Isaksson, E., 2001. Measuring snow and glacier ice properties from satellite. Reviews of Geophysics 39, 1–27.

Li, L., Zhang, Y., Dong, Z., Liang, D., 2014. New Faraday Rotation Estimators Based on Polarimetric Covariance Matrix. IEEE Geoscience and Remote Sensing Letters 11, 133–137. https://doi.org/10.1109/LGRS.2013.2250478

Liao, H., Meyer, F., 2014. Ionosphere effect correction in InSAR using improved split spectrum processing, in: AGU Fall Meeting.
Liao, H., Meyer, F.J., 2016. A combined estimator for Interferometric SAR ionosphere correction, in: Geoscience and Remote Sensing Symposium (IGARSS), 2016 IEEE International. IEEE, pp. 6499–6501.
Liao, H., Meyer, F.J., n.d. An optimized split spectrum approach for Interferometric SAR Ionospheric effect correction. (Unpublished).
Libert, L., Derauw, D., d'Oreye, N., Barbier, C., Orban, A., 2017. Split-Band Interferometry-Assisted Phase Unwrapping for the Phase Ambiguities Correction. Remote Sensing 9, 879.
Liu, Z., Jung, H.-S., Lu, Z., 2014. Joint Correction of Ionosphere Noise and Orbital Error in L-Band SAR Interferometry of Interseismic Deformation in Southern California. IEEE Transactions on Geoscience and Remote Sensing 52, 3421–3427. https://doi.org/10.1109/TGRS.2013.2272791
Meyer, F., 2010. A review of ionospheric effects in low-frequency SAR—Signals, correction methods, and performance requirements, in: Geoscience and Remote Sensing Symposium (IGARSS), 2010 IEEE International. IEEE, pp. 29–32.
Meyer, F., Bamler, R., Jakowski, N., Fritz, T., 2006. The Potential of Low-Frequency SAR Systems for Mapping Ionospheric TEC Distributions. IEEE Geoscience and Remote Sensing Letters 3, 560–564. https://doi.org/10.1109/LGRS.2006.882148
Meyer, F.J., Nicoll, J., 2008. The impact of the ionosphere on interferometric SAR processing, in: Geoscience and Remote Sensing Symposium, 2008. IGARSS 2008. IEEE International. IEEE, pp. II–391.
Michel, R., Rignot, E., 1998. Flow of Moreno Glaciar, Argentina, from repeat-pass Shuttle Imaging Radar images: Comparison of the phase correlation method with radar interferometry. Journal of Glaciology.
Millan, R., Mouginot, J., Rignot, E., 2017. Mass budget of the glaciers and ice caps of the Queen Elizabeth Islands, Canada, from 1991 to 2015. Environmental Research Letters 12, 024016. https://doi.org/10.1088/1748-9326/aa5b04
Morlighem, M., Rignot, E., Seroussi, H., Larour, E., Ben Dhia, H., Aubry, D., 2011. A mass conservation approach for mapping glacier ice thickness: BALANCE THICKNESS. Geophysical Research Letters 38, n/a-n/a. https://doi.org/10.1029/2011GL048659
Mouginot, J., Rignot, E., Scheuchl, B., Millan, R., 2017. Comprehensive Annual Ice Sheet Velocity Mapping Using Landsat-8, Sentinel-1, and RADARSAT-2 Data. Remote Sensing 9, 364. https://doi.org/10.3390/rs9040364
Mouginot, J., Scheuchl, B., Rignot, E., 2012. Mapping of ice motion in Antarctica using synthetic-aperture radar data. Remote Sensing 4, 2753–2767.
Nagler, T., Rott, H., Hetzenecker, M., Wuite, J., Potin, P., 2015. The Sentinel-1 Mission: New Opportunities for Ice Sheet Observations. Remote Sensing 7, 9371–9389. https://doi.org/10.3390/rs70709371
Orús, R., Hernández-Pajares, M., Juan, J.M., Sanz, J., Garcıa-Fernández, M., 2002. Performance of different TEC models to provide GPS ionospheric corrections. Journal of Atmospheric and Solar-Terrestrial Physics 64, 2055–2062.
Sánchez-Gámez, P. and Navarro, F.J., 2017. Glacier Surface Velocity Retrieval Using D-InSAR and Offset Tracking Techniques Applied to Ascending and Descending Passes of

Sentinel-1 Data for Southern Ellesmere Ice Caps, Canadian Arctic. Remote Sensing 9, 442. https://doi.org/10.3390/rs9050442

Pi, X., Freeman, A., Chapman, B., Rosen, P., Li, Z., 2011. Imaging ionospheric inhomogeneities using spaceborne synthetic aperture radar. Journal of Geophysical Research 116. https://doi.org/10.1029/2010JA016267

Raucoules, D., de Michele, M., 2010. Assessing Ionospheric Influence on L-Band SAR Data: Implications on Coseismic Displacement Measurements of the 2008 Sichuan Earthquake. IEEE Geoscience and Remote Sensing Letters 7, 286–290. https://doi.org/10.1109/LGRS.2009.2033317

Rignot, E., Mouginot, J., 2012. Ice flow in Greenland for the International Polar Year 2008-2009: ICE FLOW GREENLAND 2009. Geophysical Research Letters 39, n/a-n/a. https://doi.org/10.1029/2012GL051634

Rignot, E., Mouginot, J., Scheuchl, B., 2011. Ice flow of the Antarctic ice sheet. Science 333, 1427–1430.

Rignot, E., Mouginot, J., Scheuchl, B., n.d. MEaSUREs InSAR-Based Antarctica Ice Velocity Map, Version 2.

Rosen, P.A., Hensley, S., Chen, C., 2010. Measurement and mitigation of the ionosphere in L-band interferometric SAR data, in: Radar Conference, 2010 IEEE. IEEE, pp. 1459–1463.

Strozzi, T., Kouraev, A., Wiesmann, A., Wegmüller, U., Sharov, A., Werner, C., 2008. Estimation of Arctic glacier motion with satellite L-band SAR data. Remote Sensing of Environment 112, 636–645.

Xu, Z.-W., Wu, J., Wu, Z.-S., 2004. A survey of ionospheric effects on space-based radar. Waves in Random Media 14, S189–S274.

Zhang, B., Ding, X., Zhu, W., Wang, C., Zhang, L., Liu, Z., 2016. Mitigating Ionospheric Artifacts in Coseismic Interferogram Based On Offset Field Derived From ALOS-PALSAR Data. IEEE Journal of Selected Topics in Applied Earth Observations and Remote Sensing 9, 3050–3059.

3.8 APPENDIX A

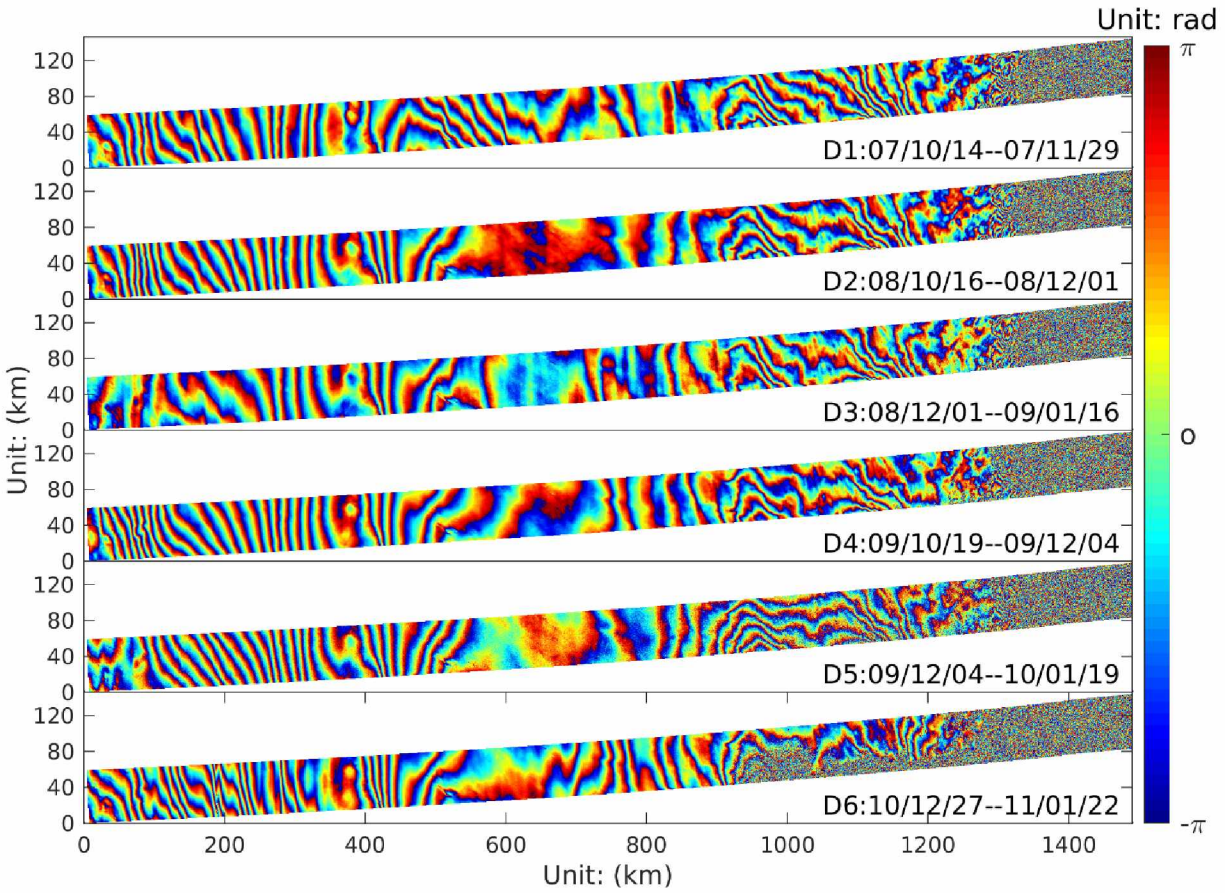

Figure A-1 Antarctica time series Interferograms (D1-D6), where topographic phase has been removed, while other signal like the ionosphere, baseline error and ice motion are remaining in it. 1 color cycle converted to ice velocity is about 1 m/yr.

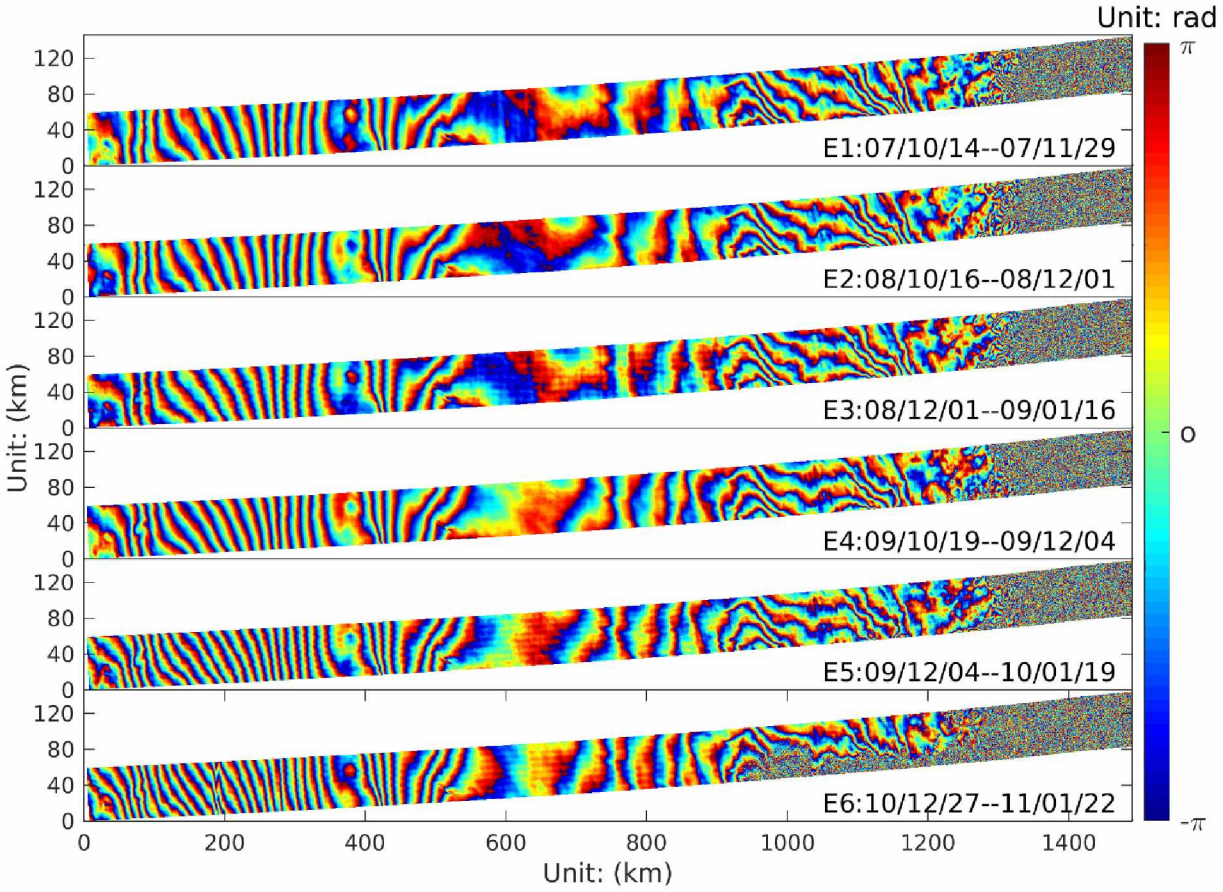

Figure A-2. Antarctica time series interferograms with ionospheric correction(E1-E6), where topographic and ionospheric phase have been removed, while baseline error still exists. 1 color cycle converted to ice velocity is about 1 m/yr.

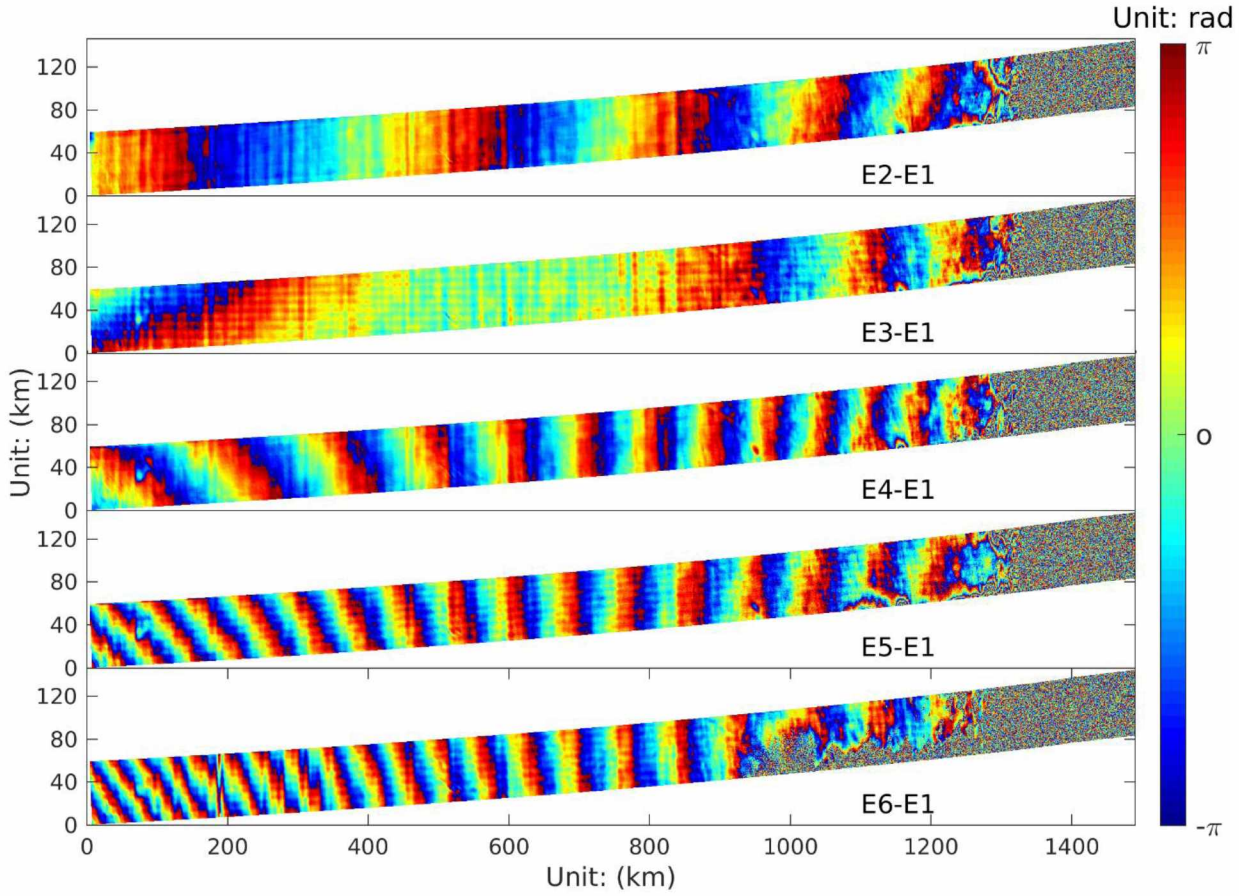

Figure A-3. Antarctica time series data double difference interferograms (E2-E1, E3-E1,…, E6-E1). 1 color cycle converted to ice velocity is about 1 m/yr.

Chapter 4

Ionospheric Correction of L-band InSAR Data for Monitoring Permafrost Subsidence: A Case Study with an Arctic Tundra Fire[3]

4.1 Abstract

Degrading permafrost can alter ecosystems, affect carbon recycling, damage infrastructure, and change land morphology and hydrology. SAR interferometry has been proven to be effective to detect uplift and subsidence in permafrost. InSAR-based permafrost studies are, however, susceptible to ionosphere disturbances, and this is especially true for low-frequency (e.g. L-band or P-band) SAR systems. Previous studies have recognized the ionospheric issue, but no research has systematically evaluated the frequency and the magnitude of ionosphere effects in InSAR-based permafrost studies. This study selects the Anaktuvuk River fire on the North Slope of Alaska as a study site and evaluates ionospheric effects on InSAR-based permafrost research over this site. We introduce an advanced split spectrum approach to facilitate InSAR ionospheric correction. With ionospheric correction accomplished, we generate 39 interferograms from 15 single look complex (SLC) SAR images, which is 15% more useable data than previous study were able to generate for this area of interest, allowing for better characterization of the permafrost-related ground deformation over short and long time scales. Our estimated ionospheric phase screen shows that all 39 interferograms experience ionospheric contamination at varying levels of magnitude. We present selected case studies to show different levels of ionosphere signals in SAR interferograms. We analyze the impact of ionospheric distortions on permafrost deformation estimates for typically-used processing approaches, namely single-interferogram analysis and time series processing. We show that ionosphere correction increases the capability to utilize single interferograms for permafrost studies. We show that with ionospheric correction, the very short-interval thaw season deformation, which was difficult to observe with InSAR before due to large errors induced by the ionosphere, becomes feasible. Also, ionospheric correction allows us to form InSAR measurements with large temporal baseline, spanning one entire thaw season. This helps to improve the accuracy of single interferogram derived seasonal deformation estimates. We verify our results by visual inspection and by analyzing improvements in standard deviation of the interferometric phase. For the latter, we calculate the standard deviation for an area outside of the

[3] Liao, H., Meyer, F. J., Liu, L (2018), Ionospheric Correction Of L-band InSAR Data for Monitoring Permafrost Subsidence: A case study with an Arctic Tundra Fire. Prepared for submission to Remote Sensing of Environment.

burn scar, expected to deform slowly and uniformly within the covered time span. For time-series InSAR-based permafrost measurements, we show that the ionospheric correction improves the accuracy of seasonal permafrost deformation rates. We validate our performance through visual inspection and through comparison with previous studies.

4.2 Introduction

Permafrost is defined as subsurface matter that remains frozen for at least two consecutive years (Marshall, 2011). It is estimated to occupy about 24% of the exposed land areas of the northern hemisphere (Zhang et al., 2008). It stores nearly twice as much carbon than is currently measured in the atmosphere (Tarnocai et al., 2009), and 3~10 cm sea-level equivalent ice volume (Zhang et al., 2008). Permafrost degradation has become an important topic regarding its role in affecting carbon recycling, damaging infrastructure, and changing land morphology and hydrology (Schaefer et al., 2014). Effective monitoring of permafrost dynamics (e.g. surface uplift (frost heave) and subsidence (thaw settlement)) is of significance for quantifying its dynamics and understanding its driving forces (Liu et al., 2014).

Recent research has demonstrated that SAR Interferometry (InSAR) is a useful tool for quantifying large scale surface subsidence caused by permafrost degradation (Liu et al., 2010; Rykhus and Lu, 2008; Short et al., 2011). Different wavelength (X, C, L) SAR data have been used for measuring permafrost frost heave and thawing subsidence. Among these studies, L-band SAR data is reported to be the most promising data source due to its ability to retain relatively high coherence, even for data separated by several years, in the changing Arctic environment of snow accumulation, melt, freeze, and vegetation growth. (Short et al., 2011). L-band SAR data, however, are susceptible to ionospheric distortions, affecting the achievable accuracy with which permafrost deformation can be measured and causing localized biases in the estimates (Iwahana et al., 2016; Liao et al., 2017; Liu et al., 2010; Rykhus and Lu, 2008; Short et al., 2011).

Previous permafrost-related InSAR studies dealt with ionospheric artifacts by either not using ionosphere-contaminated data (Eshqi Molan et al., 2018; Liu et al., 2014; Rykhus and Lu, 2008; Short et al., 2014, 2011) and/or by fitting and removing low-order polynomial surfaces to compensate for the large-scale phase residuals (often composed of a combination of ionospheric effects and phase screens related to orbit errors) (Iwahana et al., 2016; Liu et al., 2014; Short et al., 2011). These approaches can reduce the ionospheric effect to some extent, but also introduce some risks. Firstly, discarding data samples may significantly reduce temporal sampling, and may

not always be possible as the number of space-borne SAR images (especially historic data) is often limited. Secondly, the incurred reduction of temporal sampling could hinder the retrieval of important short-term dynamics of the active layer and the underlying permafrost. Thirdly, polynomial fitting for ionospheric signal compensation relies on the assumption that ionospheric phase contributions are mostly occurring at large spatial scales, an assumption that is often violated. Researchers have noticed that L-band InSAR analysis without an effective ionospheric correction scheme could lead to biases of short-term permafrost deformation measurements (Iwahana et al., 2016) as well as long-term deformation trends (Rykhus and Lu, 2008; Short et al., 2011). A thorough evaluation of how frequent and how large the ionosphere phase distortions are in permafrost InSAR data and the implementation of an effective approach correcting the ionospheric effect for permafrost studies are still missing.

To improve upon this situation, we introduce an advanced split spectrum approach for differential InSAR ionospheric phase screen estimation and correction. We select the Anaktuvuk River fire on the Alaska's North Slope as a case study to demonstrate the necessity for and the performance of our split spectrum technique for ionospheric correction of low-frequency InSAR data for permafrost deformation measurements. Ionospheric correction enables us to form 39 geophysically useful (sufficient coherence and low phase error) interferograms from 15 ALOS PALSAR SAR images, which is significantly more data than previous studies were able to produce from the same set of images (Liu et al., 2014). Analyzing the ionospheric phase screens extracted from these 39 interferograms, we found that all interferograms experienced measurable ionospheric distortions with varying magnitude and spatial patterns. We found that implementing ionospheric correction leads to significant improvement of InSAR-based permafrost analysis. First, we will show that permafrost analysis based on short-interval InSAR pairs is becoming possible, which was difficult or impossible without ionospheric correction. In addition, the integration of ionospheric correction and its related increase in data availability and measurement accuracy now allows us to analyze long-term permafrost deformation rate with higher accuracy.

The paper is organized as follows: We first briefly explain the various ionospheric effects that may appear in InSAR data, we then review the InSAR techniques for permafrost and the theory of the split spectrum ionospheric correction for permafrost studies (Section 4.3). In Section 4.4, we introduce our study site and the data we used in this study. In Section 4.5, we extract ionospheric phase screens from interferograms over our area of interest and present three

ionospheric distortions cases to demonstrate the necessity and the achievable correction performance. In Section 4.6, we evaluate the ionospheric correction performance and its benefit for the typically single interferogram-based and time series-based permafrost deformation estimate. We utilize all thawing date SAR acquisitions in 2008 and showcase the benefit of ionospheric correction for short time interval permafrost deformation estimates. We also provide annual estimates of the thaw season deformation using the earliest and latest SAR acquisitions of each thaw season. The visual inspection and our estimates compared to published results show the good performance of our ionospheric estimate. For time series InSAR permafrost, we demonstrate incorporating the ionospheric correction in the time series approach can help to improve the accuracy of permafrost deformation measurements. Different approaches were examined for validation. We also discuss the limitation of ionosphere correction in Section 4.7. The paper ends with a summary in Section 4.8.

4.3 Methodology

4.3.1 Ionospheric Effects in Interferometric SAR (InSAR) Data

The ionosphere is a mixture of electrons, ions, and molecules in a layer at an altitude ranging between several tens of km to more than 1,000 km above the Earth's surface. The ionosphere density is strongly affected by solar activity and its spatial distribution is controlled by the magnetic field and convection, storms and other meteorology activity (Pi, et al, 2011). The ionosphere can introduce a variety of distortions, such as azimuth/range image geometric distortions, phase advance, Faraday rotation, amplitude and phase scintillation, as well as image resolution degradation in low-frequency SAR data. A wide range of SAR-based studies, including both C- and L-band data, have reported significant ionospheric effects (Feng, 2011; Gray et al., 2000; Liao et al., 2018; Mattar and Gray, 2002; Raucoules and de Michele, 2010; Rykhus and Lu, 2008). The ionosphere is a function of solar cycle, geographical location, and time (seasonal and diurnal). Ionospheric irregularities predominantly happen in the aurora zones, the polar caps, and the post-sunset geomagnetic equatorial region (Fejer and Kelley, 1980; Perkins, 1975). Thus, applying the InSAR technique, especially for low-frequency data, at high latitude is at high risk of strong ionospheric distortions.

For InSAR-based permafrost studies, the most relevant ionospheric effects are the localized differential azimuth shifts in InSAR image pairs that cause decorrelation of the interferometric phase, as well as the differential phase distortions between the partner images of an InSAR pair

that lead to interferometric phase biases. An example of both of these effects is shown in Figure 1, where an ALOS PALSAR differential interferogram (topographic phase $\emptyset_{topo}$ corrected; acquisition dates: 20080724 and 20100914) over the Anaktuvuk river fire area is displayed. We see that the ionosphere-induced azimuth pixel offset (Figure 4.1(a)) can reach as much as 3 pixels. For areas experiencing large offsets, we see corresponding low coherence (Figure 4.1(c)) and noisy interferometric phase (Figure 4.1(b)). A differential ionospheric phase screen is superimposed on the permafrost deformation signal. For permafrost studies, the ionospheric induced coherence loss needs to be compensated, and the ionospheric phase need to be separated from the true permafrost deformation signal.

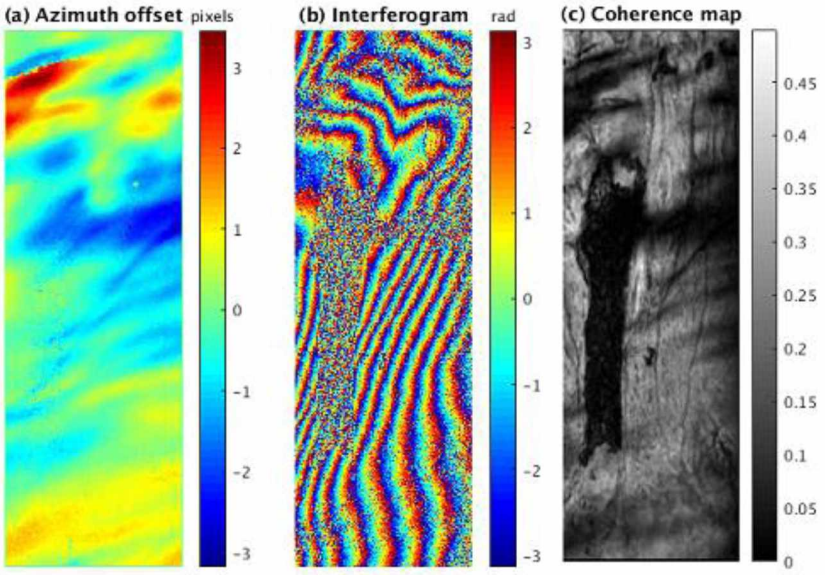

Figure 4.1 Ionospheric effect on L-band ALOS PALSAR InSAR data over the Anaktuvuk River fire area (20080724 to 20100914). (a) Ionosphere-induced azimuth offsets between the InSAR data pair; (b) Corresponding interferogram; (c) Corresponding coherence map.

4.3.2 SAR Interferometry for Permafrost Analysis

SAR interferometry approaches targeting surface deformation utilize coherent SAR data acquired at different times to form interferograms, which measure the phase difference between two SAR acquisition times. The interferometric phase $\emptyset_0$ represents a summation of phase contributions that relate to the SAR acquisition geometry $\emptyset_{flat}$, surface topography $\emptyset_{topo}$, traveling delay in atmosphere $\emptyset_{atm}$ and ionosphere $\emptyset_{iono}$, ground object scattering property (dielectric property, roughness, …) changes and other noises from instruments $\emptyset_{noise}$, as well as

ground deformation $\emptyset_{def}$ such as permafrost deformation, which is our signal of interest in this study.

$$\emptyset_0 = \emptyset_{flat} + \emptyset_{topo} + \emptyset_{atm} + \emptyset_{def} + \emptyset_{iono} + \emptyset_{noise} \quad (4.1)$$

For a successful InSAR estimate of, e.g., the permafrost deformation $\emptyset_{def}$, two key factors have to be satisfied: (1) the ground should not experience too much change ($\emptyset_{noise}$ should be small), in other words, the data needs relatively good coherence. For example, if the ground receives a large amount of snow or heavy rain, the surface scattering properties change dramatically between the acquisition times of an InSAR data pair, leading to decorrelation; (2) the ability to accurately separate our signal of interest $\emptyset_{def}$ from other phase contributions components. Here, the topographic phase $\emptyset_{topo}$ is usually accounted for using global DEMs with sufficient accuracy.

In recent years, there has been growing interesting in the use of InSAR for studying permafrost deformation (Li et al., 2015; Liu et al., 2015, 2010; Rykhus and Lu, 2008; Short et al., 2014, 2011) and in the study of external drivers such as tundra fire effects on permafrost degradation (Eshqi Molan et al., 2018; Iwahana et al., 2016; Liu et al., 2014). These past studies have typically used one of two different approaches in InSAR-based permafrost studies: One approach is to use single interferograms to quantify the deformation signal between the acquisition times of a specific InSAR image pair (Iwahana et al., 2016). From these measurements, the vertical ground deformation can be quantified as,

$$D = \frac{\lambda}{4\pi \cos\theta} \phi_{def} \quad (4.2)$$

Where λ is the wavelength of the radar signal, which is 23.6 cm for L-band ALOS PALSAR SAR data; θ is the radar incidence angle; ϕ_{def} is the unwrapped deformation InSAR phase in radians; D represents the vertical ground displacement between the acquisition times of InSAR pair. Single interferogram estimates directly measure permafrost deformation between the acquisition times of the InSAR pair. In the single interferogram approach, other phase components ($\emptyset_{flat}, \emptyset_{topo}, \emptyset_{atm}, \emptyset_{iono}, \emptyset_{noise}$) have to be accurately compensated in order to extract permafrost deformation ϕ_{def} with sufficient accuracy and precision. Traditional InSAR processing can deal well with $\emptyset_{flat}$ (using orbit vectors plus polynomial fitting), $\emptyset_{topo}$ (external DEM with sufficient accuracy), $\emptyset_{noise}$ (selecting data with relatively good coherence, multi-looking process, noise filtering). Sufficient correction for delays in the neutral atmosphere ($\emptyset_{atm}$) and the ionosphere ($\emptyset_{iono}$) is often less straightforward. For InSAR data at L-band frequencies (~1.27 GHz) acquired

over high-latitude areas, ionospheric phase contributions typically heavily outweigh neutral atmosphere effects. This is due to the typically turbulent nature of the ionosphere at these latitudes, the increased sensitivity of L-band data (as compared to data at C-band and X-band) to ionospheric distortions, and the low water vapor content of the rather cold neutral atmosphere in these regions. Therefore, neutral atmosphere effect $\emptyset_{atm}$ will be ignored in this study. In traditional approaches, ionospheric effects are typically treated using a polynomial fitting process, which is designed to compensate orbit errors but helps to mitigate large-scale ionospheric effects in the process. While useful for removing large scale phase contributions, small scale ionosphere signatures typically remain in the interferometric phase, potentially biasing permafrost information derived from InSAR. To further reduce ionospheric artifacts, researchers often focus on areas of limited spatial extent. E.g., (Iwahana et al., 2016) choose to focus on a small sub-area of the Anaktuvuk River fire scar and compared deformation estimate within the fire scar to deformation in unaffected areas. This approach to some extent reduces ionospheric effects, however, it bears risks as permafrost deformation can be spatially inhomogeneous such that small areas may not be representative of the permafrost behavior across the larger burn scar. This scenarios was reported in (Jones et al., 2015).

The other approach utilizes a time series InSAR solution combined with a permafrost deformation model and field temperature records to retrieve an estimate of the seasonal permafrost deformation. In this approach, the phase of a single interferogram is related to the measured vertical subsidence (D) between two the two data acquisition times t_1 and t_2 via the simplified Stephen equation (Liu et al., 2014)

$$D = \left(E_2\sqrt{A_2} - E_1\sqrt{A_1}\right) + B^{\perp}K \quad (4.3)$$

Where E_1, E_2 are the seasonal deformation coefficients corresponding to the InSAR pair acquisition dates (t_1, t_2, we make sure the slave data acquisition date (t_2) is always the later acquisition ($t_2 > t_1$)) .We assume that the deformation coefficients are the same for all pre-fire data and all post-fire data, and they are noted as $E_{pre-fire}$, $E_{post-fire}$ respectively. E_2, E_1 is decided according to:

$$E_i(i = 1,2) = \begin{cases} E_{pre-fire}\ (t_i < t_0) \\ E_{post-fire}\ (t_i > t_0) \end{cases} \quad (4.4)$$

t_0 is the fire end date that separates pre- from post-fire acquisitions. It was set to Nov 1, 2007 in this study (approximate end of the fire). A_1, A_2 are the accumulated degree day of thaw (ADDT)

corresponding to InSAR image pair acquisition times (t_1, t_2). The ADDT is calculated as the summation of the air temperature above 0℃ from the thaw onset date to the SAR data acquisition date. The thaw onset date of each year is fixed to May 1st in this study. We calculate the ADDTs using 1-hour sampling air temperature 5m above ground recorded at Toolit Lake Research Station (Environmental Data Center Team, 2018); $B^{\perp}$ is the perpendicular baseline associated with a particular interferogram and K is a variable representing errors in the DEM used for topographic correction of the interferometric phase.

If more than three independent interferograms are available, the deformation coefficients $E_{pre-fire}$ and $E_{post-fire}$ as well as the DEM error K can be estimated separately for the pre-fire and post-fire periods via the linear model:

$$\begin{bmatrix} d_1 \\ d_2 \\ \cdots \\ d_N \end{bmatrix} = G \begin{bmatrix} E_{post-fire} \\ E_{pre-fire} \\ K \end{bmatrix} \quad (4.5)$$

Or

$$d_{obs} = G \cdot m \quad (4.6)$$

Where $d_{obs} = \begin{bmatrix} d_1 \\ d_2 \\ \cdots \\ d_N \end{bmatrix}$ are the N time series interferogram observations. The N^{th} row of the design matrix G is:

$$G(N,:) = \begin{cases} \left[\sqrt{A_{N,2}} - \sqrt{A_{N,1}} \quad 0 \quad B_1^{\perp}\right] (if\ t_1 > t_0) \\ \left[0 \quad \sqrt{A_{N,2}} - \sqrt{A_{N,1}} \quad B_1^{\perp}\right] (if\ t_2 < t_0) \\ \left[\sqrt{A_{N,2}} \quad \sqrt{A_{N,1}} \quad B_N^{\perp}\right] \quad (if\ t_1 < t_0 < t_2) \end{cases} \quad (4.7)$$

$\sqrt{A_{N,1}}, \sqrt{A_{N,2}}$, $B_N^{\perp}$ are the ADDTs corresponding to the master and slave data acquisition dates and the InSAR data perpendicular baseline of the N^{th} interferogram, respectively. $m = \begin{bmatrix} E_{post-fire} \\ E_{pre-fire} \\ K \end{bmatrix}$ is the vector of unknowns. The data correlation matrix $C_{d_{obs}}$ is defined equivalently to (Liu et al., 2015): (1) if two interferograms are identical, then covariance $C_{i,j} = 1$; (2) if two interferograms share the same master or slave, then the covariance $C_{i,j} = 0.5$; (3) if one interferogram's master (slave) data is the same with the other interferogram's slave (master) data, then the covariance $C_{i,j} = -0.5$; (3) otherwise two interferograms share no common data, the covariance $C_{i,j} = 0$.

A weighted least square solution of the pre-fire and post-fire seasonal deformation coefficients as well as the DEM error is given by

$$m = \begin{bmatrix} E_{post-fire} \\ E_{pre-fire} \\ K \end{bmatrix} = (G^T C_{d_{obs}} G)^{-1} G^T C_{d_{obs}}^{-1} d_{obs} \quad (4.8)$$

We can then estimate the pre-fire, post-fire seasonal permafrost deformation rates

$$d_{pre-fire} = ADDT \cdot E_{pre-fire} \quad (4.9)$$

$$d_{post-fire} = ADDT \cdot E_{post-fire} \quad (4.10)$$

and the fire induced seasonal deformation increase can then be inverted

$$\Delta d = ADDT \cdot (E_{post-fire} - E_{pre-fire}) \quad (4.11)$$

The ADDT is the mean of the maximum ADDTs from 2007 to 2010 using all the dataset.

In time series InSAR approaches, similar data processing is implemented as that in the single interferogram approach, including polynomial fitting to remove orbit errors and large scale ionospheric signals. Also, the time series processing approach combines time series InSAR data with a deformation model to extract deformation coefficients, and then scale the deformation coefficients to seasonal deformation. This process, taking many data to achieve an 'average' deformation coefficient therefore mitigates the ionospheric effect to some extent.

With the estimated seasonal deformation coefficients of $E_{post-fire}$, $E_{pre-fire}$, we quantify the data uncertainty as follows (Liu et al., 2015):

$$\sigma_{d_{obs}} = \sqrt{\sum_{i=1}^{N} (d_i - \widehat{d_i})^2 / (N-2)} \quad (4.12)$$

Where d_i is our InSAR estimate and $\widehat{d_i}$ is the estimated subsidence calculated with Eq. (4.3) using our estimates of m in Eq. (4.8). The covariance of m

$$cov(m) = (G^T \sigma_{d_{obs}}^{-1} G)^{-1} = \begin{bmatrix} \sigma_{E_{post-fire}}^2 & \sigma_{E_{post-fire},E_{pre-fire}} & \sigma_{E_{post-fire},K} \\ \sigma_{E_{pre-fire},E_{post-fire}} & \sigma_{E_{pre-fire}}^2 & \sigma_{E_{pre-fire},K} \\ \sigma_{k,E_{post-fire}} & \sigma_{K,E_{pre-fire}} & \sigma_K^2 \end{bmatrix} \quad (4.13)$$

With the diagonal element of cov(m) are variance of each parameter, the pre-fire and post-fire seasonal deformation uncertainty can be estimated via:

$$\sigma_{pre-fire} = \sigma_{E_{pre-fire}} \cdot ADDT \quad (4.14)$$

$$\sigma_{post-fire} = \sigma_{E_{post-fire}} \cdot ADDT \quad (4.15)$$

With the increasing interest in permafrost dynamics and its implication for climate change, formal quantitative analyses of the ionospheric characteristic and permafrost deformation, effective correction methods, and a thorough evaluation of its effect on permafrost estimation and modeling are needed. Next, we introduce an advanced split spectrum technique for InSAR ionosphere correction and evaluate its performance for the ionosphere correction of permafrost-related InSAR data.

4.3.3 Ionospheric Delay Correction in InSAR-based Permafrost Studies

As mentioned previously, the measured interferometric phase of an InSAR data set with center frequency f_0 can be regarded as being the sum of a non-dispersive component $\left(\emptyset_{non-dispersive} = \emptyset_{flat} + \emptyset_{topo} + \emptyset_{tropo} + \emptyset_{def}\right)$ and a dispersive component ($\emptyset_{iono}$), such that the InSAR phase can be written as:

$$\emptyset_0 = \emptyset_{iono} + \emptyset_{non-dispersive} \quad (4.16)$$

As a dispersive contribution, the ionospheric phase component $\emptyset_{iono}$ is inversely proportional to the center frequency f_0, and related to the status of the ionosphere according to (Meyer, 2006):

$$\emptyset_{iono} = -\frac{4\pi K}{c f_0}\Delta STEC \quad (4.17)$$

Where $K = 40.28\ {}^{m^3}/_{s^2}$ is a constant, $\Delta STEC$ is the differential (between master and slave image) total electron content (TEC) integrated along the sensor's slant range direction, f_0 is the center frequency of the SAR signal, and c is the vacuum speed of light.

The split spectrum technique splits the SAR data range spectrum into several sub-bands resulting in several (lower resolution) images with different center frequencies (e.g f_1, f_2, ...). In previous publications (Brcic et al., 2010; Gomba et al., 2016), the full range spectrum is usually divided into three sub-bands, and the upper and lower sub-bands are then used for separate $\emptyset_{iono}$ and $\emptyset_{non-dispersive}$. These three sub-band configurations however do not fully use all available spectrum information, and, thus, can be improved. We propose a multiple sub-bands solution that divides the full range spectrum into N sub-bands, and then uses all N sub-bands for an overdetermined estimation of the dispersive ($\emptyset_{iono}$) and non-dispersive phase contributions ($\emptyset_{non-dispersive}$). Assuming a division of the full range spectrum into N sub-bands with center frequencies (f_1, $f_2, \ldots, f_N$), N sub-band interferograms can be formed using the corresponding sub-bands of the master and slave acquisitions. For the m^{th} (m=1, 2, …, N) interferogram, we get

$$\frac{f_0}{f_m}\emptyset_{iono} + \frac{f_m}{f_0}\emptyset_{non-dispersive} = \emptyset_m \quad (4.18)$$

With the N sub-band interferograms, we can form the following overdetermined equation system:

$$\begin{bmatrix} f_0/f_1 & f_1/f_0 \\ f_0/f_2 & f_2/f_0 \\ \cdots & \cdots \\ f_0/f_N & f_N/f_0 \end{bmatrix} \begin{bmatrix} \emptyset_{iono} \\ \emptyset_{non-disp} \end{bmatrix} = \begin{bmatrix} \emptyset_1 \\ \emptyset_2 \\ \cdots \\ \emptyset_N \end{bmatrix} \quad (4.19)$$

This can be rewritten in matrix form according to:

$$G \cdot m = d_{obs} \quad (4.20)$$

with

$$G = \begin{bmatrix} \frac{f_0}{f_1} & \frac{f_1}{f_0} \\ \frac{f_0}{f_2} & \frac{f_2}{f_0} \\ \cdots & \cdots \\ \frac{f_0}{f_N} & \frac{f_N}{f_0} \end{bmatrix} \quad (4.21)$$

$$m = \begin{bmatrix} \emptyset_{iono} \\ \emptyset_{non-disp} \end{bmatrix} \quad (4.22)$$

$$d_{obs} = \begin{bmatrix} \emptyset_1 \\ \emptyset_2 \\ \cdots \\ \emptyset_N \end{bmatrix} \quad (4.23)$$

As each sub-band interferogram are independent from each other, therefore the covariance matric of the d_{obs} is simply an identity matrix with dimension $N \times N$, $C_{d_{obs}} = \sigma^2_{sub-band}\begin{bmatrix} 1 & & & \\ & 1 & & \\ & & \cdots & \\ & & & 1 \end{bmatrix}$, where $\sigma_{sub-band}$ is the sub-band interferogram phase dispersion.

$$\sigma_{\emptyset_{sub-band}} = \frac{1}{\sqrt{2N_b}} \cdot \frac{\sqrt{1-\gamma_0{}^2}}{\gamma_0} \quad (4.24)$$

where $N_b = {Pix_N \cdot B_{sb}}/{B_0}$ stands for the number of the resolution element in a system with bandwidth B_{sb}. Pix_N stands for the number of pixels at the original full band data, which is decided by the multi-looking number. B_0 is the full bandwidth of original data and $\gamma_{sub-band}$ is the sub-band interferometric coherence. The solution for the unknown phase components $\emptyset_{iono}$ and $\emptyset_{non-disp}$ can be derived via the general least-squares solution.

$$m = \begin{bmatrix} \emptyset_{iono} \\ \emptyset_{non-disp} \end{bmatrix} = (G^T C_{d_{obs}} G)^{-1} G^T C_{d_{obs}}^{-1} d_{obs} \quad (4.25)$$

This overdetermined solution will increase the robustness and accuracy of the separation of dispersive and non-dispersive phase components and, hence, improves ionospheric correction. In our case, this is especially relevant for areas within the tundra fire where the burn has removed vegetation and part of the surface organic layer, resulting in significant changes of the scattering properties and corresponding partial decorrelation in this area. The reduced coherence often causes challenges for ionosphere estimation with conventional three sub-bands configurations.

The covariance of the unknown parameters can be estimated via:

$$cov(m) = \left[(G^T C_{d_{obs}} G)^{-1} G^T C_{d_{obs}}^{-1}\right] \cdot cov(d_{obs}) \cdot \left[(G^T C_{d_{obs}} G)^{-1} G^T C_{d_{obs}}^{-1}\right]^T \quad (4.26)$$

and the accuracy of the ionosphere estimation $\sigma_{\emptyset_{iono}}$ will be the square root of the first element of the parameter covariance matrix $cov(m)$.

For InSAR datasets with large spatial baseline, the common bandwidth in the master and slave datasets are shifted. This wavenumber shift or spectral shift effect in interferometric data affects the common bandwidth available for interferometric processing and has to be considered when formulating the ionospheric correction approach. Hence, we propose an advanced split spectrum InSAR processing strategy, which includes the wavenumber shift effect during split spectrum sub-band generation. The split spectrum technique including this spectral shift effect is discussed in detailed in a separate publication (Liao and Meyer, in preparation).

Once an estimate $\emptyset_{iono}$ for the ionospheric phase was derived, the ionospheric-corrected permafrost deformation estimate can be calculated via:

$$\emptyset_{def} = \emptyset_0 - \emptyset_{flat} - \emptyset_{topo} - \emptyset_{atm} - \emptyset_{iono} \quad (4.27)$$

In a real world implementation of this approach, an additional orbit correction has to be performed especially when data from legacy sensors are used for which the accuracy of orbit information was limited (Hooper et al., 2012). Hence, in our approach, a 6th order polynomial fit is applied to compensate for the orbit residual $\emptyset_{orbit-residual}$ after the correction for the phase components $\emptyset_{flat}, \emptyset_{topo}, \emptyset_{iono}$ was performed. To facilitate orbit correction, we mask out areas within the burn scar as the higher surface deformation within the scar could lead to biases in the orbit correction.

As InSAR is a double-differencing method, measuring the temporal and spatial differences in interferometric phase, all InSAR measurements have a datum defect and require the identification of a reference point to convert relative deformation into absolute measurements. As reported in several studies, the Anaktuvuk river plain mainly consists of coarse rock and contains

very little ice crystal, except for large scale tectonic motion. Hence it can be considered a stable surface and can be regarded as a good source of reference for this area of interest (Liu et al., 2010). We therefore use the same river bank published in (Liu et al., 2014) as a reference site.

4.4 Study Area and Data Information

In this study, we took the 2007 Anaktuvuk tundra fire as an example for evaluating the necessity and performance of ionospheric correction. Figure 4.2 (a) shows a Google Earth screenshot of the area of interest, a black box shows the outline of the Landsat-5 TM image in Figure 4.2 (b); a Landsat-5 TM image (20080614) in Figure 4.2 (b) indicates the location and extent of the burn scar and shows the damage to vegetation associated with the event. The blue box in Figure 4.2 (b) shows the coverage of the SAR data we used in this study. The Anaktuvuk tundra fire, which was the largest and longest recorded tundra fire in Alaska, started on July 16, 2007 and last until early October of the same year. The resulting burn scar spans an area of more than 100,000 hectares (1,000 km^2) with a north-south extent of more than 40 km. The fire consumed the vegetation and insulating organic layer at the top of the surface, altering the surface energy exchange and leading to an increased in local active layer thickness, the maximum thaw depth of the soil during the summer season. This increase in active layer thickness resulted in a significant increase in the maximal seasonal surface deformation as well as the surface deformation rate (quantified by the seasonal deformation coefficient E) in the fire region (Iwahana et al., 2016; Jones et al., 2015; Liu et al., 2014).

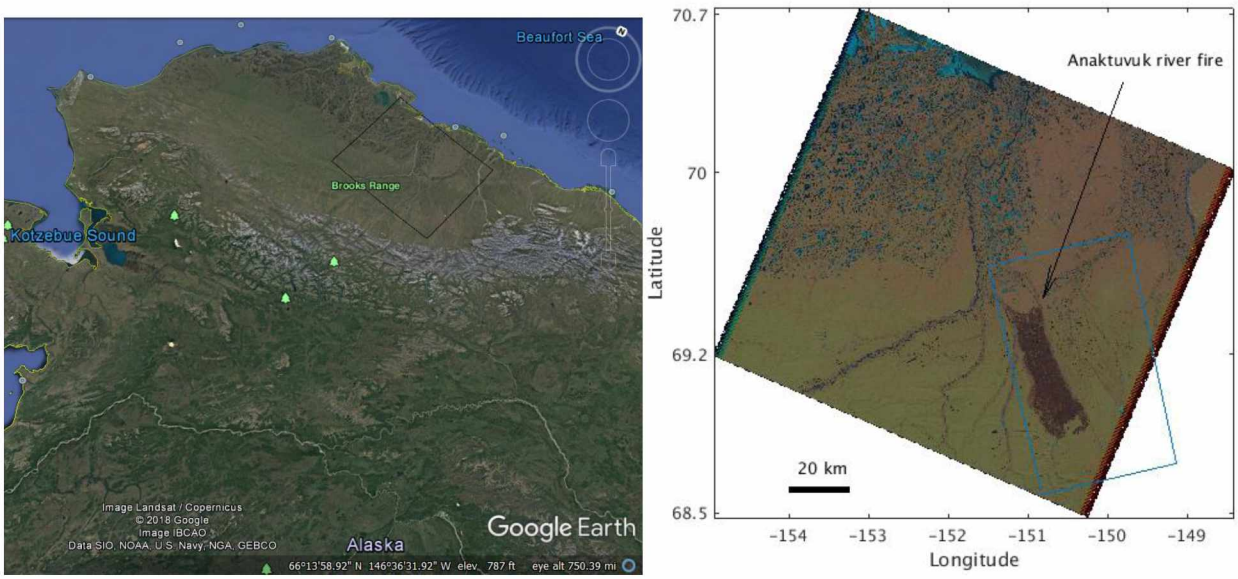

Figure 4.2 Anaktuvuk tundra fire and SAR data coverage.

(a): The black box overlaid on the background google earth imagery shows the outline of Landsat-5 TM image in subplot (b). (b): the blue rectangular area in subplot (b) shows the coverage of the SAR data used in this study, and the background image is a Landsat-5 TM image (20080614). The fire scar at the lower right of the image clearly stands out from its background.

A total of 15 ALOS PALSAR images were acquired for the summer period (May to October) throughout the duration of this mission from late 2006 to early 2011. As the burning area is large, two adjacent scenes are concatenated for each acquisition time to form a larger frame that fully covers the fire perimeter (Frame 1380 and Frame 1390). The data include both fine beam singular polarization (FBS) mode and fine beam dual polarization (FBD) mode acquisitions, characterized by different range resolutions of the image data. All data were acquired in ascending mode at an acquisition time around the local midnight. Detailed information of the ALOS PALSAR data used in this study can be found in Table 4.1.

Previous studies found that some of the acquired L-band images are subject to significant ionospheric contamination, resulting in distortions of azimuth geometry and interferometric phase. These studies either removed severely contaminated data before further processing (Liu et al., 2014) or attempted a mitigation of observed ionospheric effect by fitting a polynomial to the measured interferometric data (Iwahana et al., 2016; Liu et al., 2014). The removal of data points reduced the ability to resolve short-term variations of permafrost deformation. The reduction of redundancy also diminished the accuracy with which deformation coefficients E can be derived.

Additionally, smaller ionospheric distortions in the remaining data sets will further reduce this accuracy and may additionally introduce bias. Polynomial-based correction methods are limited in their performance and may inadvertently remove true deformation signals from the data.

Table 4.1 SAR data information.

SLCs ID	Acquisition date	Beam mode	Bandwidth (MHz)
ALPSRP019001380, ALPSRP019001390	2006-06-03	FBS	28
ALPSRP039131380, ALPSRP039131390	2006-10-19	FBS	28
ALPSRP079391380, ALPSRP079391390	2007-07-22	FBS	28
ALPSRP086101380, ALPSRP086101390	2007-09-06	FBD	14
ALPSRP092811380, ALPSRP092811390	2007-10-22	FBD	14
ALPSRP126361380, ALPSRP126361390	2008-06-08	FBS	28
ALPSRP133071380, ALPSRP133071390	2008-07-24	FBS	28
ALPSRP139781380, ALPSRP139781390	2008-09-08	FBD	14
ALPSRP146491380, ALPSRP146491390	2008-10-24	FBD	14
ALPSRP186751380, ALPSRP186751390	2009-07-27	FBS	28
ALPSRP193461380, ALPSRP193461390	2009-09-11	FBD	14
ALPSRP200171380, ALPSRP200171390	2009-10-27	FBD	14
ALPSRP233721380, ALPSRP233721390	2010-06-14	FBS	28
ALPSRP240431380, ALPSRP240431390	2010-07-30	FBS	28
ALPSRP247141380, ALPSRP247141390	2010-09-14	FBD	14

4.5 Implementation of Ionospheric Correction Techniques over Permafrost Regions

From the 15 SLC images, we formed 105 interferograms using a systematically combination. Due to the fire disturbance, the scattering characteristic of the fire scar area experienced dramatic change. Therefore, a lot of data, especially interferograms formed with data from before and after the burn are almost completely decorrelated. For data with extremely low coherence, the InSAR measurement as well as the ionospheric phase estimate decreases in accuracy or becomes unreliable. Discarding the data with extremely low coherence, we were able to select 39 usable interferograms out of the 105 interferograms with good coherence as well as good ionospheric estimates. These 39 interferograms include data acquired before the fire (pre-fire), data after the fire (post-fire) and data spanned across the fire. Detailed information on the 39 interferograms can be found in Table 4.2.

Table 4.2 Selected 39 Interferograms Data Information

InSAR data pair (master, slave)				
20060603,20061019	20061019,20080724	20070906,20081024	20080908,20090727	20090911,20091027
20060603,20070906	20061019,20081024	20071022,20080608	20080908,20090911	20090911,20100614
20060603,20080608	20070722,20070906	20080608,20080724	20081024,20090727	20090911,20100730
20060603,20080724	20070722,20080724	20080608,20100614	20090727,20090911	20090911,20100914
20060603,20080908	20070722,20080608	20080724,20080908	20090727,20091027	20100614,20100730
20061019,20070722	20070906,20071022	20080724,20090727	20090727,20100614	20100614,20100914
20061019,20070906	20070906,20080608	20080724,20100614	20090727,20100730	20100730,20100914
20061019,20080608	20070906,20080724	20080908,20081024	20090727,20100914	

We implemented the ionospheric estimate for the 39 interferograms following the approach described in section 4.3.3. A thorough examination of the 39 extracted ionospheric phase screens showed that all (100%) data experience different magnitudes of ionospheric distortions. Three examples, including cases experiencing severe, medium and light ionospheric contamination are showcased in Figure 4.3 -- Figure 4.5. For each case, we show the original interferogram, its corresponding ionospheric phase screen estimate and the ionospheric corrected interferogram. For dataset 20100614-20100914 in Figure 4.3, we can see the ionospheric estimate contains about 10 fringes, and the small signal corresponding to surface subsidence of the fire scar area is buried. For dataset 20080724-20090727 presented in Figure 4.4, we can see an intermediate ionospheric contamination with an irregular pattern. For dataset 20090727-20090911 shown in Figure 4.5, ionospheric distortions are small but still measurable using our algorithm.

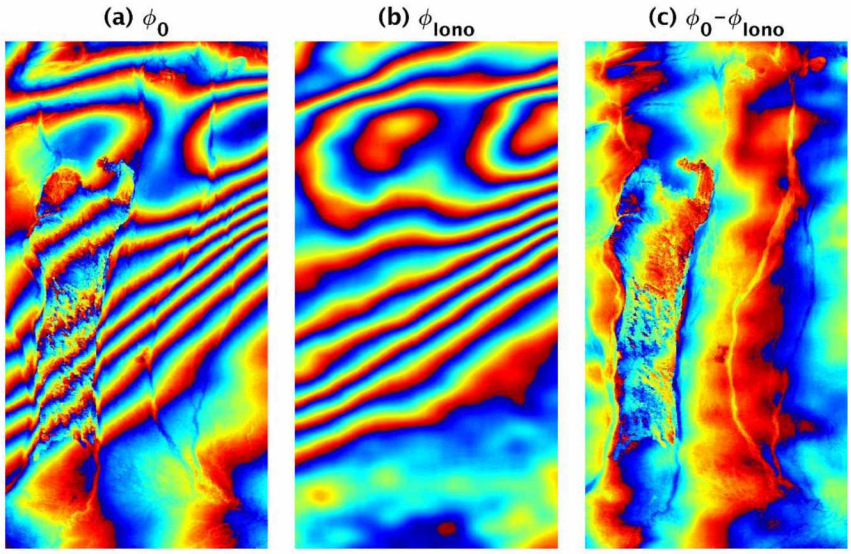

Figure 4.3 Ionospheric contamination, example 1: 20100614-20100914.
(1) Topographic corrected interferogram. (b) Estimated wrapped ionosphere phase screen. (c) Ionosphere corrected interferogram (a-b), residue orbit still exists.

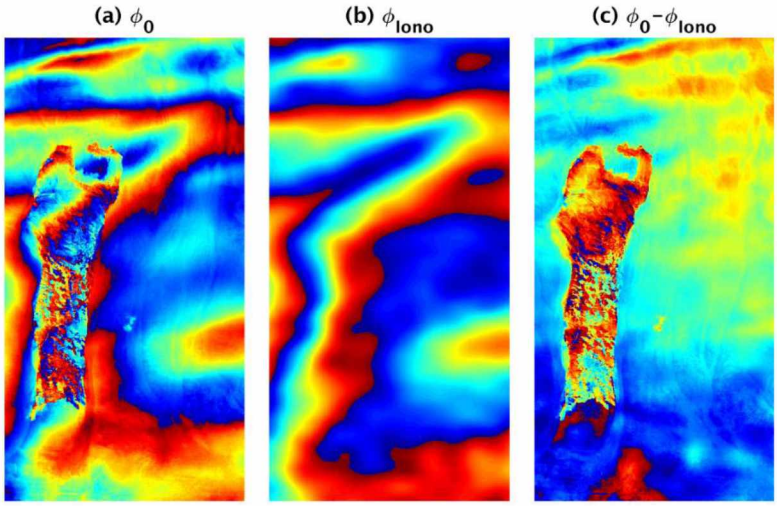

Figure 4.4 Ionospheric contamination, example 2: 20080724-20090727.
(a) Topographic corrected interferogram. (b) Estimated wrapped ionosphere phase screen. (c) Ionosphere corrected interferogram (a-b), residue orbit still exists.

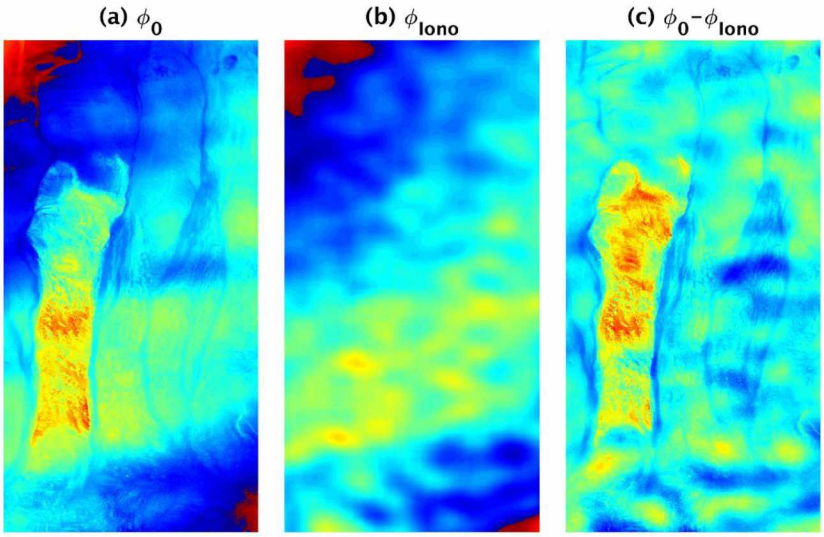

Figure 4.5 Ionospheric contamination, example 3: 20090727-20090911.
(a) Topographic corrected interferogram. (b) Estimated wrapped ionosphere phase screen. (c) Ionosphere corrected interferogram (a-b).

After ionospheric correction, we have 39 corrected interferograms that can be used for the estimation of permafrost deformation parameters. 39 interferograms is about 15% more data compared to a previous study (Liu et al., 2014), in which the same 15 SLCs were used but only 34 interferogram interferograms were usable without ionospheric correction. We will show how the increased number of InSAR estimates and ionospheric correction of these interferograms will improve the permafrost parameter estimate.

4.6 Ionospheric Correction Performance for Permafrost Deformation Monitoring

In this section, we will show how ionospheric correction improves permafrost deformation monitoring. As previously mentioned, there are two general approaches that are typically used for monitoring permafrost deformation: (1) A single interferogram approach that measures the average permafrost-related deformation during the period covered by a single interferogram; and (2) a time series approach that is estimating parameters of a deformation model from an over-determined set of multi-temporal interferograms. We will evaluate the effect of ionospheric correction on both of these approaches.

4.6.1 Single Interferogram-based Permafrost Deformation Estimate

Over natural environments such as permafrost regions, InSAR data usually maintains coherence only over limited time periods. Hence, short time interferograms are often preferred for permafrost monitoring and seasonal deformation estimates are derived by scaling short term

measurements to the duration of a thaw season. While being a frequently used approach, the presence of ionospheric phase distortions combined with the need for large scaling factors often leads to large errors in permafrost deformation measurements derived in this manner (Iwahana et al., 2016). We will show that ionospheric correction enables us to derive seasonal deformation estimates from short time interferograms with reasonable error bars.

4.6.1.1 Short Interval Permafrost Deformation

We took the 2008 year's dataset as an example to showcase that ionospheric correction enables accurate short interval permafrost deformation detection. There are 4 thaw season ALOS PALSAR SAR acquisitions in 2008, the most thaw season acquisitions in one year in the duration of the mission from 2006 to 2011. We formed three interferograms with the shortest possible time separation using the four acquisitions. Detailed information on the three interferograms is provided in Table 4.3.

Table 4.3 Data information of the 2008 short time interval InSAR estimates.

Master	Slave	Temporal baseline (days)	Perpendicular baseline (m)
20080608	20080724	46	4614
20080724	20080908	46	3440
20080908	20081024	46	518

We build two processing flows to process the data both with and without ionospheric correction. In a reference run (the run without ionospheric correction, we named this conventional process), we first use a 1/3 Arc DEM from the National Elevation Database (NED) to correct topographic phase contributions and unwrap the topography-corrected interferometric phase. Subsequently, we fit a 6th order polynomial to the topography-corrected data to account for orbit residue and scale the residual phase to arrive at an estimate for the line-of-sight deformation. In a modified run, we add a split spectrum ionospheric correction step after phase unwrapping and before fitting and subtracting a polynomial. We compare the results from the two methods to assess the impact of ionospheric correction on permafrost deformation estimates.

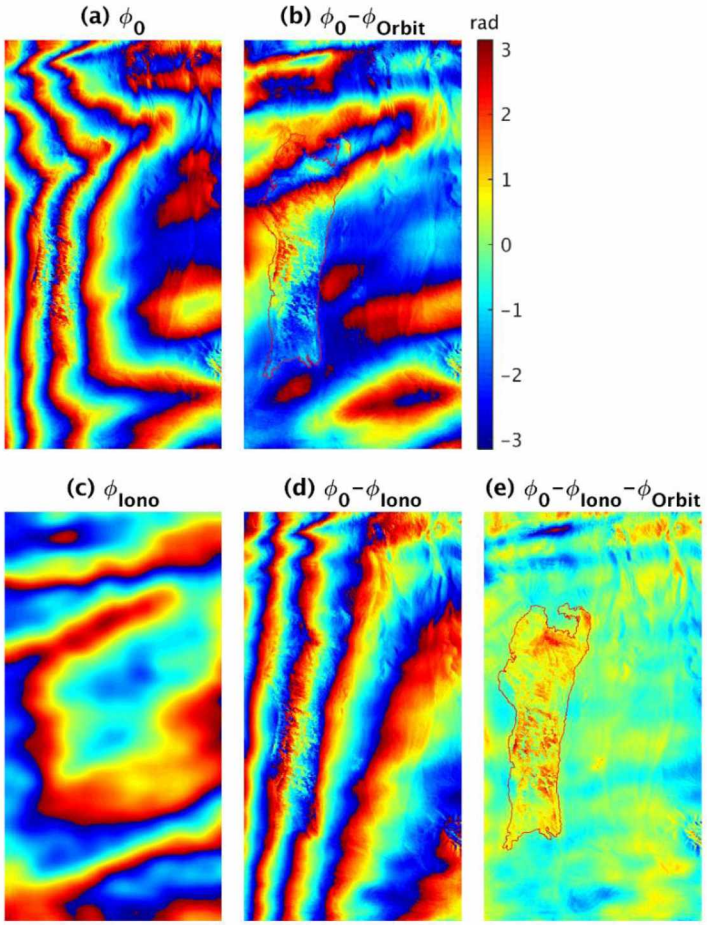

Figure 4.6 Short-interval (20080608-20080724) deformation estimate with and without ionosphere correction. (a) Topographic phase removed interferogram $\emptyset_0$. (b) Interferograms with orbit correction $\emptyset_0 - \emptyset_{\text{orbit}}$. (c) Wrapped Ionospheric phase screen estimate $\emptyset_{\text{Iono}}$. (d) Interferograms with orbit correction $\emptyset_0 - \emptyset_{\text{iono}}$. (e) Interferograms with ionosphere plus orbit correction $\emptyset_0 - \emptyset_{\text{Iono}} - \emptyset_{\text{orbit}}$. All figures share the same colorbar. The fire perimeter is delineated by a red line and plotted in Figure 4.6 (b) and Figure 4.6 (e).

For dataset 20080608-20080724 with 46 days temporal baseline, the results of the two processing flows are shown in Figure 4.6. For the reference run without ionosphere correction, the InSAR estimate in Figure 4.6 (b) is obviously biased. The real signal for the fire scar area is buried in residual ionospheric phase patterns that extend throughout the full extent of the data set. With the ionosphere correction applied (Figure 4.6 (c) – (e)), the extracted deformation signal shows significantly less spatial variation and the deformation patterns within the burn scar become evident (Figure 4.6 (e)). To quantify the improved noise reduction that was achieved via ionospheric correction, we calculate the standard deviation of the deformation estimates outside

of the burn scar for both processing runs. As surface deformation outside of the burn scar is assumed to be small and spatially smooth over the 46 days time span, this area can provide means for an approximate assessment of correction performance. Our analysis shows that ionospheric correction reduces deformation standard deviation from 5.1 cm to 1.4 cm, corresponding to an error reduction by a factor of about 4.

A similar analysis was applied to dataset 20080724-20080908 and the results are shown in Figure 4.7. We see that dense ionosphere-induced fringes were successfully removed and the fire scar deformation stands out after ionosphere correction. We calculate the phase standard deviation outside of the burn scar-affected area to provide a quantitative estimate of correction performance. From this analysis we find the standard deviation of the area outside the fire scar decreases from 4.9 cm to 1.9 cm with ionospheric correction. It should be noted that at the upper left and the lower right corner of the ionosphere-corrected result shows some residual ionospheric error.

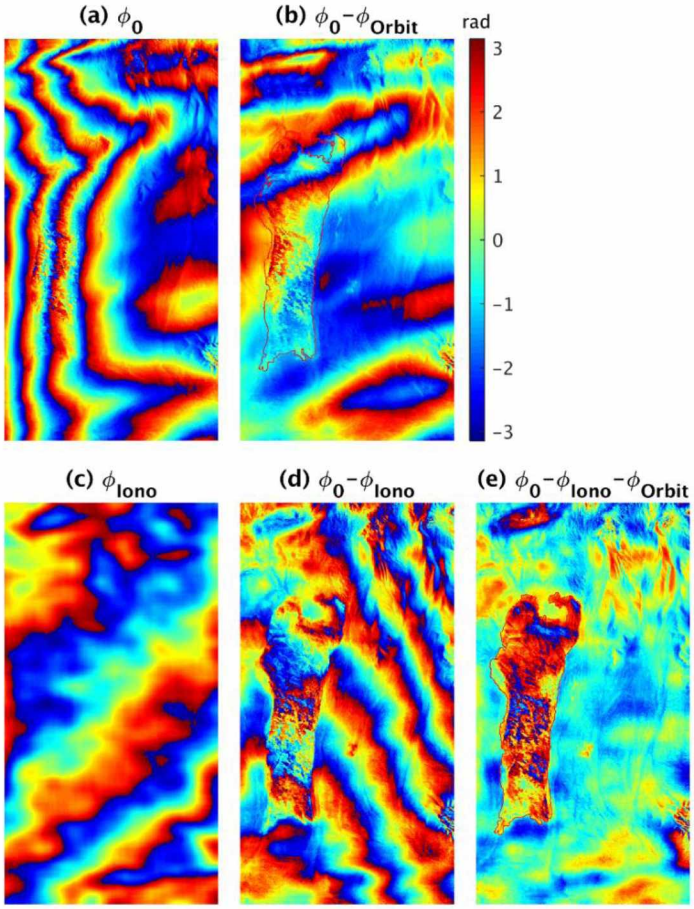

Figure 4.7 Short-interval (20080724-20080908) deformation estimate with and without ionosphere correction. (a) Topographic phase removed interferogram $\emptyset_0$. (b) Interferograms with orbit correction $\emptyset_0 - \emptyset_{\text{orbit}}$. (c) Wrapped Ionospheric phase screen estimate $\emptyset_{\text{Iono}}$. (d) Interferograms with orbit correction $\emptyset_0 - \emptyset_{\text{iono}}$. (e) Interferograms with ionosphere plus orbit correction $\emptyset_0 - \emptyset_{\text{Iono}} - \emptyset_{\text{orbit}}$.

For dataset 20080908-20081024, surface deformation estimates with and without ionospheric correction are shown in Figure 4.8. There it can be seen that ionosphere correction fixes the apparent bias in the conventional estimate where ionosphere correction is not applied. Standard deviation estimates are 1.5 cm and 1.9 cm for the cases with and without ionospheric correction. Though the statistic improvement is not as apparent as in the previous two experiments, we see obvious improvement in a visual analysis (Figure 4.8 (b) vs Figure 4.8 (e)).

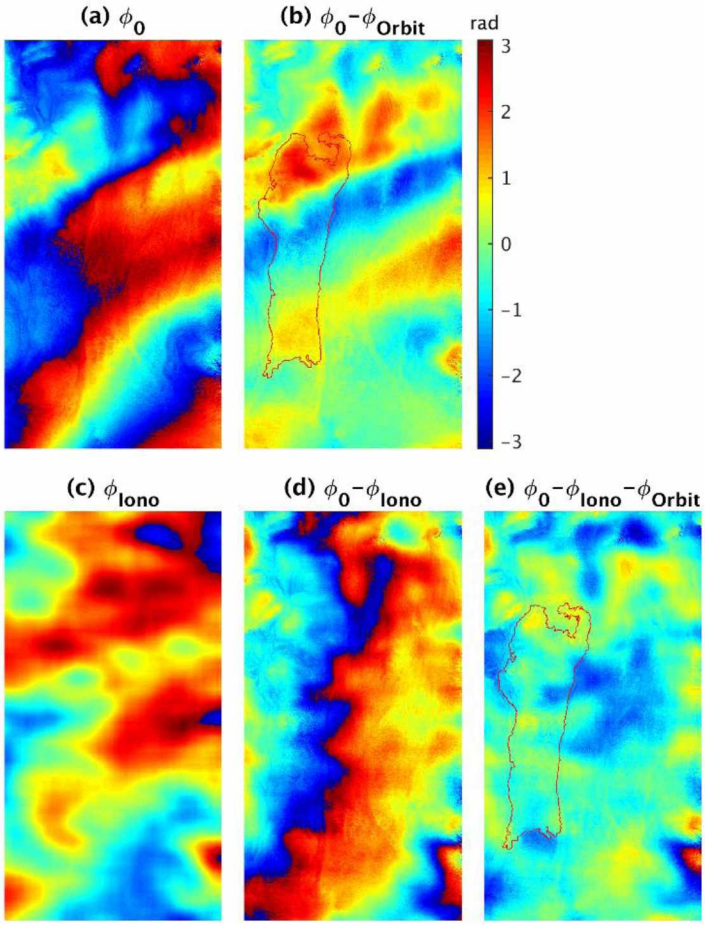

Figure 4.8 Short-interval (20080908-20081024) deformation estimate with and without ionosphere correction. (a) topographic phase removed interferogram $\emptyset_0$. (b) Interferograms with orbit correction $\emptyset_0 - \emptyset_{\text{orbit}}$. (c) wrapped Ionospheric phase screen estimate $\emptyset_{\text{Iono}}$. (d) Interferograms with orbit correction $\emptyset_0 - \emptyset_{\text{iono}}$. (e) Interferograms with ionosphere plus orbit correction $\emptyset_0 - \emptyset_{\text{Iono}} - \emptyset_{\text{orbit}}$.

To further evaluate our ionosphere correction performance, we performed an additional quantitative analysis. We calculate the average deformation rate within the fire scar area and the area outside the fire scar and compare these values for the two processing approaches. The result of this comparison is shown in Table 4.4. For data 20080608-20080724, without ionospheric correction the estimated average deformation within the fire scar and outside the fire scar is -1.9±5.1 cm and -1.6±5.3 cm. For the ionosphere corrected result, the average deformation within the fire scar estimate is 0.0±1.6 cm and outside fire scar is -0.2±1.4 cm. The deformation for the fire scar compared to the outside area are 0.3±7.4 and 0.2±2.1 over a time of 46 days for data

without and with ionospheric correction. We can see the large decrease in the standard deviation of the relative fire-scar area deformation estimate. Similar trends also show for data 20080724-20080908 and 20080908-20081024. These are all indicators for the correctness of the ionospheric correction. It's difficult to fully validate these measurements as there are no such dense estimates from external measurements, but the overlay of the location of the deformation map and the fire perimeter cannot be a coincidence, which means the success of our ionospheric correction.

Table 4.4 InSAR estimate of deformation over fire scar area (unit: cm).

Data	Without ionosphere correction			With ionosphere correction		
	Fire scar	Outside fire scar	difference	Fire scar	Outside fire scar	difference
20080608-20080724	-1.6±5.3	-1.9±5.1	**0.3**±7.4	0.0±1.6	-0.2±1.4	**0.2**±2.1
20080724-20080908	3.2±4.8	2.5±4.9	**0.7**±6.9	1.8±2.7	1.2±1.9	**0.7**±3.3
20080908-20081024	0.8±1.9	0.6±1.9	**0.2**±2.7	0.3±1.3	0.2±1.5	**0.1**±2

4.6.1.2 Seasonal Permafrost Deformation

If sufficient coherence is warranted, seasonal deformation estimates can also be derived by combining the earliest and latest acquisitions available for a thaw season. While this approach has to cope with reduced coherence, it reduces the necessity for applying large scaling factors to convert short term measurements to seasonal deformation estimates. In this part, we quantify the impact of ionospheric correction on this estimation approach. The datasets we used are shown in Table 4.5.

Table 4.5 Data information of the InSAR seasonal deformation estimates.

Yeas	Master	Slave	Temporal baseline (days)	Perpendicular baseline (m)
2006	20060603	20061019	138	973
2007	20070722	20071022	92	780
2008	20080608	20080724	138	4614
	20080724	20080908		3440
	20080908	20081024		518
2009	20090727	20091027	92	1003
2010	20100614	20100914	92	713

We apply the same processing flows as in the previous section to all the datasets in Table 4.5, resulting in thaw season deformation estimates for the years 2006, 2007, 2008, 2009 and 2010.

The results for each year are presented in Figure 4.9, Figure 4.10, Figure 4.11, Figure 4.12 and Figure 4.13 respectively corresponding to years from 2006 to 2010.

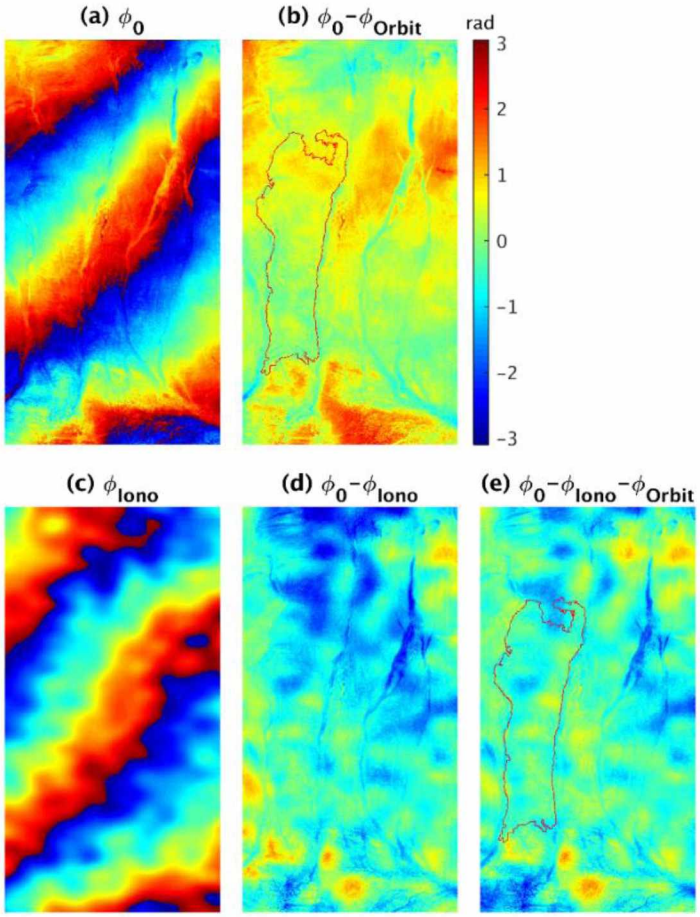

Figure 4.9 2006 seasonal deformation estimate with and without ionosphere correction.
(a) topographic phase removed interferogram $\emptyset_0$. (b) Interferograms with orbit correction $\emptyset_0 - \emptyset_{\text{orbit}}$. (c) wrapped Ionospheric phase screen estimate $\emptyset_{\text{Iono}}$. (d) Interferograms with orbit correction $\emptyset_0 - \emptyset_{\text{iono}}$. (e) Interferograms with ionosphere plus orbit correction $\emptyset_0 - \emptyset_{\text{Iono}} - \emptyset_{\text{orbit}}$.

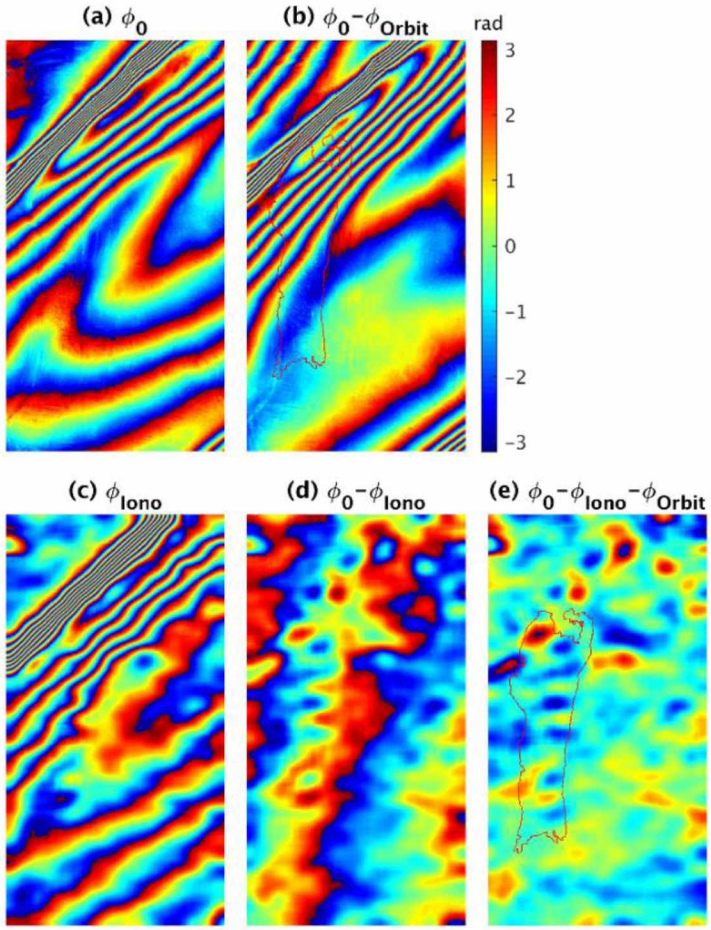

Figure 4.10 2007 seasonal deformation estimate with and without ionosphere correction.
(a) topographic phase removed interferogram $\emptyset_0$. (b) Interferograms with orbit correction $\emptyset_0 - \emptyset_{\text{orbit}}$. (c) wrapped Ionospheric phase screen estimate $\emptyset_{\text{Iono}}$. (d) Interferograms with orbit correction $\emptyset_0 - \emptyset_{\text{iono}}$. (e) Interferograms with ionosphere plus orbit correction $\emptyset_0 - \emptyset_{\text{Iono}} - \emptyset_{\text{orbit}}$. Discrete local bias still exists and shows up in the residue map.

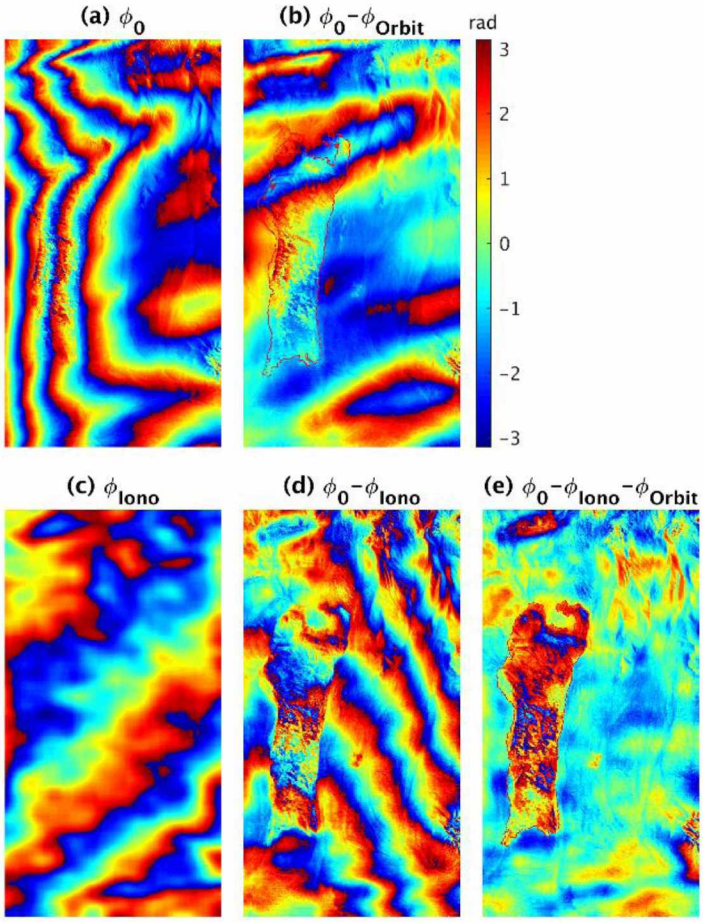

Figure 4.11 2008 seasonal deformation estimate with and without ionosphere correction.
(a) topographic phase removed interferogram $\emptyset_0$. (b) Interferograms with orbit correction $\emptyset_0 - \emptyset_{\text{orbit}}$. (c) wrapped Ionospheric phase screen estimate $\emptyset_{\text{Iono}}$. (d) Interferograms with orbit correction $\emptyset_0 - \emptyset_{\text{iono}}$. (e) Interferograms with ionosphere plus orbit correction $\emptyset_0 - \emptyset_{\text{Iono}} - \emptyset_{\text{orbit}}$.

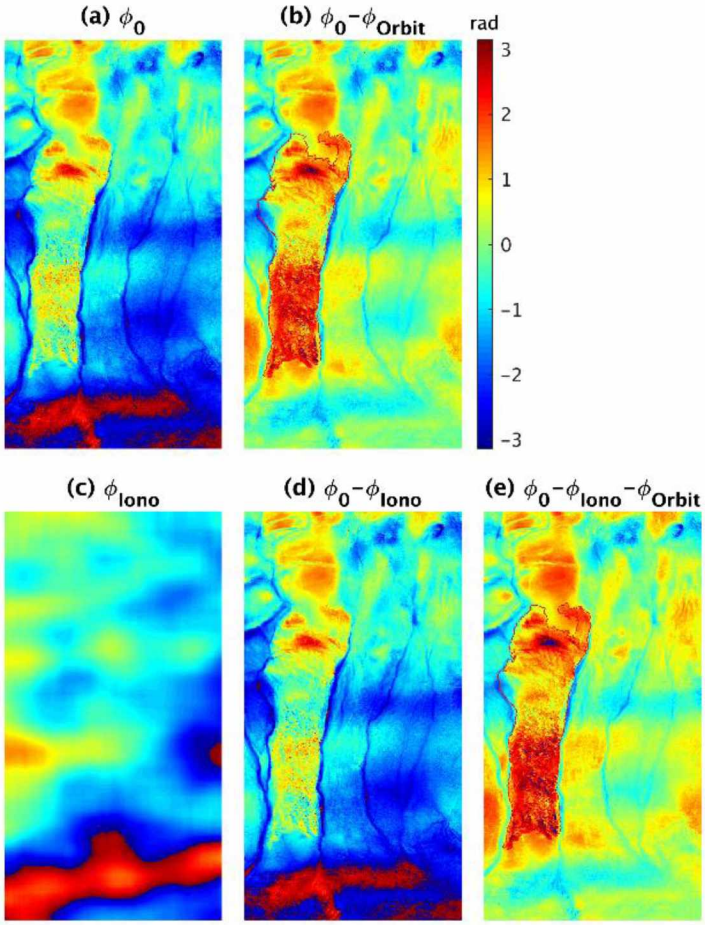

Figure 4.12 2009 seasonal deformation estimate with and without ionosphere correction.
(a) topographic phase removed interferogram $\emptyset_0$. (b) Interferograms with orbit correction $\emptyset_0 - \emptyset_{\text{orbit}}$. (c) wrapped Ionospheric phase screen estimate $\emptyset_{\text{Iono}}$. (d) Interferograms with orbit correction $\emptyset_0 - \emptyset_{\text{iono}}$. (e) Interferograms with ionosphere plus orbit correction $\emptyset_0 - \emptyset_{\text{Iono}} - \emptyset_{\text{orbit}}$.

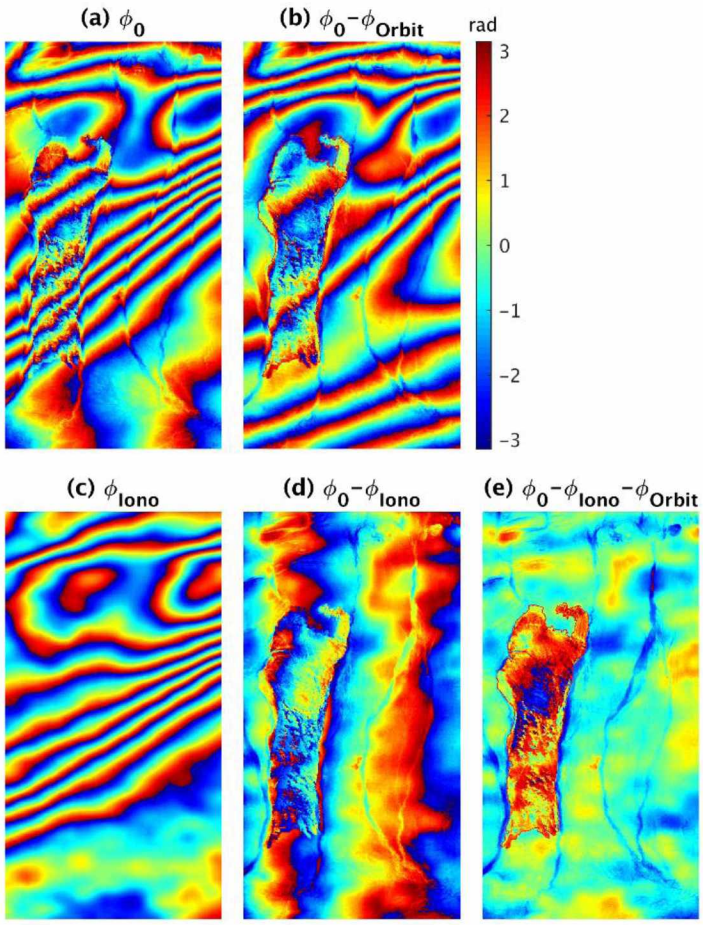

Figure 4.13 2010 seasonal deformation estimate with and without ionosphere correction.
(a) topographic phase removed interferogram $\emptyset_0$. (b) Interferograms with orbit correction $\emptyset_0 - \emptyset_{\text{orbit}}$. (c) wrapped Ionospheric phase screen estimate $\emptyset_{\text{Iono}}$. (d) Interferograms with orbit correction $\emptyset_0 - \emptyset_{\text{iono}}$. (e) Interferograms with ionosphere plus orbit correction $\emptyset_0 - \emptyset_{\text{Iono}} - \emptyset_{\text{orbit}}$.

For each of the five seasonal deformation estimates, we quantify improvements in estimation accuracy by calculating the deformation standard deviation for areas outside of the burn scar for both the workflow with and without ionospheric correction. The variance estimates are presented in Table 4.6 and show significant improvements for 2007, 2008, 2010 data. For 2006, the ionospheric signature shows a ramp-like pattern and the result without formal ionospheric correction shows equivalent standard deviation for the area outside the fire scar is because the orbit fitting processing can correct the ramp-like ionospheric signal well. For 2009 data, the ionospheric distortion is very small, so the outside fire area standard deviation for the ionospheric corrected result is close to the result without ionospheric correction. These experiments demonstrate the

benefit of ionospheric correction. Similar to the previous section, we also estimate the average deformation rates within and outside of the fire scar area for each year and for both processing flows. The result is shown in Table 4.6.

The deformation of the fire scar area compared to outside fire scar area, before ionosphere correction, from 2006 to 2010 are: -0.2±1.4 cm, -1.4±37.3 cm, 3.6±7.4 cm, 0.6±3.2, 0.4±21.3. After the ionosphere correction, the deformation increases from 2006 to 2010 are: -0.1±1.7 cm, -0.3±3.0 cm, 1.0±4.9 cm, 0.6±3.4 cm, 1.1±4.2 cm. Among these estimates, the 2006, 2007 are the pre-fire estimates, while the last three years (2008, 2009,2010) are the post-fire estimates. Our ionosphere correction results and the spatial pattern matches well with the fire perimeter, which is a strong indicator of the success of our ionosphere correction performance. This however does not happen for the estimate without ionosphere correction. Secondly, our ionosphere corrected results show a deformation increase after the fire, which aligns well with previous findings (Iwahana et al., 2016; Jones et al., 2015; Liu et al., 2014). Based on these estimates, we derived the seasonal deformation coefficients for each year. We calculate the average deformation coefficients difference of the fire-scar area and area outside fire scar and then scale them to the seasonal deformation, the results are displayed in columns 'Model Estimate' in Table 4.6. For the model estimate without ionospheric correction, we get a quite large uplift of ~13 cm for year 2007 and a nearly zero for year 2008. With ionospheric correction, the relative deformation seems more reasonable now. We can see a deformation increase for post-fire estimates comparing to pre-fire estimates (shaded in Table 4.6), this is consistent with previous publications (Iwahana et al., 2016; Jones et al., 2015; Liu et al., 2014). We noticed that the 2007 fire scar area shows an uplift of 2.4 cm, this is probably biased as there is still obvious ionospheric residue shown in Figure 4.10. Our estimates for year 2006, 2008, 2009 and 2010 are consistent with publication (Liu et al., 2014) which shows a deformation increase within the fire area of 2~8 cm/season.

Table 4.6 InSAR derived seasonal deformation (unit: cm)

Data	Without ionosphere correction				With ionosphere correction			
	Fire scar	Outside fire scar	Difference	Model Estimate Difference	Fire scar	Outside fire scar	Difference	Model Estimate Difference
20060603-20061019	0.9±0.9	1.0±1.1	**-0.2**±1.4	-0.45±1.9	0.3±1.2	0.4±1.2	**-0.1**±1.7	**-0.5**±2.3
20070722-20071022	-10.5±27.8	-9.0±24.8	**-1.4**±37.3	-12.45±133.5	0.4±2.1	0.7±2.2	**-0.3**±3.0	**-2.4**±10.7
20080608-20081024	3.1±5.4	-0.5±5.1	**3.6**±7.4	-0.01±10.28	2.2±4.0	1.2±2.9	**1.0**±4.9	**3.2**±6.8
20090727-20091027	3.0±2.6	2.3±1.9	**0.6**±3.2	6.4±13.7	4.1±2.6	3.4±2.2	**0.7**±3.4	**7.3±14.6**
20100614-20100914	9.1±14.8	8.7±15.3	**0.4**±21.3	1.5±36.8	4.5±3.4	3.4±2.4	**1.1**±4.2	**4.7**±7.3

4.6.2 Time Series InSAR-based Permafrost Deformation Estimate

We also implemented the InSAR time series solution (see Section 4.3.1), which uses a redundant set of interferograms combined with a geophysical model to arrive at deformation coefficients that describe the deformation behavior across a thaw season. As the time series approach is based on a redundant set of data, it allows for the calculation of covariance information for the derived deformation coefficients, which can be compared to evaluate performance improvement gained by including ionospheric correction into the processing flow.

Using the interferograms with and without ionospheric correction, we derived the pre-fire and post-fire seasonal deformation coefficients following the time series approach in Section 4.3.2. We calculate the maximum ADDTs of each year from 2006 to 2010 using all the 15 SLC data, and its mean maximum ADDTs. With these coefficients and the ADDT, we derived the seasonal deformation for data with and without ionospheric correction. The uncertainty of the deformation estimate is calculated based on Eqs (4.12) - (4.15). The results are shown in Figure 4.14 and Figure 4.15.

We can see a very distinct difference of the model result whether we correct the ionosphere or not. For the result without ionospheric correction, both pre- and post-fire deformation estimates show distinct stripes, which are caused by the ionosphere. Ionosphere-induced distortions of the surface deformation estimates reach up to 2.5 cm in this case. The ionosphere-corrected result

shows a pattern which is consistent with the fire perimeter, and also consistent with results from previous studies (Jones et al., 2015; Liu et al., 2014). A close inspection of the deformation map created from ionosphere-corrected data reveals interesting new details such as a small number of small fire scars near the main Anaktuvuk fire area, which were difficult to see in the uncorrected result.

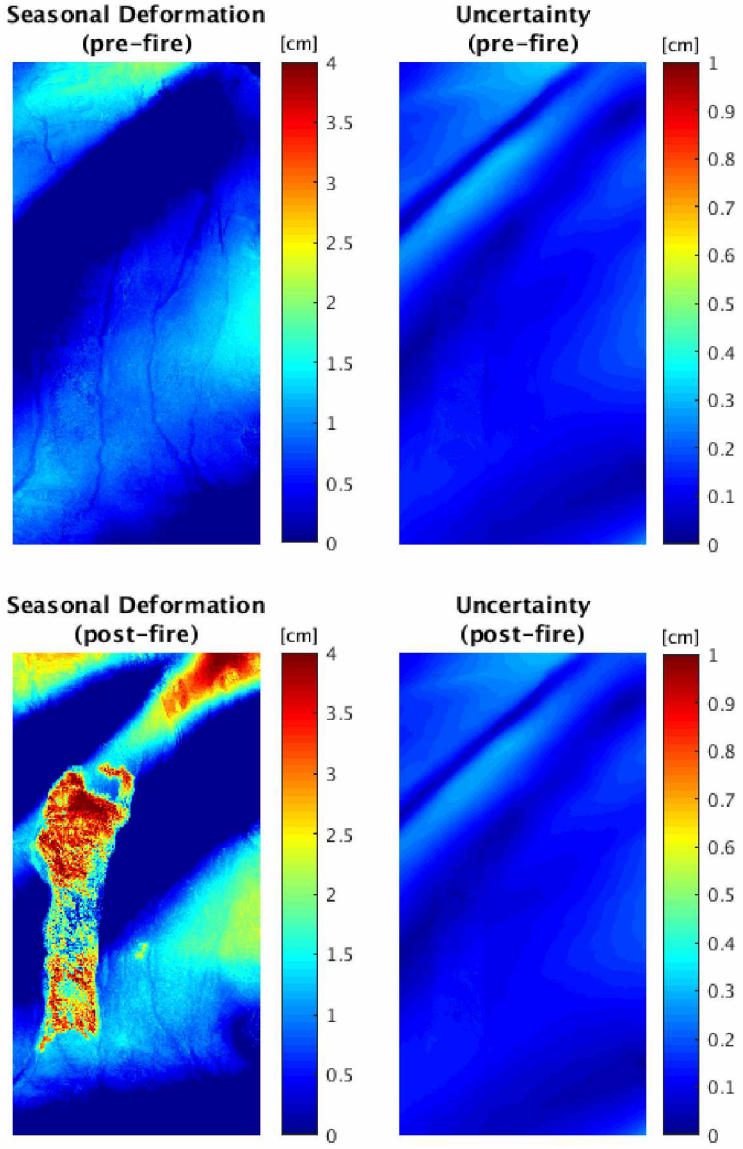

Figure 4.14 Time series derived seasonal deformation (without ionosphere correction).
UL: Seasonal deformation rate for pre-fire period. UR: Corresponding pre-fire accuracy. LL: Seasonal deformation rate for Post-fire period. LR: Corresponding post-fire accuracy.

For a quantitative analysis, we calculate the average deformation rate of the fire scar area for pre-fire and post-fire period using the time series approach. The results with ionosphere correction and without ionosphere correction are compared. Results are shown in Table 4.7.

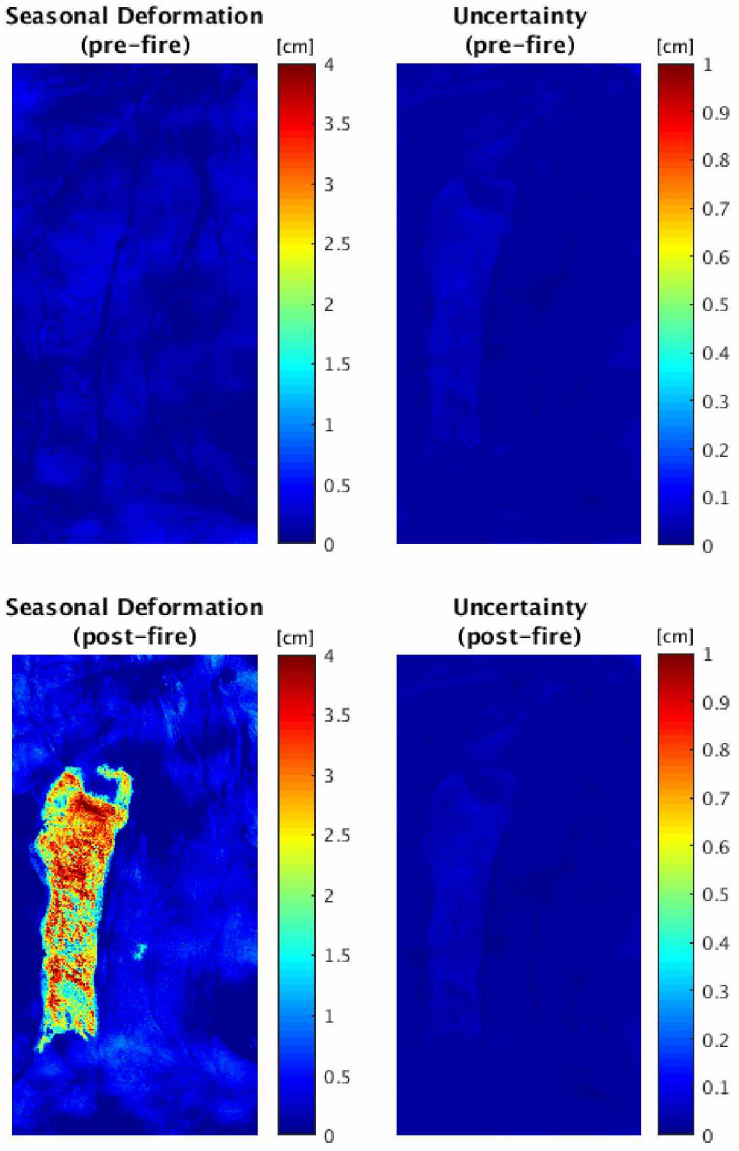

Figure 4.15 Time series derived seasonal deformation (with ionosphere correction). (upper Left). Seasonal deformation rate for pre-fire period. (upper Right) Corresponding accuracy. (lower Left) Seasonal deformation rate for Post-fire period. (lower Right) Corresponding accuracy.

Table 4.7 Time series approach derived fire-scar deformation results (unit: cm/season)

With ionosphere correction		Without ionosphere correction	
Pre-Fire scar	Post-Fire scar	Pre-Fire scar	Post-Fire scar

0.18±0.01	2.46±0.01	-0.02±0.07	2.48±0.06

The average values of the fire scar area and outside area are quite close to each other when corrected and uncorrected data are compared. However, we do see a decrease in standard deviation of the deformation estimates. We plot the histogram of the deformations for the two cases with and without ionosphere correction and the result is shown in Figure 4.16. We can see they have similar mean values, but the distribution shows significant differences. This difference is much more evident in the deformation map in Figure 4.14 and Figure 4.15, especially for the fire-scar area.

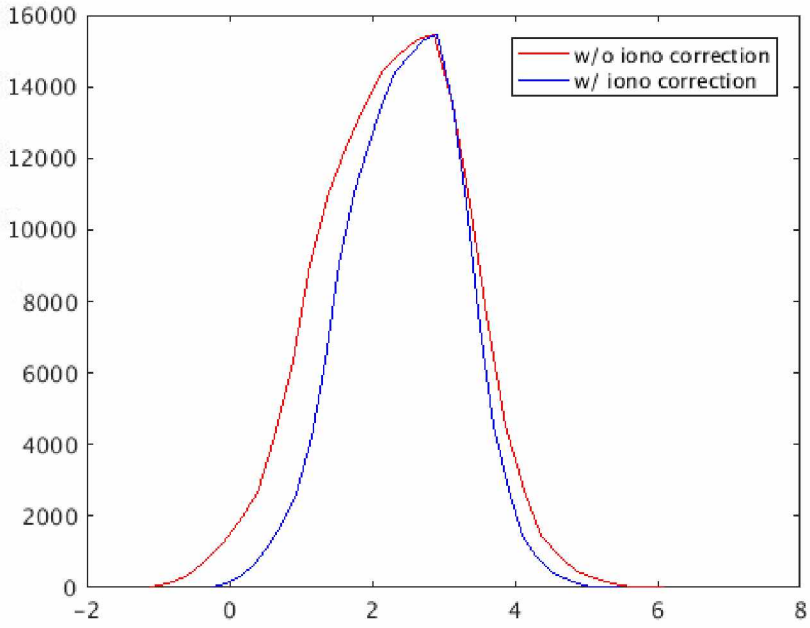

Figure 4.16 Comparison of deformations histograms over fire scar with and without ionosphere correction

4.7 Discussion

We show a large number of examples in this study that the ionosphere correction shows good performance in correcting InSAR data over fire-disturbed permafrost areas. Among the presented examples, a formal split spectrum-based ionospheric correction outperforms typically used orbit fitting approaches. The applied split spectrum approach can increase the temporal sampling that can be achieved with useful InSAR data and can enhance the accuracy of derived surface deformation estimates. This is true especially for cases where the ionospheric signature does not resemble a ramp-like pattern and the InSAR data maintains good coherence. We note that for data with low coherence, our ionosphere estimate can be very noisy. Implementing the correction sometime introduces localized bias, as can be seen in Figure 4.10. Also, we need to be informed

that the orbit fitting approach sometimes works well, e.g. if the ionospheric signal shows ramp-like features. The appropriateness of polynomial fitting also depends on the scale of our study interest. If the area is small and the spatial scale of the ionospheric phase signature is far larger than the area of interest, orbit correction tends to be a suitable approach for mitigating ionospheric distortions.

4.8 Conclusion

We introduced the range sub-band split spectrum InSAR approach for permafrost ionospheric correction. We chose the Anaktuvuk tundra fire as a test site for our study. The tundra fire is known to lead an increase of the permafrost deformation and this increased deformation has a distinct pattern that coincides with the fire-scar footprint. This distinct pattern plays as an ideal criterion for us to validate our ionosphere correction performance. With ionosphere correction, we were able to form 39 useful interferograms from 15 SAR images, which is about 15% more than previous studies achieved of no ionosphere correction was applied. Our ionospheric phase screen estimates show that all data experiences different magnitude of ionosphere contamination. Selected examples with L-band ALOS PLASAR InSAR data are presented in this study. With ionospheric correction, the estimated deformation map shows a distinct pattern that overlaid well with the fire perimeter. This is a strong indicator for the correctness of the ionospheric correction.

We evaluated the performance of ionospheric correction for different InSAR approaches typically used for permafrost analysis. We presented three datasets in 2008 for short-interval single interferogram permafrost deformation analysis. With ionosphere correction, the outside of fire-scar area deformation standard deviation drops, and the decreases were large for some datasets. The decrease of the deformation in the outside fire-scar area proves the permafrost deformation estimate accuracy improvement. For the single interferogram-based long-term deformation estimate, we show that ionospheric correction allows us to form useful interferograms for permafrost deformation estimates with the largest possible temporal separation, this large temporal separation estimate can reduce the scaling factor effect in seasonal deformation analysis. Our model estimates of the relative deformation within the fire scar have good consistency with previous studies, while the ones without ionosphere correction are largely biased.

In the time series approach, we demonstrate incorporating the ionospheric correction can help to improve the accuracy of permafrost deformation measurements. This can be seen from two different aspects: (1) the permafrost estimate with ionosphere correction shows the distinct pattern

of the fire scar; (2) a lower standard deviation of both the fire scar area and outside fire scar area after ionosphere correction was applied. In the discussion, we talk about the strengths and weakness of the proposed ionosphere correction.

4.9 Acknowledgement

The ALOS PALSAR SAR data used in this study were acquired by JAXA and provided to us through the Alaska Satellite Facility (ASF). We thank Scott Arko from ASF for providing us concatelated SLC data used in this study.

4.10 Reference

Brcic, R., Parizzi, A., Eineder, M., Bamler, R., Meyer, F., 2010. Estimation and compensation of ionospheric delay for SAR interferometry, in: Geoscience and Remote Sensing Symposium (IGARSS), 2010 IEEE International. IEEE, pp. 2908–2911.

Environmental Data Center Team. 2018. Meteorological monitoring program at Toolik, Alaska. Toolik Field Station, Institute of Arctic Biology, University of Alaska Fairbanks, Fairbanks, AK 99775. http://toolik.alaska.edu/edc/abiotic_monitoring/data_query.php

Eshqi Molan, Y., Kim, J.-W., Lu, Z., Wylie, B., Zhu, Z., 2018. Modeling Wildfire-Induced Permafrost Deformation in an Alaskan Boreal Forest Using InSAR Observations. Remote Sensing 10, 405. https://doi.org/10.3390/rs10030405

Fejer, B.G., Kelley, M.C., 1980. Ionospheric irregularities. Reviews of Geophysics 18, 401–454.

Feng, G., 2011. Coseismic deformation and ionospheric variation associated with Wenchuan earthquake estimated from InSAR.

Gomba, G., Parizzi, A., De Zan, F., Eineder, M., Bamler, R., 2016. Toward operational compensation of ionospheric effects in SAR interferograms: the split-spectrum method. IEEE Transactions on Geoscience and Remote Sensing 54, 1446–1461.

Gray, A.L., Mattar, K.E., Sofko, G., 2000. Influence of ionospheric electron density fluctuations on satellite radar interferometry. Geophysical Research Letters 27, 1451–1454.

Hooper, A., Bekaert, D., Spaans, K., Arıkan, M., 2012. Recent advances in SAR interferometry time series analysis for measuring crustal deformation. Tectonophysics 514–517, 1–13. https://doi.org/10.1016/j.tecto.2011.10.013

Iwahana, G., Uchida, M., Liu, L., Gong, W., Meyer, F.J., Guritz, R., Yamanokuchi, T., Hinzman, L., 2016. InSAR Detection and Field Evidence for Thermokarst after a Tundra Wildfire, Using ALOS-PALSAR. Remote Sensing 8, 218.

Jones, B.M., Grosse, G., Arp, C.D., Miller, E., Liu, L., Hayes, D.J., Larsen, C.F., 2015. Recent Arctic tundra fire initiates widespread thermokarst development. Scientific Reports 5. https://doi.org/10.1038/srep15865

Li, Z., Zhao, R., Hu, J., Wen, L., Feng, G., Zhang, Z., Wang, Q., 2015. InSAR analysis of surface deformation over permafrost to estimate active layer thickness based on one-dimensional heat transfer model of soils. Scientific reports 5, 15542.

Liao, H., Meyer, F .J., 2018. On the Practical Implementation of Split Spectrum Technique for Interferometric SAR Ionospheric Effect Correction. In preparation.

Liao, H., Meyer, F.J., Liu, L., 2017. Ionospheric Correction in Using ALOS PALSAR InSAR Data for Monitoring Permafrost Subsidence associated with an Arctic Tundra Fire, in: AGU Fall Meeting Abstracts.

Liao, H., Meyer, F.J., Scheuchl, B., Mouginot, J., Joughin, I., Rignot, E., 2018. Ionospheric correction of InSAR data for accurate ice velocity measurement at polar regions. Remote Sensing of Environment 209, 166–180. https://doi.org/10.1016/j.rse.2018.02.048

Liu, L., Jafarov, E.E., Schaefer, K.M., Jones, B.M., Zebker, H.A., Williams, C.A., Rogan, J., Zhang, T., 2014. InSAR detects increase in surface subsidence caused by an Arctic tundra fire. Geophysical Research Letters 41, 3906–3913. https://doi.org/10.1002/2014GL060533

Liu, L., Schaefer, K.M., Chen, A.C., Gusmeroli, A., Zebker, H.A., Zhang, T., 2015. Remote sensing measurements of thermokarst subsidence using InSAR. Journal of Geophysical Research: Earth Surface 120, 1935–1948.

Liu, L., Zhang, T., Wahr, J., 2010. InSAR measurements of surface deformation over permafrost on the North Slope of Alaska. Journal of Geophysical Research 115. https://doi.org/10.1029/2009JF001547

Marshall, S.J., 2011. The cryosphere. Princeton University Press.

Mattar, K.E., Gray, A.L., 2002. Reducing ionospheric electron density errors in satellite radar interferometry applications. Canadian Journal of Remote Sensing 28, 593–600.

Perkins, F.W., 1975. Ionospheric irregularities. Reviews of Geophysics 13, 884–884.

Raucoules, D., de Michele, M., 2010. Assessing Ionospheric Influence on L-Band SAR Data: Implications on Coseismic Displacement Measurements of the 2008 Sichuan Earthquake. IEEE Geoscience and Remote Sensing Letters 7, 286–290. https://doi.org/10.1109/LGRS.2009.2033317

Rykhus, R.P., Lu, Z., 2008. InSAR detects possible thaw settlement in the Alaskan Arctic Coastal Plain. Canadian Journal of Remote Sensing 34, 100–112.

Schaefer, K., Lantuit, H., Romanovsky, V.E., Schuur, E.A.G., Witt, R., 2014. The impact of the permafrost carbon feedback on global climate. Environmental Research Letters 9, 085003. https://doi.org/10.1088/1748-9326/9/8/085003

Short, N., Brisco, B., Couture, N., Pollard, W., Murnaghan, K., Budkewitsch, P., 2011. A comparison of TerraSAR-X, RADARSAT-2 and ALOS-PALSAR interferometry for monitoring permafrost environments, case study from Herschel Island, Canada. Remote Sensing of Environment 115, 3491–3506. https://doi.org/10.1016/j.rse.2011.08.012

Short, N., LeBlanc, A.-M., Sladen, W., Oldenborger, G., Mathon-Dufour, V., Brisco, B., 2014. RADARSAT-2 D-InSAR for ground displacement in permafrost terrain, validation from Iqaluit Airport, Baffin Island, Canada. Remote Sensing of Environment 141, 40–51. https://doi.org/10.1016/j.rse.2013.10.016

Tarnocai, C., Canadell, J.G., Schuur, E.A.G., Kuhry, P., Mazhitova, G., Zimov, S., 2009. Soil organic carbon pools in the northern circumpolar permafrost region. Global biogeochemical cycles 23.

Zhang, T., Barry, R.G., Knowles, K., Heginbottom, J.A., Brown, J., 2008. Statistics and characteristics of permafrost and ground-ice distribution in the Northern Hemisphere. Polar Geography 31, 47–68.

Chapter 5

Conclusion

InSAR has been proven to be an effective tool for monitoring subtle ground deformation over large areas and has been widely used in geophysical studies of earthquakes, volcanos, landslides, glaciers and permafrost. InSAR will play a more important role in geophysical studies in the future as more data with higher quality and lower cost will become available. For InSAR applications, how to separate the noise signal from real geophysical information is an important topic. This thesis addresses the detection and removal of ionospheric signals in InSAR data by developing an advanced ionospheric signal correction technique and evaluating the benefits of incorporating this technique into existing workflows for glacier velocity measurements and permafrost deformation applications.

In Chapter 2, we presented an advanced ionospheric correction approach by incorporating spectral shift effects associated with large baseline data and by introducing a multiple sub-band split spectrum approach that goes beyond the traditional split spectrum concepts. We analyzed the impact of spectral shift effects on the implementation of split spectrum techniques and proposed an effective solution to ensure optimal split spectrum performance even in the presence of long spatial baselines. For data with low coherence, the conventional split spectrum technique is often limited in its performance by the emergence of non-random errors such as phase unwrapping errors. We proposed a multiple sub-band approach to improve the ionospheric estimation performance by increasing achievable accuracy as well as computational robustness. We analyzed optimized sub-band configurations as well as sub-band bandwidths for the multiple sub-band approach. We also presented a case study to demonstrate the performance of the proposed technique relative to conventional implementations. The result validated our algorithm both in visual inspection and quantitative analysis. Our developed technique has been delivered to several research groups and has started to benefit the community.

In Chapter 3, we applied the ionospheric correction concept to glacier velocity measurements over the ice sheets of Greenland and the Antarctic. Three case studies based on ALOS PALSAR data were used to assess the performance of the split spectrum technique for ionospheric correction in these areas. We employed several approaches to evaluate ionospheric correction results, including visual inspection, profile analysis, comparison of experimental and theoretical errors, comparison with reference data from other sources, generation of double

difference interferograms, and analysis of time series of multi-temporal data. Our experiments showed that ionospheric distortions are observed regularly. Quantitative assessments showed that ionospheric noise in our data sets reached 14 m/yr and 10 m/yr equivalent glacier velocity in Greenland and Antarctica, respectively, each exceeding the signal associated with ice motion. Our performance analyses using several different approaches demonstrated that the split spectrum technique provides an effective means for ionospheric correction. The split spectrum technique was found to be superior to currently used approaches such as baseline fitting and multi-temporal averaging. Through split spectrum-based ionospheric correction phase noise levels could be reduced by a factor of 70% in Greenland and 90% in the Antarctic.

In Chapter 4, we evaluated the influence of ionospheric distortions on L-band InSAR-based permafrost deformation measurements. We assessed the benefits of ionospheric correction by analyzing ALOS PALSAR SAR data for the measurement of permafrost deformation associated with the 2007 Anaktuvuk river fire. Our analysis showed that after incorporating ionospheric correction to the InSAR data, a total of 39 interferograms with low phase noise can be generated from an initial set of 15 SLCs, which is about 15% more data than reported in previous studies using the same data for this area. Our ionospheric phase screen estimates of the 39 interferograms revealed that each interferogram experienced ionosphere contamination, with phase distortions ranging from mild to severe. We presented three cases showing the different level of ionospheric phase distortions. We evaluated ionosphere-correction for single interferogram-based and time series-based permafrost deformation estimates. We showed that split spectrum-based techniques improve short time interval permafrost deformation monitoring and leads to more robust and accurate estimates of seasonal deformation rates. We also presented the improvement in permafrost estimates that can be achieved by integrating split spectrum-based ionospheric correction into the framework of a commonly used time series model approach. We quantified the achievable performance improvement through visual inspection and by comparison to standard processing procedures.

In summary, our work has improved the technique for the estimation and correction of ionospheric signals in low-frequency InSAR data. The developed technology has been delivered to several research groups and has already been benefiting the InSAR community. Through the study of glacier velocity and permafrost deformation applications, we have evaluated the performance and robustness of ionospheric correction techniques for geophysical applications that

are most affected by the ionospheric influence. We showed that the inclusion of the developed techniques improves our ability to use InSAR for glacier and permafrost studies. Our study demonstrates that the proposed technique is effective for ionospheric estimation and correction. An assessment of L-band InSAR data over high-latitude areas showed that most low-frequency SAR acquisitions show measurable ionospheric distortions. Hence, ionospheric correction should be a standard component of processing workflows applying L-band InSAR data to study high-latitude environments.

Several directions of future work can be envisioned based on the conducted research:

The interest in developing effective algorithms for SAR/InSAR data ionospheric correction is growing in the community. To develop effective correction algorithms, it would be important to have a thorough understanding of the ionospheric statistical properties including its spatial characteristics in 2D and 3D. One work that can be attempted is to collect large volumes of SAR data, e.g., all polarimetric ALOS PALSAR data in North America, and analyze these data for Faraday rotation to derive corresponding TEC maps. This study will not only benefit the understanding of the statistical properties of the ionosphere but would also help compiling a comprehensive catalogue with different ionospheric distortions. Publication of such a catalogue to the community would support the development of effective algorithms in the long run.

Also, it would be interesting to organize SAR data with simultaneous ionospheric measurements from other instruments, like those provided by GPS, The High-frequency Active Auroral Research Program (HAARP), The Super Dual Auroral Radar Network (SuperDARN) or all-sky cameras to improve our ability to study ionospheric properties (density profiles, ionospheric drift speeds). This can be useful to improve our understanding of ionospheric effects in SAR data across a wider range of ionospheric scenarios.

Based on our work for improved ice velocity measurements, this work can be applied for numerous geophysical applications, such as elastic rebound due to deglacial process, delineation of drainage basins, and the determination of the location of the ice divide on the large ice sheets.